Multilevel model reduction for uncertainty quantification in computational structural dynamics

Olivier ´ Ezvan

UNIVERSITE PARIS-EST

Année 2016

THÈSE

pour obtenir le grade de

DOCTEUR DE L'UNIVERSITÉ PARIS-EST

Discipline: Mécanique

présentée et soutenue publiquement
par

Olivier Ezvan

le 23 septembre 2016

Titre:

Multilevel model reduction for uncertainty quantification in computational structural dynamics

JURY

M. Louis JÉZÉQUEL,	Professeur, ECL,	*président*
M. Geert DEGRANDE,	Professeur, KU Leuven,	*rapporteur*
M. Jean-François DEÜ,	Professeur, CNAM,	*rapporteur*
M. Christian SOIZE,	Professeur, UPEM,	*directeur de thèse*
M. Anas BATOU,	Maître de Conférences, UPEM,	*co-encadrant*
M. Laurent GAGLIARDINI,	Docteur, PSA Peugeot Citroën,	*examinateur*

Acknowledgments

Je remercie les professeurs G. Degrande et J.-F. Deü de m'avoir fait l'honneur de rapporter ma thèse. J'ai été très sensible à leurs rapports de pré-soutenance, riches de conseils et d'enthousiasme. Je remercie le professeur L. Jézéquel d'avoir assuré le rôle de président du jury ainsi que L. Gagliardini d'avoir examiné ma thèse. Pour leur temps à tous, consacré à l'étude de mes travaux, et pour l'ensemble de leurs questions et remarques lors de la soutenance, ayant permis un échange très enrichissant et fructueux, j'en suis à la fois honoré et reconnaissant.

Mes remerciements vont maintenant bien-sûr au professeur C. Soize, mon directeur de thèse, qui m'a offert un cadre de travail idéal à tout point de vue. Je le remercie plus particulièrement pour son investissement des plus généreux pour me guider tout au long de cette thèse. Je remercie également mon co-encadrant de thèse, A. Batou, pour son implication soutenue et son aide très étroite, lesquelles contribuant à mon sentiment d'avoir profité d'un encadrement exceptionnel.

Je me dois également de remercier l'ensemble des membres du laboratoire MSME pour leur gentillesse et sympathie, de leur soutien notamment lors des congrès, ou encore de leurs enseignements dont j'ai pu bénéficier avant et pendant ma thèse. Sans oublier les non-permanents de MSME, pour la plupart doctorants, pour ces bons moments et pour leur soutien.

Il va sans dire que je suis redevable du soutien inconditionnel et atemporel de ma famille, dont la présence nombreuse à ma soutenance m'a touché, merci.

Summary

This work deals with an extension of the classical construction of reduced-order models (ROMs) that are obtained through modal analysis in computational linear structural dynamics. It is based on a multilevel projection strategy and devoted to complex structures with uncertainties. Nowadays, it is well recognized that the predictions in structural dynamics over a broad frequency band by using a finite element model must be improved in taking into account the model uncertainties induced by the modeling errors, for which the role increases with the frequency. In such a framework, the nonparametric probabilistic approach of uncertainties is used, which requires the introduction of a ROM. Consequently, these two aspects, frequency-evolution of the uncertainties and reduced-order modeling, lead us to consider the development of a multilevel ROM in computational structural dynamics, which has the capability to adapt the level of uncertainties to each part of the frequency band. In this thesis, we are interested in the dynamical analysis of complex structures in a broad frequency band. By complex structure is intended a structure with complex geometry, constituted of heterogeneous materials and more specifically, characterized by the presence of several structural levels, for instance, a structure that is made up of a stiff main part embedding various flexible sub-parts. For such structures, it is possible having, in addition to the usual global-displacements elastic modes associated with the stiff skeleton, the apparition of numerous local elastic modes, which correspond to predominant vibrations of the flexible sub-parts. For such complex structures, the modal density may substantially increase as soon as low frequencies, leading to high-dimension ROMs with the modal analysis method (with potentially thousands of elastic modes in low frequencies). In addition, such ROMs may suffer from a lack of robustness with respect to uncertainty, because of the presence of the numerous local displacements, which are known to be very sensitive to uncertainties. It should be noted that in contrast to the usual long-wavelength global displacements of the low-frequency (LF) band, the local displacements associated with the structural sub-levels, which can then also appear in the LF band, are characterized by short wavelengths, similarly to high-frequency (HF) displacements. As a result, for the complex structures considered, there is an overlap of the three vibration regimes, LF, MF, and HF, and numerous local elastic modes are intertwined with the usual global elastic modes. This implies two major difficulties, pertaining to uncertainty quantification and to computational efficiency. The objective of this thesis is thus double. First, to provide a multilevel stochastic ROM that is able to take into account the heterogeneous variability introduced by the overlap of the three vibration regimes. Second, to provide a predictive ROM whose dimension

is decreased with respect to the classical ROM of the modal analysis method. A general method is presented for the construction of a multilevel ROM, based on three orthogonal reduced-order bases (ROBs) whose displacements are either LF-, MF-, or HF-type displacements (associated with the overlapping LF, MF, and HF vibration regimes). The construction of these ROBs relies on a filtering strategy that is based on the introduction of global shape functions for the kinetic energy (in contrast to the local shape functions of the finite elements). Implementing the nonparametric probabilistic approach in the multilevel ROM allows each type of displacements to be affected by a particular level of uncertainties. The method is applied to a car, for which the multilevel stochastic ROM is identified with respect to experiments, solving a statistical inverse problem. The proposed ROM allows for obtaining a decreased dimension as well as an improved prediction with respect to a classical stochastic ROM.

Short summary

For some complex dynamical structures exhibiting several structural scales, numerous local displacements can be intertwined with the usual global displacements, inducing an overlap of the low-, medium-, and high-frequency vibration regimes (LF, MF, HF). Hence the introduction of a multilevel reduced-order model (ROM), based on three reduced-order bases (ROBs) that are constituted of either LF-, MF-, or HF-type displacements. These ROBs are obtained using a filtering method based on global shape functions for the kinetic energy. First, thanks to the filtering of local displacements, the dimension of the multilevel ROM is reduced compared to classical modal analysis. Second, implementing the nonparametric probabilistic approach in the multilevel ROM allows each type of displacements to be affected by a particular level of uncertainties. The method is applied to a car, for which the multilevel stochastic ROM is identified with respect to experiments, solving a statistical inverse problem.

Résumé

Ce travail de recherche présente une extension de la construction classique des modèles réduits (ROMs) obtenus par analyse modale, en dynamique numérique des structures linéaires. Cette extension est basée sur une stratégie de projection multi-niveau, pour l'analyse dynamique des structures complexes en présence d'incertitudes. De nos jours, il est admis qu'en dynamique des structures, la prévision sur une large bande de fréquence obtenue à l'aide d'un modèle éléments finis doit être améliorée en tenant compte des incertitudes de modèle induites par les erreurs de modélisation, dont le rôle croît avec la fréquence. Dans un tel contexte, l'approche probabiliste non-paramétrique des incertitudes est utilisée, laquelle requiert l'introduction d'un ROM. Par conséquent, ces deux aspects, évolution fréquentielle des niveaux d'incertitudes et réduction de modèle, nous conduisent à considérer le développement d'un ROM multi-niveau, pour lequel les niveaux d'incertitudes dans chaque partie de la bande de fréquence peuvent être adaptés. Dans cette thèse, on s'intéresse à l'analyse dynamique de structures complexes caractérisées par la présence de plusieurs niveaux structuraux, par exemple avec un squelette rigide qui supporte diverses sous-parties flexibles. Pour de telles structures, il est possible d'avoir, en plus des modes élastiques habituels dont les déplacements associés au squelette sont globaux, l'apparition de nombreux modes élastiques locaux, qui correspondent à des vibrations prédominantes des sous-parties flexibles. Pour ces structures complexes, la densité modale est susceptible d'augmenter fortement dès les basses fréquences (BF), conduisant, via la méthode d'analyse modale, à des ROMs de grande dimension (avec potentiellement des milliers de modes élastiques en BF). De plus, de tels ROMs peuvent manquer de robustesse vis-à-vis des incertitudes, en raison des nombreux déplacements locaux qui sont très sensibles aux incertitudes. Il convient de noter qu'au contraire des déplacements globaux de grande longueur d'onde caractérisant la bande BF, les déplacements locaux associés aux sous-parties flexibles de la structure, qui peuvent alors apparaître dès la bande BF, sont caractérisés par de courtes longueurs d'onde, similairement au comportement dans la bande hautes fréquences (HF). Par conséquent, pour les structures complexes considérées, les trois régimes vibratoires BF, MF et HF se recouvrent, et de nombreux modes élastiques locaux sont entremêlés avec les modes élastiques globaux habituels. Cela implique deux difficultés majeures, concernant la quantification des incertitudes d'une part et le coût numérique d'autre part. L'objectif de cette thèse est alors double. Premièrement, fournir un ROM stochastique multi-niveau qui est capable de rendre compte de la variabilité hétérogène introduite par le recouvrement des trois régimes vibratoires. Deuxièmement, fournir un ROM prédictif de dimension réduite par rapport à celui

de l'analyse modale. Une méthode générale est présentée pour la construction d'un ROM multi-niveau, basée sur trois bases réduites (ROBs) dont les déplacements correspondent à l'un ou l'autre des régimes vibratoires BF, MF ou HF (associés à des déplacements de type BF, de type MF ou bien de type HF). Ces ROBs sont obtenues via une méthode de filtrage utilisant des fonctions de forme globales pour l'énergie cinétique (par opposition aux fonctions de forme locales des éléments finis). L'implémentation de l'approche probabiliste non-paramétrique dans le ROM multi-niveau permet d'obtenir un ROM stochastique multi-niveau avec lequel il est possible d'attribuer un niveau d'incertitude spécifique à chaque ROB. L'application présentée est relative à une automobile, pour laquelle le ROM stochastique multi-niveau est identifié par rapport à des mesures expérimentales. Le ROM proposé permet d'obtenir une dimension réduite ainsi qu'une prévision améliorée, en comparaison avec un ROM stochastique classique.

Résumé court

Pour des structures dynamiques complexes comportant plusieurs échelles structurales, de nombreux déplacements locaux peuvent être entremêlés avec les déplacements globaux habituels, induisant un recouvrement des régimes vibratoires basses, moyennes et hautes fréquences (BF, MF, HF). D'où l'introduction d'un modèle réduit (ROM) multi-niveau, basé sur trois bases réduites (ROBs) constituées de déplacements de type BF, MF ou bien HF. Ces ROBs sont obtenues via une méthode de filtrage utilisant des fonctions de forme globales pour l'énergie cinétique. Grâce au filtrage de déplacements locaux, la dimension du ROM multi-niveau est réduite, comparée à l'analyse modale classique. Un modèle probabiliste non-paramétrique permet d'obtenir un ROM stochastique multi-niveau avec un niveau d'incertitudes spécifique pour chacune des ROBs. La méthode est appliquée à une voiture, pour laquelle le ROM stochastique multi-niveau est identifié expérimentalement, en résolvant un problème statistique inverse.

Contents

Notations

DOF: degree of freedom.
FEM: finite element model.
FRF: frequency response function.
HF: high frequency.
LF: low frequency.
MF: medium frequency (or mid frequency).
ROB: reduced-order vector basis.
ROM: reduced-order model.

C-NROM: classical nominal ROM.
C-SROM: classical stochastic ROM.
ML-NROM: multilevel nominal ROM.
ML-SROM: multilevel stochastic ROM.

$\mathbb{C}^p$: Hermitian space of dimension p.
$\mathbb{R}^p$: Euclidean space of dimension p.
$\mathcal{S}_c$: vector subspace for the classical ROM.
$\mathcal{S}_g$: vector subspace for the global-displacements ROM.
$\mathcal{S}_\ell$: vector subspace for the local-displacements ROM.
$\mathcal{S}_t$: vector subspace for the multilevel ROM.

$\mathcal{S}_\mathcal{H}$: vector subspace for the scale-$\mathcal{H}$ ROM.
$\mathcal{S}_\mathcal{L}$: vector subspace for the scale-$\mathcal{L}$ ROM.
$\mathcal{S}_\mathcal{M}$: vector subspace for the scale-$\mathcal{M}$ ROM.
$\mathcal{S}_\mathcal{R}$: vector subspace for the reduced kinematics.
$\mathcal{S}_{\mathcal{LM}}$: vector subspace for the scale-$\mathcal{LM}$ ROM.

d: maximum degree of the polynomial approximation.
m: dimension of the FEM (number of DOFs).

n: dimension of $\mathcal{S}_c$.
r: dimension of $\mathcal{S}_\mathcal{R}$.
n_g: dimension of $\mathcal{S}_g$.
n_ℓ: dimension of $\mathcal{S}_\ell$.
n_t: dimension of $\mathcal{S}_t$.
$n_\mathcal{H}$: dimension of $\mathcal{S}_\mathcal{H}$.
$n_\mathcal{L}$: dimension of $\mathcal{S}_\mathcal{L}$.
$n_\mathcal{M}$: dimension of $\mathcal{S}_\mathcal{M}$.
$n_{\mathcal{LM}}$: dimension of $\mathcal{S}_{\mathcal{LM}}$.

$[B]$: ROB of $\mathcal{S}_\mathcal{R}$ such that $[B]^T[\mathbb{M}][B] = [I_r]$.
$[B^\ell]$: ROB of $\mathcal{S}_\mathcal{R}$ such that $[B^\ell]^T[\mathbb{M}^\ell][B^\ell] = [I_r]$.
$[I_p]$: identity matrix of dimension p.
$[\mathbb{M}]$: mass matrix of the FEM.
$[\mathbb{M}^\ell]$: lumped approximation of $[\mathbb{M}]$.

$[\Phi]$: ROB of the classical ROM.
$[\Phi^g]$: global-displacements ROB.
$[\Phi^\ell]$: local-displacements ROB.
$[\Phi^t]$: ROB of the scale-t ROM.
$[\Phi^\mathcal{H}]$: HF-type displacements ROB.
$[\Phi^\mathcal{L}]$: LF-type displacements ROB.
$[\Phi^\mathcal{M}]$: MF-type displacements ROB.
$[\Phi^{\mathcal{LM}}]$: ROB of the scale-$\mathcal{LM}$ ROM.
$[\Psi]$: ROB of the multilevel ROM.

Chapter 1

Introduction

1.1 Context of the research

This work deals with an extension of the classical construction of reduced-order models (ROMs) that are obtained through modal analysis in computational linear structural dynamics, an extension that is based on a multilevel projection strategy, for complex structures with uncertainties.

Nowadays, it is well recognized that the predictions in structural dynamics over a broad frequency band by using a computational model, based on the finite element method [1, 2, 3], must be improved in taking into account the model uncertainties induced by the modeling errors, for which the role increases with the frequency. This means that any model of uncertainties must account for this type of frequency evolution. In addition, it is also admitted that the parametric probabilistic approach of uncertainties is not sufficiently efficient for reproducing the effects of modeling errors. In such a framework, the nonparametric probabilistic approach of uncertainties can be used, but in counter part requires the introduction of a ROM for implementing it. Consequently, these two aspects, frequency-evolution of the uncertainties and reduced-order modeling, lead us to consider the development of a multilevel ROM in computational structural dynamics, which has the capability to adapt the level of uncertainties to each part of the frequency band. This is the purpose of the thesis.

In structural dynamics, the low-frequency (LF) band is generally characterized by a low modal density and by frequency response functions (FRFs) exhibiting isolated resonances. These are due to the presence of long-wavelength displacements, which are global (the concept of global displacement will be clarified later).

In contrast, the high-frequency (HF) band is characterized by a high modal density and by rather smooth FRFs, these being due to the presence of numerous short-wavelength displacements. The intermediate band, the medium-frequency (MF) band, presents a non-uniform modal density and FRFs with overlapping resonances [4]. For the LF band, modal analysis [5, 6, 7, 8, 9, 10, 11, 12, 13, 14] is a well-known effective and efficient method, which usually provides a small-dimension ROM whose reduced-order basis (ROB) is constituted of the first elastic modes (i.e. the first structural vibration modes). Energy methods, such as statistical energy analysis [15, 16, 17, 18, 19, 20, 21, 22, 23, 24, 25], are commonly used for the HF band analysis. Various methods have been proposed for analyzing the MF band. A part of these methods are related to deterministic solvers devoted to the classical deterministic linear dynamical equations [4, 26, 27, 28, 9, 29, 30, 31, 32, 33, 34, 35]. A second part are devoted to stochastic linear dynamical equations that have been developed for taking into account the uncertainties in the computational models in the MF band (which plays an important role in this band), see for instance [36, 37, 38, 39, 40, 41, 42, 43].

In order to illustrate the definitions of the LF, MF, and HF bands, a typical FRF is shown in Fig. 1.1.

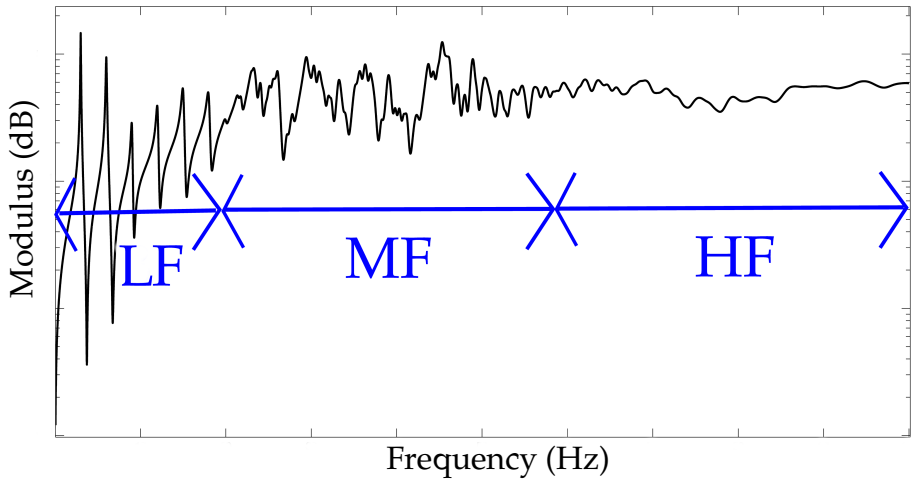

Figure 1.1: Typical FRF including the LF, MF, and HF bands: modulus in dB scale with respect to the frequency.

1.2 Position of the research

In this work, we are interested in the dynamical analysis of complex structures in a broad frequency band. By complex structure is intended a structure with complex geometry, constituted of heterogeneous materials and more specifically, characterized by the presence of several structural levels, for instance, a structure that is made up of a stiff main part embedding various flexible sub-parts. For such structures, it is possible having, in addition to the usual global-displacements elastic modes associated with their stiff skeleton, the apparition of numerous local elastic modes, which correspond to predominant vibrations of the flexible sub-parts. In Figs. 1.2 and 1.3 are depicted the mode shapes of respectively the first and the third elastic modes of a car body structure. The gray intensity is related to the level of amplitude of the displacements (the greater amplitude is the lighter). Throughout this document, any other plot of deformation shape will follow the same rule. The first elastic mode (involving a localized deformation of a flexible part at the front-right of the car) is considered as local whereas the other one is considered as a global elastic mode (involving a global torsion of the car).

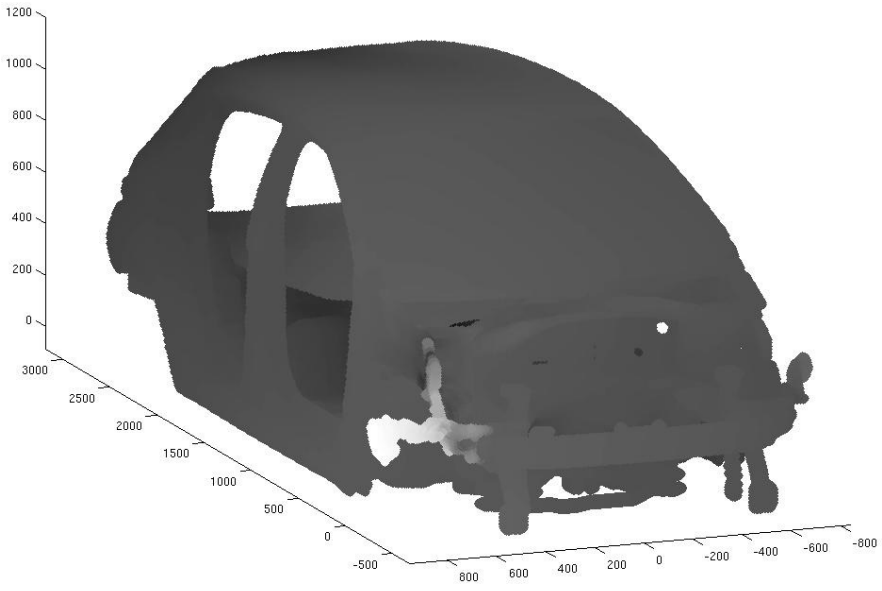

Figure 1.2: Mode shape of a local elastic mode of a car body structure (eigenfrequency 24 Hz).

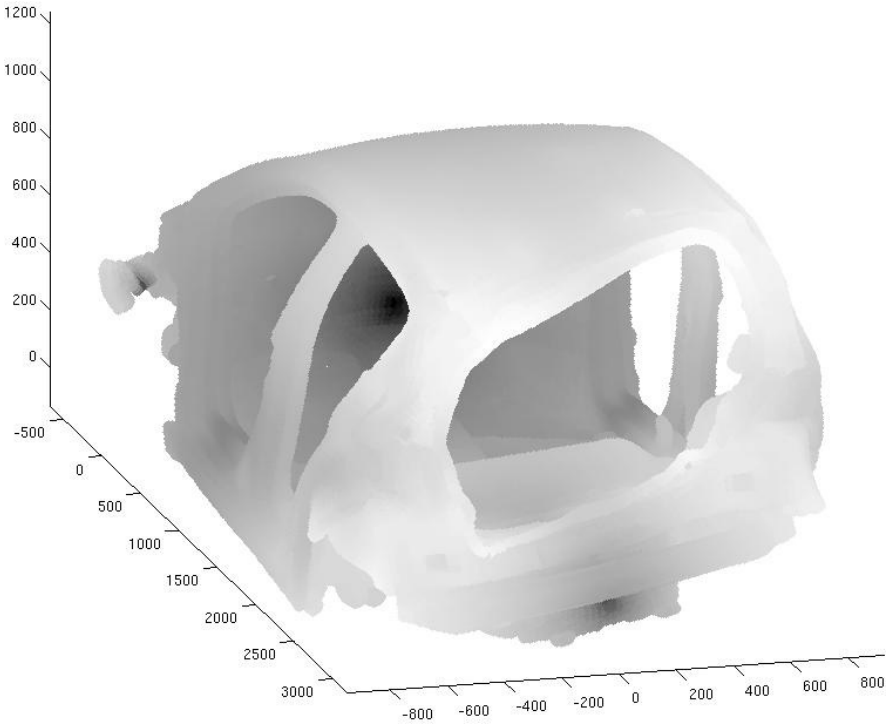

Figure 1.3: Mode shape of a global elastic mode of a car body structure (eigenfrequency 39 Hz).

For such complex structures, which can be encountered for instance in aeronautics, aerospace, automotive (see for instance [44, 45, 46, 47]), or nuclear industries, two main difficulties arise from the presence of the local displacements. First, the modal density may substantially increase as soon as low frequencies, leading to high-dimension ROMs within modal analysis (with potentially thousands of elastic modes in low frequencies). Second, such ROMs may suffer from a lack of robustness with respect to uncertainty, because of the presence of the numerous local displacements, which are known to be very sensitive to uncertainties. It should be noted that, for such a complex structure, the engineering objectives may consist in the prediction of the global displacements only, that is to say on predicting the FRFs of observation points belonging to the stiff parts.

There is not much research devoted to the dynamic analysis of structures characterized by the presence of numerous local elastic modes intertwined with the global elastic modes. In the framework of experimental modal analysis, techniques for the spatial filtering of the short wavelengths have been proposed [48], based on regularization schemes [49]. In the framework of computational models, the Guyan condensation technique [50], based on the introduction of master nodes at which the inertia is concentrated, allows for the filtering of local displacements.

The selection of the master nodes is not obvious for complex structures [51]. Filtering schemes based on the lumped mass matrix approximations have been proposed [52, 53, 54], but the filtering depends on the mesh and cannot be adjusted. In [16] a basis of global displacements is constructed using a coarse mesh of a finite element model, which, generally, gives big errors for the elastic energy. In order to extract the long-wavelength free elastic modes of a master structure, the free-interface substructuring method has been used [35]. Other computational methods include image processing [55] for identifying the global elastic modes, the global displacements as eigenvectors of the frequency mobility matrix [56], or the extrapolation of the dynamical response using a few elastic modes [57]. In the framework of slender dynamical structures, which exhibit a high modal density in the LF band, simplified equivalent models [58, 59] using beams and plates, or homogenization [60] have been proposed. Using these approaches, the construction of a simplified model is not automatic, requires an expertise, and a validation procedure remains necessary. In addition, these approximations are only valid for the LF band.

For a complex structure for which the elastic modes may not be either purely global elastic modes or purely local elastic modes, the increasing of the dimension of the ROM that is constructed by using the classical modal analysis can be troublesome. The methodology that would consist in sorting the elastic modes according to whether they be global or local cannot be used because the elastic modes are combinations of both global displacements and local displacements. In addition, due to the large amplitude of the local displacements in comparison to the global displacements, it is difficult to distinguish the global displacements based on the mode shapes (this becomes even more difficult for higher frequencies). In Fig. 1.4, we present a mode shape of an elastic mode found in the LF band, which is representative of the regular mode shapes that can be observed for the considered complex structure in this band. It allows for illustrating the fact that in general the elastic modes are not either global or local. Indeed, such mode is constituted of a global deformation of the structure assorted with local deformations of distinct structural levels (the roof, the flexible part in the left back). In Fig. 1.5, we present a mode shape of an elastic mode found in the MF band, which is representative of the regular mode shapes that can be observed for the car body structure in this band. It allows for illustrating the fact that, as the frequency increases, the global displacements within the elastic modes are becoming less and less perceptible: most of the mode shapes are dominated by large-amplitude local displacements that are irregularly distributed over the structure. Another solution would consist in using substructuring techniques for which reviews can be found in [61, 62, 63] and for which a state of the art has

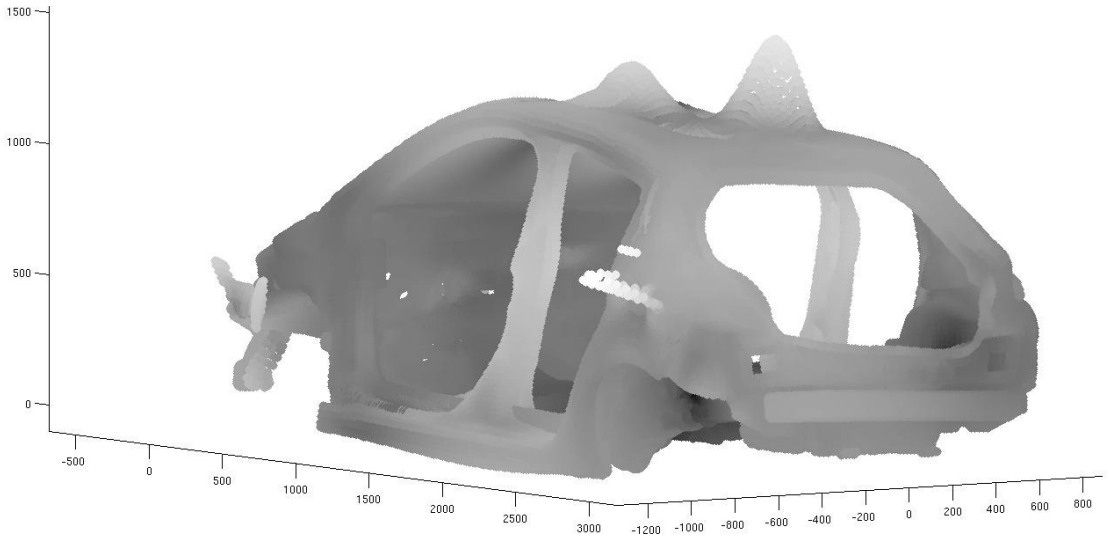

Figure 1.4: Mode shape of a regular low-frequency elastic mode of a car body structure (eigenfrequency 72 Hz).

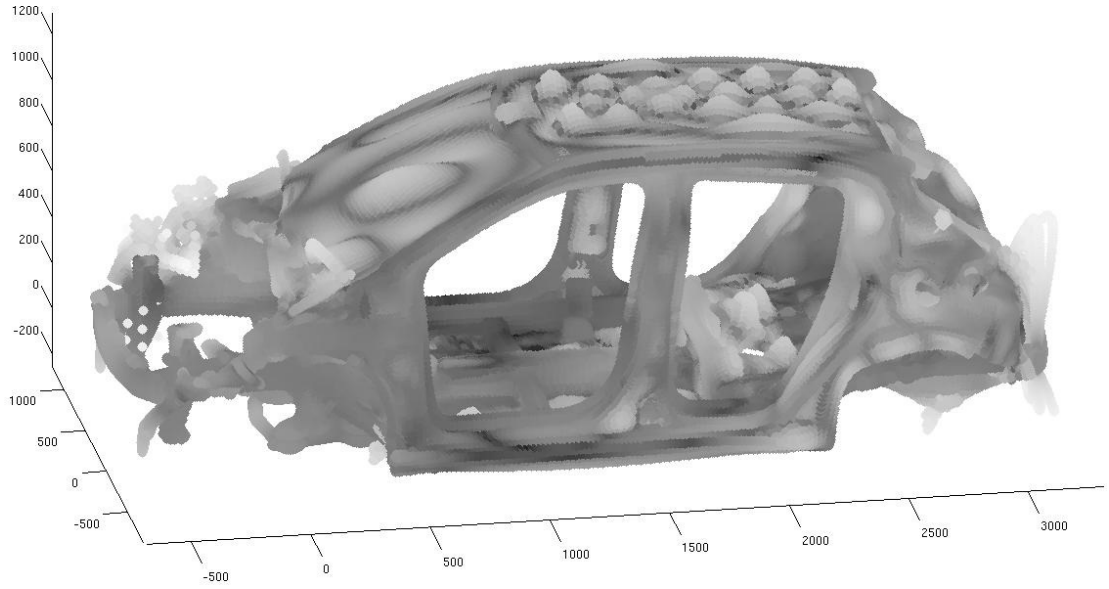

Figure 1.5: Mode shape of a regular medium-frequency elastic mode of a car body structure (eigenfrequency 262 Hz).

recently been done in [64]. A brief summary is given hereinafter. The concept of substructures was first introduced by Argyris and Kelsey in 1959 [65] and by Przemieniecki in 1963 [66] and was extended by Guyan and Irons [50, 67]. Hurty [68, 69] considered the case of two substructures coupled through a geometrical

interface. Finally, Craig and Bampton [70] adapted the Hurty method. Improvements have been proposed with many variants [71, 72, 73, 74, 75], in particular for complex dynamical systems with many appendages considered as substructures (such as a disk with blades) Benfield and Hruda [76]. Another type of methods has been introduced in order to use the structural modes with free geometrical interface for two coupled substructures instead of the structural modes with fixed geometrical interface (elastic modes) as used in the Craig and Bampton method and as proposed by MacNeal [77] and Rubin [78]. The Lagrange multipliers have also been used to write the coupling on the geometrical interface [79, 80, 81, 82].

The substructuring techniques would require to discard the component modes associated with flexible sub-parts, hence removing their associated local displacements. Unfortunately, for the complex structures considered, there is no clear separation between the skeleton and the substructures for which the displacements would be local. For instance, with fixed thickness, the curvatures of a shell can lead to stiffened zones with respect to the rigidity of the flat zones. Consequently, in addition to the various embedded equipments within the structure, the complex geometry of the structure is responsible for the fact that there can be no separation of the several structural levels, but rather a continuous series of structural levels. In such conditions, the notion of local displacement is relative. Figures 1.6 and 1.7 show two complementary points of view of a car body struc-

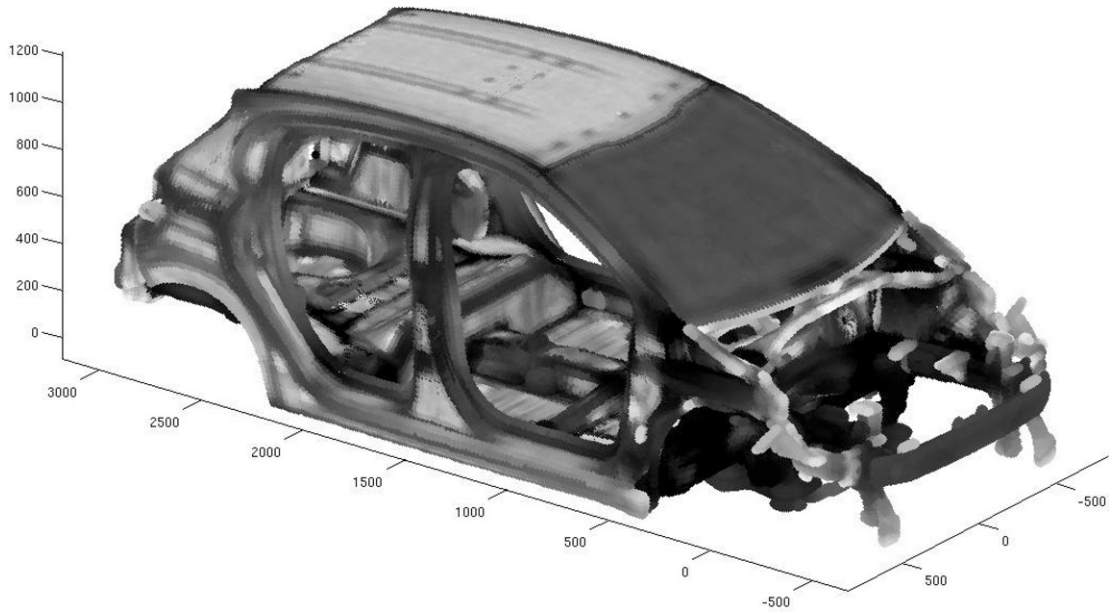

Figure 1.6: Computational model of a car body structure, in which the gray intensity is related to the level of rigidity (the darker is the stiffer).

ture, in which it can be seen that a stiff skeleton emerges among several structural levels. In addition, there are numerous flexible parts spread over the whole structure (not only well identified components such as the roof or the floor panels, but also erratically distributed flexible parts, see for instance the parts located at the front of the car). It allows for illustrating the fact that no clear boundary can be defined between the structural scales.

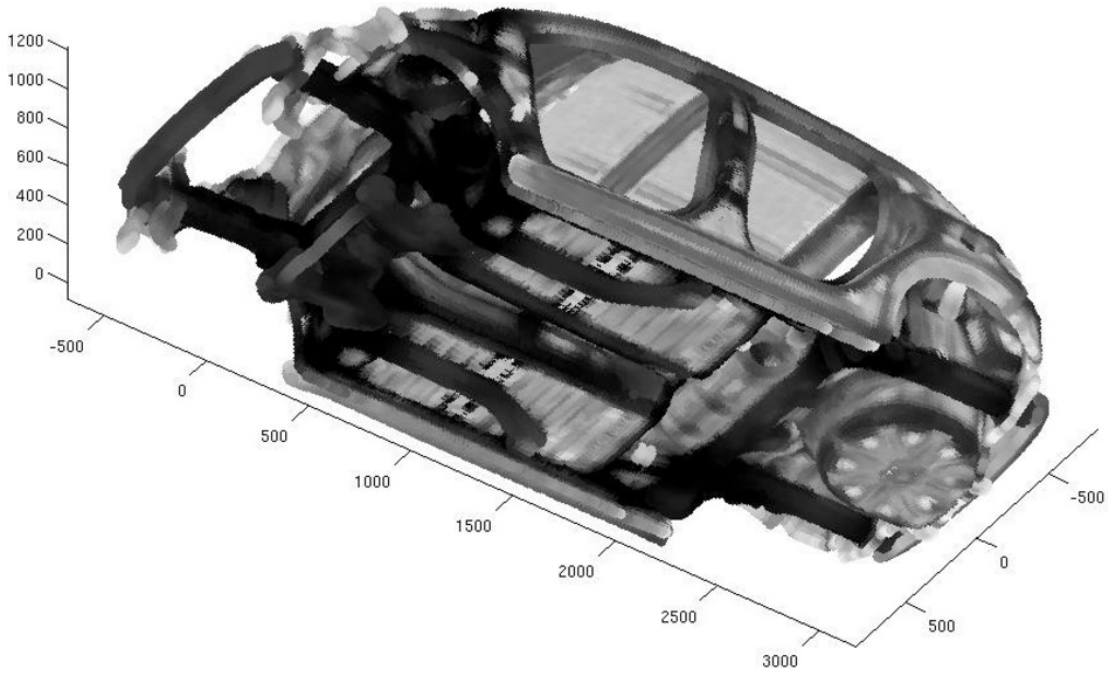

Figure 1.7: Computational model of a car body structure, in which the gray intensity is related to the level of rigidity (the darker is the stiffer).

It should be noted that, in contrast to the usual long-wavelength global displacements of the LF band, the local displacements associated with the structural sub-levels, which can then also appear in the LF band, are characterized by short wavelengths, similarly to HF displacements. As a result, for the complex structures considered, there is an overlap of the three vibration regimes, LF, MF, and HF.

Concerning the taking into account of uncertainties in the computational model, the probabilistic framework is well adapted to construct the stochastic models, for the stochastic solvers, and for solving the associated statistical inverse problems for the identification of the stochastic models, for the finite dimension and for the infinite dimension. Hereinafter, we present a brief background that is limited to

the probabilistic framework for uncertainty quantification. As a function of the sources of uncertainties in the computational model (model-parameter uncertainties and model uncertainties induced by modeling errors) and of the variabilities in the real dynamical system, several probabilistic approaches can be used.
(i) *Output-predictive error method.* Several methods are currently available for analyzing model uncertainties. The most popular one is the standard output-predictive error method introduced in [83]. This method has a major drawback because it does not enable the ROM to learn from data.
(ii) *Parametric probabilistic methods for model-parameter uncertainties.* An alternative family of methods for analyzing model uncertainties is the family of parametric probabilistic methods for the uncertainty quantification. This approach is relatively well developed for model-parameter uncertainties, at least for a reasonably small number of parameters. It consists in constructing prior and posterior stochastic models of uncertain model parameters pertaining, for example, to geometry, boundary conditions, material properties, etc [84, 85, 86, 87, 88, 89, 90, 91, 92, 93, 94, 95, 96]. This approach was shown to be computationally efficient for both the computational model and its associated ROM (for example, see [97, 98]), and for large-scale statistical inverse problems [99, 100, 101, 102, 103, 104]. However, it does not take into account neither the model uncertainties induced by modeling errors introduced during the construction of the computational model, nor those due to model reduction.
(iii) *Nonparametric probabilistic approach for modeling uncertainties.* For modeling uncertainties due to more general modeling errors, a nonparametric probabilistic approach was introduced in [105], in the context of linear structural dynamics. The methodology is in two steps. For the first one, a linear ROM of dimension n is constructed by using the linear computational model with m degrees of freedom (DOFs) and a ROB of dimension n. For the second step, a linear stochastic ROM is constructed by substituting the deterministic matrices underlying the linear ROM with random matrices for which the probability distributions are constructed using the Maximum Entropy (MaxEnt) principle [106, 107]. The construction of the linear stochastic ROM is carried out under the constraints generated from the available information such as some algebraic properties (positiveness, integrability of the inverse, etc.) and some statistical information (for example, the equality between mean and nominal values). This nonparametric probabilistic approach has been extended for different ensembles of random matrices and for linear boundary value problems [108, 109]. It was also experimentally validated and applied for linear problems in composites [110], viscoelasticity [111], dynamic substructuring [112, 113, 114], vibroacoustics [44, 43], robust design and optimization [115], etc. More recently, the nonparametric approach has been extended to take into account some nonlinear geometrical effects

in structural analysis [116, 117], but it does not hold for arbitrary nonlinear systems, while the work recently published [118] allows for taking into account any nonlinearity in a ROM.

In addition, the real systems exhibit variabilities: for a given design of a structure, the associated manufactured objects exhibit variations, which result in dispersed FRFs. It can be explained by the manufacturing process and by the small differences in the design configurations. It should be noted that, in general, the variability of the real system increases with the frequency. Figure 1.8 presents a set of 20 trajectories obtained measuring, under the same conditions, the FRF (modulus in log scale of the acceleration at a given location) of 20 nominally identical automobiles. One can see that the dispersion increases with the frequency.

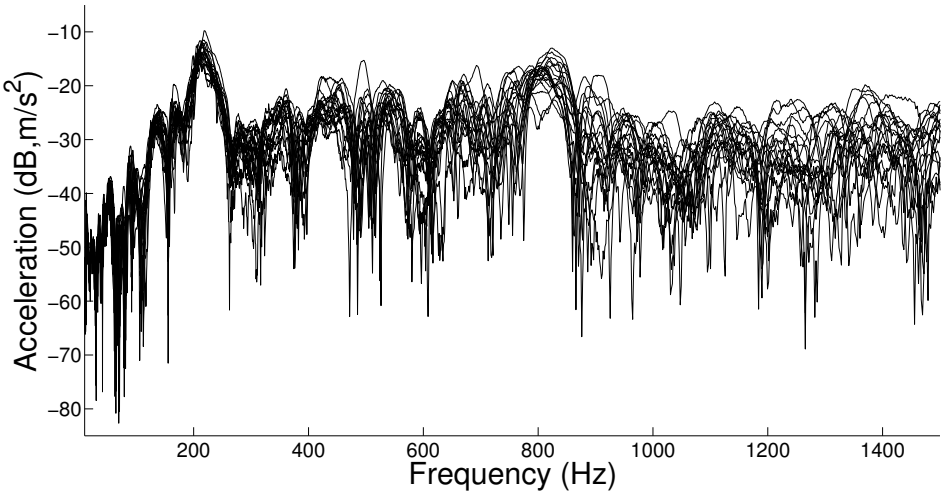

Figure 1.8: Experimental measurements of 20 FRFs on a broad frequency band performed on PSA cars of the same type [119].

1.3 Objectives of the research

As previously explained, for the complex structures considered, numerous local elastic modes are intertwined with the usual global elastic modes. The resulting high modal density and overlap of the LF, MF, and HF vibration regimes (presence of small-wavelength HF-type displacements with the usual large-wavelength global displacements of the LF band) induces two major difficulties, pertaining to uncertainty quantification and to computational efficiency.

The objective of this thesis is thus double. First, to provide a multilevel stochastic ROM that is able to take into account the heterogeneous variability introduced by the overlap of the three vibration regimes. Second, to provide a predictive ROM whose dimension is decreased with respect to the classical ROM constructed by using the modal analysis method. Both these objectives are to be fulfilled by means of efficient methods that are non-intrusive with respect to commercial software.

1.4 Strategy of the research

Recently, a new methodology [120] has been proposed for constructing a stochastic ROM devoted to dynamical structures having numerous local elastic modes in the low-frequency range. The stochastic ROM is obtained by implementing the nonparametric probabilistic approach of uncertainties within a novel ROM whose ROB is constituted of two families: one of global displacements and another of local displacements. These families are obtained through the introduction, for the kinetic energy, of a projection operator associated with a subspace of piecewise constant functions. The spatial dimension of the subdomains, in which the projected displacements are constant, and which constitute a partition of the domain of the structure, allows for controlling the filtering between the global displacements and the local displacements. These subdomains can be seen as macro-elements, within which, using such an approximation, no local displacement is permitted. It should be noted that the generation of a domain partition for which the generated subdomains have a similar size (that we call *uniform domain partition*), necessary for obtaining a spatially uniform filtering criterion, is not trivial for complex geometries. Based on the Fast Marching Method [121, 122], a general method has been developed in order to perform the uniform domain partition for a complex finite element mesh, and then implemented for the case of automobile structures [45, 46]. Published papers related to the methodology are given in [120, 45, 46, 123, 124]. Related to a part of these papers, a former PhD thesis [125] was defended in 2012. In the present thesis (see [126, 127, 128, 129, 130, 131, 132]), the filtering methodology is generalized through the introduction of a computational framework for the use of any arbitrary approximation subspace for the kinetic energy, in place of the piecewise constant approximation. In particular, polynomial shape functions (with support the whole domain of the structure) are used for constructing a global-displacements ROM for an automobile. This generalization allows for carrying out an efficient convergence of the global-displacements ROM with respect to the so-defined filtering

(in contrast, constructing several uniform domain partitions of different characteristic sizes can be, in practice, very time-consuming). In addition, a multilevel ROM is introduced, whose ROB is constituted of several families of displacements, which correspond to the several structural levels of the complex structure. More precisely, a multilevel ROM whose ROB is constituted of three families, namely the LF-, MF-, and HF-type displacements (successively, using several filterings), is presented. The multilevel ROM allows for implementing a probabilistic model of uncertainties that is adapted to each vibration regime. This way, the amount of statistical fluctuations for the LF-, MF-, and HF-type displacements can be controlled using the multilevel stochastic ROM that is obtained.
An alternative construction of a multilevel stochastic ROM has been proposed in [129], but for which the implementation by using the non-intrusive algorithm proposed in this thesis would not be possible.
It should be noted that multilevel substructuring techniques can be found in the literature [133, 134, 135], but for which the purpose is to accelerate the solution of large-scale generalized eigenvalue problems.

1.5 Manuscript layout

The thesis is organized as follows. In Chapter 2, the reference computational model is introduced, followed by the classical construction of the ROM that is performed by using modal analysis, on which the classical stochastic ROM is then implemented by using the nonparametric probabilistic approach of uncertainties. In Chapter 3, the methodology devoted to the filtering of the global and of the local displacements is presented, which is then used in Chapter 4 for defining the multilevel ROM. In this chapter, the numerical procedure is also detailed and the construction of the multilevel stochastic ROM is given. Finally, in Chapter 5, the proposed methodology is applied to an automobile, for which the multilevel stochastic ROM is identified by using experimental measurements, and for which its results are compared to those of the classical stochastic ROM.

Chapter 2

Classical reduced-order model

In this chapter, in addition to the reference computational model, we present the very well known modal analysis method as well as the construction of the associated stochastic ROM that is obtained by using the nonparametric probabilistic approach of uncertainties [105]. This way, basic notions that will be reused later are introduced. In addition, the multilevel stochastic ROM proposed in this work will be compared to latter classical stochastic ROM.

2.1 Reference computational model

The vibration analysis is performed over a broad frequency band – denoted as $\mathcal{B}$ – by using the finite element method. Let m denote the dimension (number of DOFs) of the finite element model. For all angular frequency ω belonging to $\mathcal{B} = [\omega_{\min}, \omega_{\max}]$, the m-dimensional complex vector $\mathbb{U}(\omega)$ of displacements is the solution of the matrix equation,

$$(-\omega^2[\mathbb{M}] + i\omega[\mathbb{D}] + [\mathbb{K}])\, \mathbb{U}(\omega) = \mathbb{F}(\omega)\,, \tag{2.1}$$

in which $\mathbb{F}(\omega)$ is the m-dimensional complex vector of the external forces and where, assuming the structure is fixed on a part of its boundary, $[\mathbb{M}]$, $[\mathbb{D}]$, and $[\mathbb{K}]$ are the positive-definite symmetric $(m \times m)$ real mass, damping, and stiffness matrices.

In practice, dimension m of the reference (or high-fidelity) computational model can be very high (millions of DOFs). Nevertheless, matrices $[\mathbb{M}]$, $[\mathbb{D}]$, and $[\mathbb{K}]$ are sparse. However, Eq. (2.1) has to be solved for the frequency sampling and possibly, for several external loadings. In addition, whole this computation must

be done several times for implementing the Monte-Carlo method for uncertainty quantification and also, for instance, in the context of a robust design, for which a sampling of the design parameters has to be considered. In this context and for complex structures, the introduction of ROMs is necessary for making such computation tractable. In this thesis, we consider ROMs that are defined upon their projection basis (that is to say their ROB), and which consist in using this projection basis in order to project the equations associated with the reference computational model. The ROB has to be constructed so that the associated vector subspace consists of a good representation of the solution of the dynamical problem. The steps for constructing the ROM are often referred to as the *offline stage*, and the stage during which the ROM is used for performing the actual simulation (including design optimization, stochastic analysis, etc.) is referred to as the *online stage*. It should be noted that, in this context, the reduction of the computational effort devoted to the offline stage is not of the greatest concern. Instead, the reduction of the computational effort devoted to the online stage, made possible through the use of a small-dimension ROM, is of great interest for handling large-scale simulations (independently of the computational effort required for the construction of the ROM). In next Section 2.2, the classical ROM, for which the ROB is constituted of the first elastic modes, is presented. For complex structures exhibiting numerous local elastic modes as soon the LF band, the solution of the generalized eigenvalue problem associated with the conservative linear dynamical system, for which the eigenvectors are the elastic modes, can involve a great computational effort (corresponding to the offline stage), due to the high modal density resulting from the presence of the local elastic modes. It should be noted that this increased computational effort for the offline stage is negligible compared to the increased computational effort induced by the use of a high-dimension ROM for the online stage (high dimension due to the presence of numerous local elastic modes in the ROB). In Chapter 3, a methodology for the construction of a small-dimension ROM is presented, based on the use of a ROB that is constituted of global displacements.

2.2 Classical nominal reduced-order model

For all $\alpha = 1, \ldots, m$ the elastic modes $\boldsymbol{\varphi}_\alpha$ with associated eigenvalues λ_α are the solutions of the generalized eigenvalue problem,

$$[\mathbb{K}]\boldsymbol{\varphi}_\alpha = \lambda_\alpha [\mathbb{M}]\boldsymbol{\varphi}_\alpha \,. \tag{2.2}$$

The first n eigenvalues verify $0 < \lambda_1 \leq \lambda_2 \leq \ldots \leq \lambda_n < +\infty$ and the normalization that is chosen for the eigenvectors is such that

$$[\Phi]^T[\mathbb{M}][\Phi] = [I_n]\,, \tag{2.3}$$

in which $[\Phi] = [\boldsymbol{\varphi}_1 \ldots \boldsymbol{\varphi}_n]$, and where $[I_n]$ is the identity matrix of dimension n. Such a normalization with unit generalized mass is always adopted in this document, in which several generalized eigenvalue problems are introduced. In practice, only the first n elastic modes with $n \ll m$ (associated with the lowest eigenvalues or lowest eigenfrequencies $f_\alpha = \sqrt{\lambda_\alpha}/2\pi$ in Hz) are calculated. The $(m \times n)$ real matrix $[\Phi]$ is the ROB of the classical nominal reduced-order model (C-NROM). The vector subspace spanned by the ROB of the C-NROM is denoted by $\mathcal{S}_c$. Using the C-NROM, displacements $\mathbb{U}(\omega)$ belong to $\mathcal{S}_c$ and we have

$$\mathbb{U}(\omega) \simeq [\Phi]\mathfrak{q}(\omega) = \sum_{\alpha=1}^{n} \mathfrak{q}_\alpha(\omega)\, \boldsymbol{\varphi}_\alpha\,, \tag{2.4}$$

where the n-dimensional complex vector of generalized coordinates $\mathfrak{q}(\omega) = (\mathfrak{q}_1(\omega) \ldots \mathfrak{q}_n(\omega))$ is the solution of the reduced-matrix equation,

$$(\,-\omega^2[\mathcal{M}] + i\omega[\mathcal{D}] + [\mathcal{K}]\,)\,\mathfrak{q}(\omega) = \mathfrak{f}(\omega)\,, \tag{2.5}$$

in which $\mathfrak{f}(\omega) = [\Phi]^T\mathbb{F}(\omega)$, $[\mathcal{D}] = [\Phi]^T[\mathbb{D}][\Phi]$ is, in general, a full matrix, and where diagonal matrices $[\mathcal{K}]$ and $[\mathcal{M}]$ are such that

$$[\mathcal{K}] = [\Phi]^T[\mathbb{K}][\Phi] = [\Lambda]\,, \quad [\mathcal{M}] = [\Phi]^T[\mathbb{M}][\Phi] = [I_n]\,, \tag{2.6}$$

in which $[\Lambda]$ is the matrix of the first n eigenvalues.

2.3 Classical stochastic reduced-order model

The classical stochastic reduced-order model (C-SROM) is constructed by using the nonparametric probabilistic approach of uncertainties [105] within the C-NROM. In this nonparametric approach, each nominal reduced matrix of dimension n, say $[\mathcal{A}]$ (= $[\mathcal{M}]$, $[\mathcal{D}]$, or $[\mathcal{K}]$), is replaced by a random matrix, $[\boldsymbol{\mathcal{A}}]$ (= $[\boldsymbol{\mathcal{M}}]$, $[\boldsymbol{\mathcal{D}}]$, or $[\boldsymbol{\mathcal{K}}]$), whose probability distribution has been constructed by using the maximum entropy principle [106, 107] under the following constraints:

- Matrix $[\boldsymbol{\mathcal{A}}]$ is with values in the set of all the positive-definite symmetric $(n \times n)$ real matrices.
- $E\{[\boldsymbol{\mathcal{A}}]\} = [\mathcal{A}]$, with E the mathematical expectation: the mean matrix is

chosen as the nominal matrix.

- $E\{|||[\boldsymbol{\mathcal{A}}]^{-1}||_F^2\} < +\infty$, with $||.||_F$ the Frobenius norm, for insuring the existence of a second-order solution of the stochastic ROM.

The construction of random matrix $[\boldsymbol{\mathcal{A}}]$ is given by

$$[\boldsymbol{\mathcal{A}}] = [L_{\mathcal{A}}]^T [\mathbf{G}_n(\delta_{\mathcal{A}})][L_{\mathcal{A}}]\,, \tag{2.7}$$

where, using the Cholesky factorization $[\mathcal{A}] = [L_{\mathcal{A}}]^T[L_{\mathcal{A}}]$ with upper-triangular $[L_{\mathcal{A}}]$, the random matrix $[\mathbf{G}_n(\delta_{\mathcal{A}})]$, whose construction is given in [105], is positive-definite almost surely, with mean value $[I_n]$, and is parameterized by a dispersion parameter $\delta_{\mathcal{A}}$ that is defined by

$$\delta_{\mathcal{A}}^2 = \frac{1}{n}\, E\{|||[\mathbf{G}_n(\delta_{\mathcal{A}})] - [I_n]||_F^2\}\,. \tag{2.8}$$

Hyperparameter $\delta_{\mathcal{A}}$ of random matrix $[\mathbf{G}_n(\delta_{\mathcal{A}})]$ has to verify $0 < \delta < \delta_{\max}$, with $\delta_{\max}$ given by

$$\delta_{\max} = \sqrt{\frac{n+1}{n+5}}\,. \tag{2.9}$$

The construction of $[\mathbf{G}_n(\delta_{\mathcal{A}})]$ proceeds from the application of the maximum entropy principle under the following constraints:

- Matrix $[\mathbf{G}_n(\delta_{\mathcal{A}})]$ is with values in the set of all the positive-definite symmetric $(n \times n)$ real matrices.
- $E\{[\mathbf{G}_n(\delta_{\mathcal{A}})]\} = [I_n]\,.$
- $E\{|||[\mathbf{G}_n(\delta_{\mathcal{A}})]^{-1}||_F^2\} < +\infty\,.$

We now give the results for the random generation of matrix $[\mathbf{G}_n(\delta_{\mathcal{A}})]$. It can be written as $[\mathbf{G}_n(\delta_{\mathcal{A}})] = [\mathbf{L}_G(\delta_{\mathcal{A}})]^T\,[\mathbf{L}_G(\delta_{\mathcal{A}})]$, in which the $(n \times n)$ upper-triangular random matrix $[\mathbf{L}_G(\delta_{\mathcal{A}})]$ is defined through its components as:

$$\text{for } i < j \qquad [\mathbf{L}_G(\delta_{\mathcal{A}})]_{ij} = \delta_{\mathcal{A}}(n+1)^{-1/2} U_{ij}\,, \tag{2.10}$$

$$\text{for } i = j \qquad [\mathbf{L}_G(\delta_{\mathcal{A}})]_{ij} = \delta_{\mathcal{A}}(n+1)^{-1/2}\sqrt{2V_i}\,, \tag{2.11}$$

in which the random variables $\{U_{ij}\}_{ij}$ are independent copies of a standard Normal random variable and where the random variables $\{V_i\}_i$ are independent and are such that V_i is a Gamma random variable with shape parameter $\alpha_i = 2\delta_{\mathcal{A}}^2/(n+$

$1 + \delta_{\mathcal{A}}^2(1-i))$ depending on i and with rate parameter $\beta = 1$. The expression for the gamma distribution f_G is the following,

$$f_G(x;\alpha,\beta) = \frac{\beta^\alpha x^{\alpha-1} e^{-x\beta}}{\Gamma(\alpha)}\,, \tag{2.12}$$

in which gamma function $\Gamma(\alpha)$ is given by

$$\Gamma(\alpha) = \int_0^{+\infty} t^{\alpha-1} e^{-t} dt\,. \tag{2.13}$$

Using the Monte-Carlo simulation method [136], the C-SROM allows for computing the random displacements $\mathbf{U}(\omega)$ associated with $\mathbb{U}(\omega)$,

$$\mathbf{U}(\omega) = [\Phi]\boldsymbol{\mathcal{Q}}(\omega), \tag{2.14}$$

in which the random complex vector $\boldsymbol{\mathcal{Q}}(\omega)$ of the generalized coordinates is obtained by solving the random matrix-equation,

$$(\,-\omega^2[\boldsymbol{\mathcal{M}}] + i\omega[\boldsymbol{\mathcal{D}}] + [\boldsymbol{\mathcal{K}}]\,)\,\boldsymbol{\mathcal{Q}}(\omega) = \mathfrak{f}(\omega)\,. \tag{2.15}$$

The Monte-Carlo simulation method consists in performing the calculation several times using realizations of the random variables involved in the probabilistic model. In Eq. (2.15), it allows for propagating uncertainties from the system matrices $[\boldsymbol{\mathcal{M}}]$, $[\boldsymbol{\mathcal{D}}]$, $[\boldsymbol{\mathcal{K}}]$ to the output FRFs $\mathbf{U}(\omega)$.

The classical ROM presented in this Section 2 is built upon the use of the elastic modes that are present in frequency band of analysis $\mathcal{B}$ (or a little further). In this manner, the size of the model is reduced while preserving its accuracy for this band. For the complex structures under consideration, numerous local displacements are intertwined with the global displacements. As a result, among the elastic modes present in $\mathcal{B}$, many have little contribution to the robust dynamical response of the stiff skeleton of the structure that is provided by the C-SROM. Consequently, we present the construction of an adapted ROM that is based on a ROB from which some local displacements have been filtered.

Chapter 3

Global-displacements reduced-order model

In this chapter, we present the construction of a new ROM that is based on the use of a global-displacements ROB, instead of the classical ROB of elastic modes, susceptible to include numerous local displacements. In Section 3.1, we present the construction of an unusual mass matrix that is associated with a reduced kinematics for the kinetic energy. In Section 3.2, we use this mass matrix for obtaining unusual eigenvectors that constitute the global-displacements ROB (this unusual mass matrix is not used as the mass matrix for computing the response of the dynamical system). In section 3.3, an efficient and nonintrusive algorithm is proposed for implementing the ROB. Finally, in Section 3.4, we give the construction of a ROB that is constituted of the complementary local displacements that are neglected in the global-displacements ROM.

3.1 Reduced kinematics for the kinetic energy

In order to filter local displacements, a reduced kinematics is introduced for the mass matrix. This reduced kinematics is intended to be such that the local displacements cannot be represented. Instead of using local shape functions within the usual finite elements, we propose the use of r global shape functions, which span a vector subspace, $\mathcal{S}_{\mathcal{R}}$, and which constitute the columns of a $(m \times r)$ real matrix, $[B]$. It should be noted that the support of these shape functions is the whole domain of the structure and that they are approximated within the finite element basis. In this work, the reduced kinematics used consists of polynomial shape functions.

3.1.1 Construction of the polynomial basis

The objective of this section is the construction of basis matrix $[B]$ of subspace $\mathcal{S}_{\mathcal{R}}$. For all m-dimensional vector $\mathbf{v}$ belonging to $\mathcal{S}_{\mathcal{R}}$, there exists a r-dimensional real vector, $\mathbf{c}$, such that

$$\mathbf{v} = [B]\,\mathbf{c}\,. \tag{3.1}$$

In the work initialized in [120], the construction of the reduced kinematics is based on a uniform domain partition of the struture, Ω, into N_s subdomains $\Omega_1, \ldots, \Omega_{N_s}$. For complex finite element models, such domain partitioning is not a straightforward task. In [45, 46], uniform domain partitions of the finite element mesh of automobiles were performed using an algorithm [45] based on the Fast Marching Method [121, 122]. In this thesis, the use, for the kinematics reduction, of more accurate approximations (compared to the piecewise constant approximation), allows for avoiding such a domain partitioning.

3.1.1.1 Polynomial reduced kinematics

In this work, we propose a polynomial approximation of maximum degree d over the entire domain Ω of the structure. To do so, N_μ multivariate orthogonal polynomials $p_{\boldsymbol{\alpha}^{(\mu)}}$ are used, where for $\mu = 1, \ldots, N_\mu$ multi-index $\boldsymbol{\alpha}^{(\mu)}$ belongs to some set $\mathcal{K}_d$ that is defined as follows. Let $\mathcal{K}_d$ be the set of vectors $\boldsymbol{\alpha} = (\alpha_1, \alpha_2, \alpha_3)$ for which integers α_1 , α_2 , and α_3 verify

$$\alpha_3 \leq \alpha_2 \leq \alpha_1 \leq d\,. \tag{3.2}$$

It can be deduced (number of possible combinations) that,

$$N_\mu = (d+1)(d+2)(d+3)/6\,. \tag{3.3}$$

The orthogonality for the polynomials is defined with respect to mass matrix $[\mathbb{M}]$. Denoting as N_f the number of free nodes of the finite element model, the approximate displacement v_γ^j of node $\gamma \in \{1, \ldots, N_f\}$ following direction j is written as

$$v_\gamma^j = \sum_{\mu=1}^{N_\mu} p_{\boldsymbol{\alpha}^{(\mu)}}(\mathbf{x}_\gamma)\, c_\mu^j\,, \tag{3.4}$$

in which c_μ^j are the polynomials coefficients and where $\mathbf{x}_\gamma = (\mathrm{x}_\gamma, \mathrm{y}_\gamma, \mathrm{z}_\gamma)$ is the position vector of node γ at which the polynomials are evaluated. In matrix form,

the N_f equations associated with Eq. (3.4) can be rewritten as

$$\mathbf{v}^j = [\,p\,]\,\mathbf{c}^j\,, \tag{3.5}$$

in which $\mathbf{v}^j$ is the sub-vector of $\mathbf{v}$ constituted of the N_f displacements v_γ^j, $\mathbf{c}^j$ is the sub-vector of $\mathbf{c}$ constituted of the N_μ coefficients c_μ^j, and where the $(N_f \times N_\mu)$ real matrix $[\,p\,]$ is constituted of the values, at each of the N_f mesh nodes, of each of the N_μ polynomials $p_{\boldsymbol{\alpha}^{(\mu)}}$. It should be noted that the same N_μ polynomials are used for every direction j. Basis matrix $[B]$ of subspace $\mathcal{S}_\mathcal{R}$, which is such that $\mathbf{v} = [B]\,\mathbf{c}$, is then assembled using $[\,p\,]$. This assembly is such that only the 3 translational directions are considered for constructing the reduced kinematics. In order to make explicit the assembly, we give an example. Considering a given node γ of the finite element mesh for which we suppose there are 6 DOFs, namely the 3 translations and the 3 rotations, and for which the numerotation in the finite element model is such that the 3 rotations come after the 3 translations, the intersection, with the 3 columns associated with the number-μ polynomial $p_{\boldsymbol{\alpha}^{(\mu)}}$, of the 6 rows in matrix $[B]$ that are associated with node γ, is the following sub-matrix,

$$[\,T_\gamma^\mu\,] = \begin{bmatrix} p_{\boldsymbol{\alpha}^{(\mu)}}(\mathbf{x}_\gamma) & 0 & 0 \\ 0 & p_{\boldsymbol{\alpha}^{(\mu)}}(\mathbf{x}_\gamma) & 0 \\ 0 & 0 & p_{\boldsymbol{\alpha}^{(\mu)}}(\mathbf{x}_\gamma) \\ 0 & 0 & 0 \\ 0 & 0 & 0 \\ 0 & 0 & 0 \end{bmatrix}. \tag{3.6}$$

As a consequence, for a three-dimensional dynamical system, the column dimension of matrix $[B]$ is $r = 3N_\mu$ (which is the dimension of subspace $\mathcal{S}_\mathcal{R}$, associated with the reduced kinematics).

The definition for the multivariate orthogonal polynomials $p_{\boldsymbol{\alpha}^{(\mu)}}$ is now given. For this, using the same notation as for $p_{\boldsymbol{\alpha}^{(\mu)}}$, the values, at the mesh nodes, of each of the associated multivariate monomials, $m_{\boldsymbol{\alpha}^{(\mu)}}$, can be written as

$$m_{\boldsymbol{\alpha}^{(\mu)}}(\mathbf{x}_\gamma) = \mathrm{x}_\gamma^{\alpha_1-\alpha_2}\,\mathrm{y}_\gamma^{\alpha_2-\alpha_3}\,\mathrm{z}_\gamma^{\alpha_3}\,. \tag{3.7}$$

Similarly to the definition of matrix $[\,p\,]$, let $[\,m\,]$ be the $(N_f \times N_\mu)$ real matrix that is constituted of the N_f values, at the mesh nodes, of each of the N_μ monomials $m_{\boldsymbol{\alpha}^{(\mu)}}$. Matrix $[\,m\,]$ of the discrete monomials being introduced, the explicit construction for $[\,p\,]$ is the following. Matrix $[\,p\,]$ is constructed as an orthonormalization of $[\,m\,]$, with respect to mass matrix $[\mathbb{M}]$. To do so, a QR decomposition

is performed.

Remark 1 For the case of the use of a diagonally-lumped approximation for mass matrix $[\mathbb{M}]$ (approximation for which we suppose the nodal mass is independent of the translational direction), the computation of matrix $[\,p\,]$ is carried out by performing the thin QR decomposition of the $(N_f \times N_\mu)$ real matrix $[\,a\,] = [m^\ell]^{1/2}[\,m\,]$, in which $[m^\ell]$ is the diagonal matrix constituted of the N_f nodal masses. The QR decomposition is written as

$$[\,a\,] = [\,q\,][\,r\,]\,, \tag{3.8}$$

in which $[\,r\,]$ is a $(N_\mu \times N_\mu)$ real matrix and where $[\,q\,]$ is a $(N_f \times N_\mu)$ real matrix, which verifies

$$[\,q\,]^T[\,q\,] = [I_{N_\mu}]\,. \tag{3.9}$$

Matrix $[\,p\,]$ can then be obtained by using $[\,p\,] = [m^\ell]^{-1/2}[\,q\,]$. Pre-multiplying latter equation by $[m^\ell]^{1/2}$ and using Eq. (3.9) yields the orthogonality property for the multivariate polynomials,

$$[\,p\,]^T[m^\ell][\,p\,] = [I_{N_\mu}]\,. \tag{3.10}$$

It should be noted that, in practice, the computation of $[\,p\,]$ is not necessary (which allows the inversion of diagonal matrix $[m^\ell]$ to be circumvented, useful if some diagonal terms in $[m^\ell]$ were to be zero). Instead, in order to construct the mass matrix corresponding to the polynomial approximation, which will be defined in next Section 3.1.2, only the product $[m^\ell]^{1/2}[\,q\,]$ is required.

Remark 2 The use of orthogonal polynomials allows for obtaining an orthonormalized basis matrix $[B]$, which verifies

$$[B]^T[\mathbb{M}][B] = [I_r]\,. \tag{3.11}$$

It should be noted that this step (the orthogonalization) is important with respect to the effectiveness of the method. In Section 3.1.2.1, the inversion of the reduced matrix in Eq. (3.11) is involved in the construction of a projector (orthogonal-projection matrix) that is used for the kinematics reduction of the mass matrix. Without the orthogonalization step, round-off errors would lead to an ill-conditioned reduced matrix (or even a rank-deficient one) and/or to large errors.

Deformation shapes via orthogonal projections onto polynomial bases In order to illustrate the effect of using such a polynomial approximation, which we recall to be devoted to the filtering of local displacements, we consider the orthogonal projection, onto the polynomial basis (represented by matrix $[B]$), of a regular low-frequency elastic mode of a car body structure. This elastic mode, depicted in Fig. 3.1, includes displacements of several structural scales, including (i) a global deformation of the body structure, (ii) a local deformation of the roof, and (iii) a highly local deformation of a flexible part that is located at the left back. The polynomial approximation is parameterized by the maximum degree d used for the polynomials. The filtering is thus controlled by the value of d. For different values of d, namely $d = 5$, $d = 10$, $d = 15$, and $d = 20$, the orthogonal projection of the low-frequency elastic mode is performed. The results are plotted in Figs. 3.2 to 3.5. It can be seen that, for the orthogonal projection given by $d = 5$, both scales of local displacements have been filtered. For the orthogonal projection given by $d = 15$, the first scale of local displacements, associated with the roof, is recovered. Finally, for the orthogonal projection given by $d = 20$, the original mode shape is recovered (including all the scales of displacements).

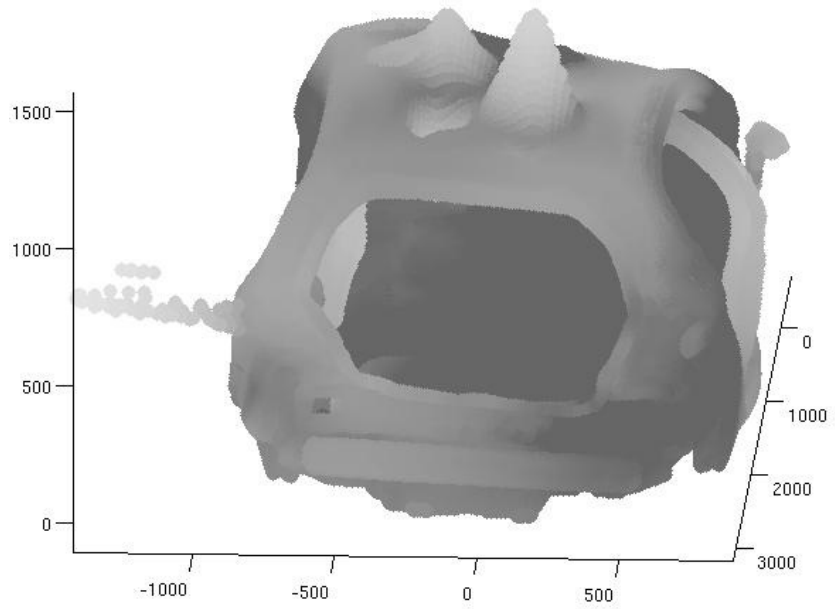

Figure 3.1: Mode shape of a regular low-frequency elastic mode of a car body structure (eigenfrequency 72 Hz).

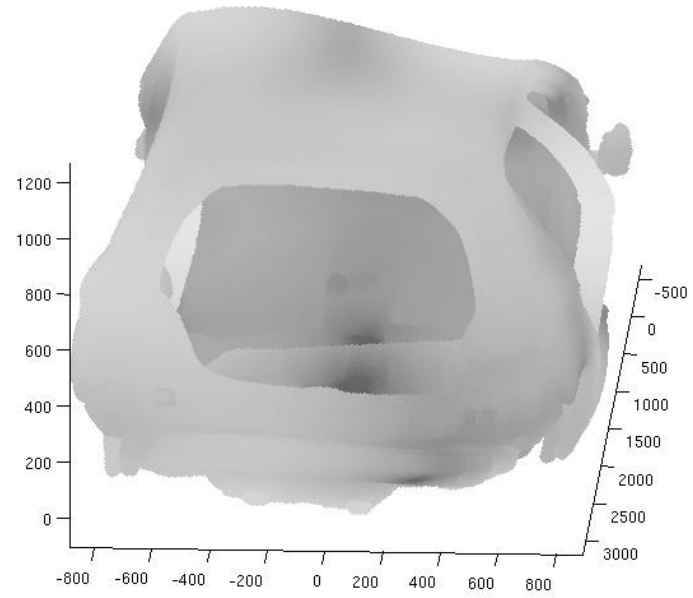

Figure 3.2: Deformation shape of the orthogonal projection, onto the polynomial basis of maximum degree $d = 5$, of the elastic mode shown in Fig. (3.1).

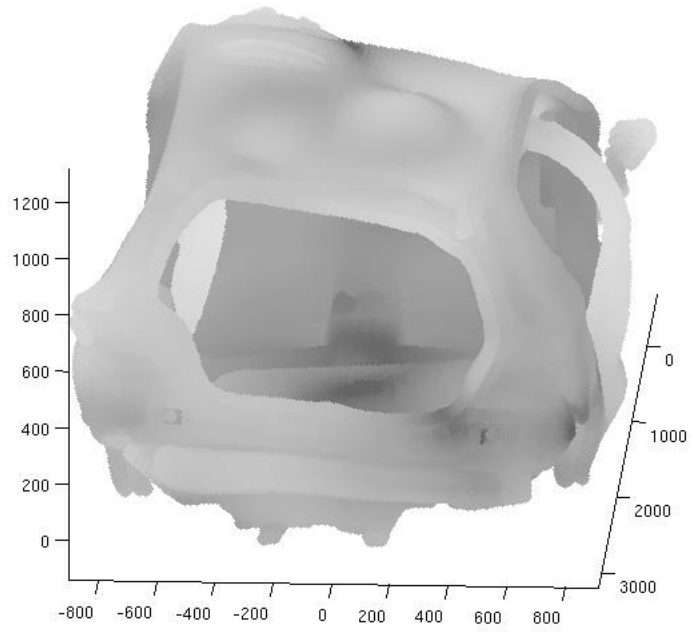

Figure 3.3: Deformation shape of the orthogonal projection, onto the polynomial basis of maximum degree $d = 10$, of the elastic mode shown in Fig. (3.1).

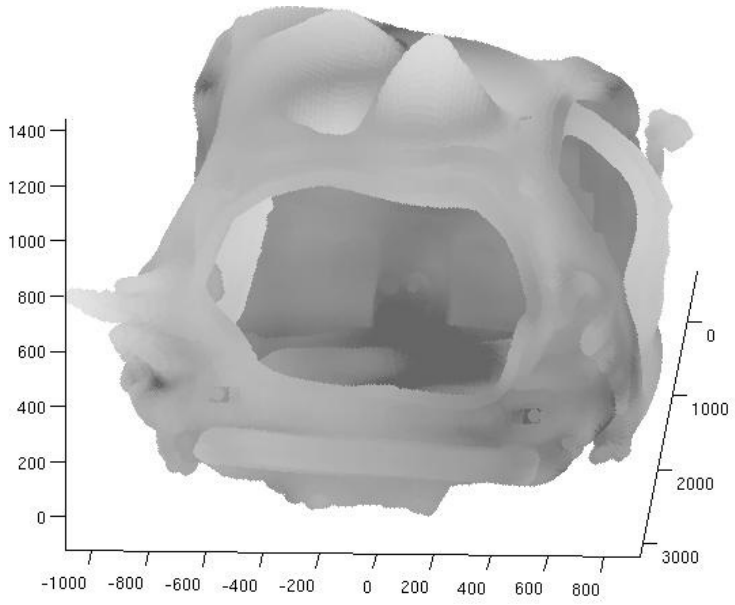

Figure 3.4: Deformation shape of the orthogonal projection, onto the polynomial basis of maximum degree $d = 15$, of the elastic mode shown in Fig. (3.1).

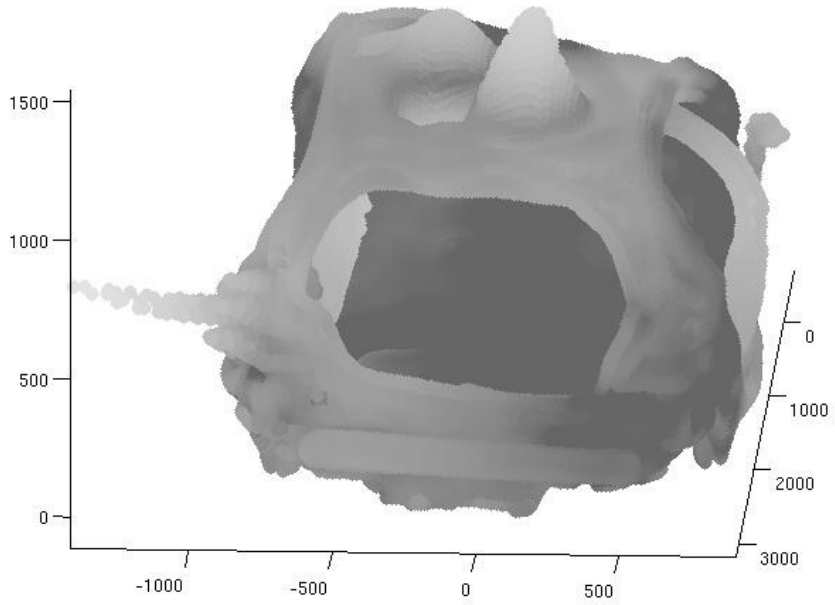

Figure 3.5: Deformation shape of the orthogonal projection, onto the polynomial basis of maximum degree $d = 20$, of the elastic mode shown in Fig. (3.1).

3.1.1.2 Alternative reduced kinematics

The proposed reduced kinematics, which is presently applied to whole domain Ω, can also be applied for each subdomain $\Omega_1, \ldots, \Omega_{N_s}$ of a partition of Ω. If such a partition is introduced, and if the maximum degree d of the polynomial approximation is chosen, for each subdomain, as $d = 0$ (which corresponds to a constant displacement field by subdomain), we then obtain the formulation introduced in [120]. In such a case, for the continuous formulation, a projection operator h^r of the displacement field $\mathbf{u}$ onto the subspace of constant functions by subdomain is, for all $\boldsymbol{x}$ in Ω, written as

$$\{h^r(\mathbf{u})\}(\boldsymbol{x}) = \sum_{j=1}^{N_s} \mathbb{1}_{\Omega_j}(\boldsymbol{x}) \frac{1}{m_j} \int_{\Omega_j} \rho(\boldsymbol{x}')\mathbf{u}(\boldsymbol{x}')d\boldsymbol{x}' \,, \tag{3.12}$$

in which $\mathbb{1}_{\Omega_j}(\boldsymbol{x}) = 1$ if $\boldsymbol{x} \in \Omega_j$ and is zero otherwise, where $m_j = \int_{\Omega_j} \rho(\boldsymbol{x})d\boldsymbol{x}$ is the mass of subdomain Ω_j, and where ρ is the mass density. In [120], the finite element discretization $[H^r]$ of h^r is used for obtaining the mass matrix associated with the reduced kinematics, $[\mathbb{M}^r] = [H^r]^T [\mathbb{M}] [H^r]$.

On the other hand, if the maximum degree d of the polynomial approximation is chosen, for each subdomain, as $d = 1$, then the reduced kinematics is very close to a rigid-body displacements field by subdomain as proposed in [128].

Figure 3.6 presents the case of a heterogeneous plate for which two distinct structural levels can be defined: the first one consists of a stiff skeleton and the second one of 12 flexible panels that are attached to the stiff skeleton. For this structure, numerous local displacements (associated with isolated vibrations of the flexible panels) are intertwined with the global displacements (associated with long-wavelength vibrations of the stiff skeleton). In order to filter the local displacements, a uniform domain partition of the structure is introduced. Two different approximations are used: a piecewise constant approximation and a piecewise linear approximation. For an elastic mode including both global and local displacements, both of these reduced kinematics allow the associated orthogonal projections to get rid of the local displacements of the flexible panels. In addition, for this case, it can be seen that, in comparison to the piecewise constant approximation, the piecewise linear approximation allows for obtaining a better approximation of the original deformation shape of the stiff skeleton, while the local displacements of the flexible panels remain filtered.

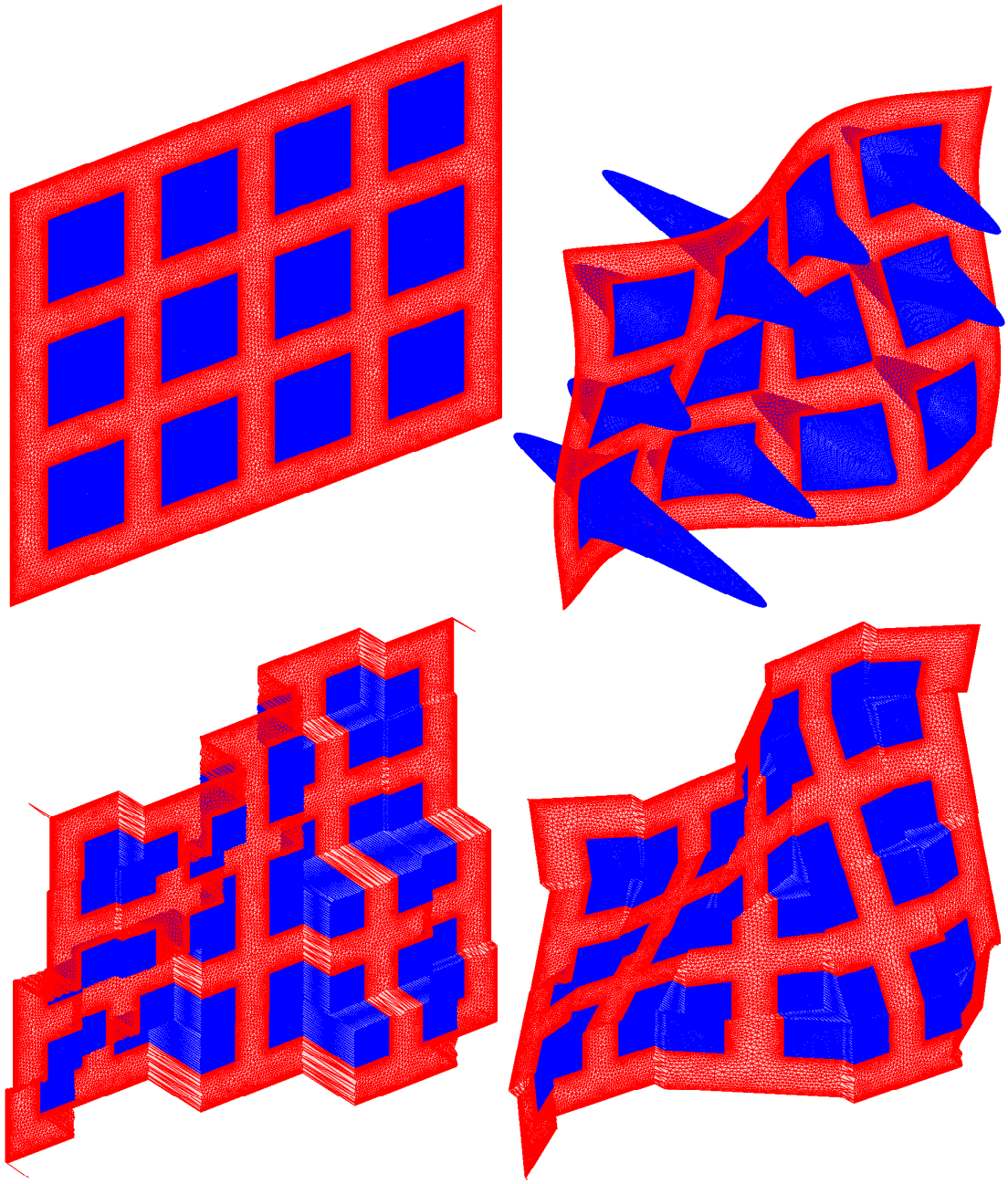

Figure 3.6: Case of a heterogeneous plate including two structural scales (with a stiff main frame supporting 12 flexible panels): undeformed configuration (top-left), an elastic mode exhibiting both global and local displacements (top-right), its orthogonal projection onto a subspace of piecewise constant functions (bottom-left), and its orthogonal projection onto a subspace of piecewise linear functions (bottom-right).

3.1.2 Reduced-kinematics mass matrix

It should be noted that in the case where both the kinetic and elastic energies were to be calculated using this polynomial approximation, the associated mass and stiffness matrices would be of reduced dimension $(r \times r)$ and given by $[B]^T[\mathbb{M}][B]$ and by $[B]^T[\mathbb{K}][B]$, respectively (which corresponds to a Galerkin projection, as used throughout all the document). In the present work, the strategy employed consists in approximating the kinetic energy while keeping the elastic energy exact. The construction of an unusual mass matrix, corresponding to the reduced kinematics, and which is compatible with keeping $[\mathbb{K}]$ as the stiffness matrix, is given. In the following, such an unusual mass matrix will be referenced as the *reduced-kinematics mass matrix*.

3.1.2.1 Definition

First, the kinetic energy $E_k(\mathbb{V}(t))$ associated with any time-dependent real velocity vector $\mathbb{V}(t)$ of dimension m is given by

$$E_k(\mathbb{V}(t)) = \frac{1}{2}\mathbb{V}(t)^T[\mathbb{M}]\mathbb{V}(t)\,. \tag{3.13}$$

Let then $\mathbb{V}^r(t)$ be the orthogonal projection of $\mathbb{V}(t)$ onto subspace $\mathcal{S}_\mathcal{R}$, with respect to the inner-product defined by matrix $[\mathbb{M}]$. It can be written as

$$\mathbb{V}^r(t) = [B]\,\mathbf{c}^{\text{opt}}(\mathbb{V}(t))\,, \tag{3.14}$$

in which $\mathbf{c}^{\text{opt}}(\mathbb{V}(t))$ is the unique solution of the optimization problem,

$$\mathbf{c}^{\text{opt}}(\mathbb{V}(t)) = \arg\min_{\mathbf{c}\,\in\,\mathbb{R}^r} \left(\mathbb{V}(t) - [B]\,\mathbf{c}\right)^T [\mathbb{M}]\,\left(\mathbb{V}(t) - [B]\,\mathbf{c}\right), \tag{3.15}$$

and which can be shown to be given by

$$\mathbf{c}^{\text{opt}}(\mathbb{V}(t)) = \left(\,[B]^T\,[\mathbb{M}]\,[B]\,\right)^{-1}\,[B]^T\,[\mathbb{M}]\,\mathbb{V}(t)\,. \tag{3.16}$$

Assuming the columns of $[B]$ to be orthonormalized with respect to $[\mathbb{M}]$ (see Eq. (3.11)), the projector $[\mathbb{P}]$ that is such that $\mathbb{V}^r(t) = [\mathbb{P}]\mathbb{V}(t)$ is therefore written as

$$[\mathbb{P}] = [B][B]^T[\mathbb{M}]\,, \tag{3.17}$$

the latter being a $(m \times m)$ real matrix of rank $r \leq m$. As a result, the reduced kinetic energy, defined as $E_k^r(\mathbb{V}(t)) = E_k(\mathbb{V}^r(t))$, can be written as

$$E_k^r(\mathbb{V}(t)) = \frac{1}{2}\mathbb{V}(t)^T[\mathbb{M}^r]\mathbb{V}(t)\,, \tag{3.18}$$

in which the m-dimensional reduced-kinematics mass matrix,

$$[\mathbb{M}^r] = [\mathbb{P}]^T[\mathbb{M}][\mathbb{P}]\,, \tag{3.19}$$

is of rank $r \leq m$, and can be written, using Eqs. (3.11), (3.17), and (3.19), as

$$[\mathbb{M}^r] = [\mathbb{M}][B][B]^T[\mathbb{M}]\,. \tag{3.20}$$

3.1.2.2 Positiveness and null space

Since matrix $[\mathbb{M}]$ is positive definite, from Eq. (3.19) it can be deduced that the null space of $[\mathbb{M}^r]$ is equal to the null space of $[\mathbb{P}]$. The null space of $[\mathbb{P}]$, which we denote as $\mathcal{S}_{\mathcal{R}}^{\perp}$, is the orthogonal complement of subspace $\mathcal{S}_{\mathcal{R}}$ of $\mathbb{R}^m$, with respect to the inner-product given by matrix $[\mathbb{M}]$. In other words, for all m-dimensional real vector $\mathbf{x}$, we have

$$\mathbf{x} = \mathbf{x}^r + \mathbf{x}^c, \tag{3.21}$$

in which vectors $\mathbf{x}^r = [\mathbb{P}]\,\mathbf{x} \in \mathcal{S}_{\mathcal{R}}$ and $\mathbf{x}^c = ([I_m] - [\mathbb{P}])\,\mathbf{x} \in \mathcal{S}_{\mathcal{R}}^{\perp}$ verify

$$\mathbf{x}^{c\,T}[\mathbb{M}]\,\mathbf{x}^r = 0\,. \tag{3.22}$$

The notion of orthogonal complement will be involved again later. Since dimension r of $\mathcal{S}_{\mathcal{R}}$ is such that $r \leq m$, matrix $[\mathbb{M}^r]$ is positive semidefinite.

3.1.2.3 Residual kinetic energy minimization

From Eqs. (3.13), (3.14), (3.15) and (3.22), it can be deduced that the construction proposed is such that the residual kinetic energy, $E_k(\mathbb{V}) - E_k(\mathbb{V}^r)$, verifying

$$E_k(\mathbb{V}) - E_k(\mathbb{V}^r) = E_k(\mathbb{V} - \mathbb{V}^r)\,, \tag{3.23}$$

is minimum.

3.1.2.4 Mass conservation

Let m^{tot} be the positive number such that $m^{\text{tot}} = \frac{1}{3}\,\mathbf{1}^T\,[\mathbb{M}]\,\mathbf{1}$, in which the m-dimensional vector $\mathbf{1}$ is constituted of ones for the translation DOFs and of zeros

for the rotation DOFs (if there exist in the computational model). Quantity m^{tot} represents approximately the mass of the structure (the mass located on the fixed boundary conditions is not taken into account). If $\mathbf{1}$ belongs to $\mathcal{S}_{\mathcal{R}}$ (in which case $[\mathbb{P}]\,\mathbf{1} = \mathbf{1}$), then the mass $m^{\text{tot},r} = \frac{1}{3}\,\mathbf{1}^T\,[\mathbb{M}^r]\,\mathbf{1}$ is such that $m^{\text{tot},r} = m^{\text{tot}}$. Since vector $\mathbf{1}$ is spanned by the 3 columns of matrix $[B]$ corresponding to polynomial $p_{\boldsymbol{\alpha}^{(1)}}$ (order-0 polynomial with multi-index $\boldsymbol{\alpha}^{(1)} = (0,0,0)$), it can be deduced that for any maximum degree d of the polynomial approximation, the mass is conserved within the kinematics reduction.

3.2 Global-displacements reduced-order basis

In order to span the global-displacements space, denoted by $\mathcal{S}_g$ (and which is a subspace of $\mathbb{R}^m$), mass matrix $[\mathbb{M}]$ is replaced by $[\mathbb{M}^r]$ for obtaining the generalized eigenvalue problem (that differs from the one used for computing the elastic modes and that cannot be used for computing them),

$$[\mathbb{K}]\boldsymbol{\psi}^g_\alpha = \sigma^g_\alpha[\mathbb{M}^r]\boldsymbol{\psi}^g_\alpha\,, \tag{3.24}$$

in which the eigenvectors $\boldsymbol{\psi}^g_\alpha$ consist of global displacements and where σ^g_α are the associated eigenvalues. The first r eigenvalues are such that $0 < \sigma^g_1 \leq \sigma^g_2 \leq \ldots \leq \sigma^g_r < +\infty$ and the eigenvalues of rank greater than r are all infinite, their associated eigenvectors being orthogonal to vector subspace $\mathcal{S}_{\mathcal{R}}$.

It should be noted that (i) the r eigenvectors $\boldsymbol{\psi}^g_\alpha$ are not orthogonal with respect to mass matrix $[\mathbb{M}]$ and (ii) they will be used for the projection of the computational model defined by Eq.(2.1), which involves mass matrix $[\mathbb{M}]$ and not $[\mathbb{M}^r]$. Let us introduce the $(m \times \nu)$ real matrix, $[\Psi^g] = [\boldsymbol{\psi}^g_1 \ldots \boldsymbol{\psi}^g_\nu]$, in which ν is a given truncation order such that

$$\nu \leq r\,. \tag{3.25}$$

The global-displacements ROB is then defined by the first eigenvectors of the dynamical system, which are constrained to belong to the vector space spanned by the ν columns of the $(m \times \nu)$ real matrix $[\Psi^g]$. The global-displacements ROB is denoted by $[\Phi^g]$ whose columns $\boldsymbol{\varphi}^g_\alpha$ are thus written as

$$\boldsymbol{\varphi}^g_\alpha = [\Psi^g]\mathbf{r}_\alpha\,, \tag{3.26}$$

in which $\mathbf{r}_\alpha$ are the eigenvectors of the small-dimension generalized eigenvalue

problem,

$$([\Psi^g]^T[\mathbb{K}][\Psi^g])\,\mathbf{r}_\alpha = \lambda^g_\alpha([\Psi^g]^T[\mathbb{M}][\Psi^g])\,\mathbf{r}_\alpha\,. \tag{3.27}$$

The eigenvalues verify $0 < \lambda^g_1 \leq \lambda^g_2 \leq \ldots \leq \lambda^g_\nu < +\infty$. Introducing the matrix $[R]$ such that $[R] = [\mathbf{r}_1 \ldots \mathbf{r}_{n_g}]$, in which n_g is a given truncation order that will be defined hereinafter, matrix $[\Phi^g]$ can be rewritten as

$$[\Phi^g] = [\Psi^g][R]\,, \tag{3.28}$$

which, using Eq. (3.27) and recalling our choice of a unit generalized mass normalization, yields

$$[\Phi^g]^T[\mathbb{K}][\Phi^g] = [\Lambda^g]\,, \qquad [\Phi^g]^T[\mathbb{M}][\Phi^g] = [I_{n_g}]\,, \tag{3.29}$$

with $[\Lambda^g]$ the diagonal matrix of the first n_g eigenvalues λ^g_α. Only the first n_g eigenvectors (associated with the lowest frequencies $f^g_\alpha = \sqrt{\lambda^g_\alpha}/2\pi$) are kept for constituting $[\Phi^g] = [\boldsymbol{\varphi}^g_1 \ldots \boldsymbol{\varphi}^g_{n_g}]$. Dimension n_g of global-displacements subspace $\mathcal{S}_g$ is deduced from a cutoff frequency, f^c, for which n_g verifies

$$f^g_{n_g} \leq f^c. \tag{3.30}$$

In addition, n_g satisfies the inequality,

$$n_g \leq \nu\,. \tag{3.31}$$

Cutoff frequency f^c is a data that must be chosen greater or equal to the upper bound $\omega_{\max}/2\pi$ of frequency band $\mathcal{B}$ and that must be adjusted through the analysis of the FRFs. It should be noted that truncation order ν cannot directly be deduced from the value $\sqrt{\sigma^g_\nu}/2\pi$ because the eigenvalues σ^g_α are not the eigenfrequencies of the dynamical system. For $\nu \leq r$, the following inequality can be shown,

$$\lambda^g_\nu \leq \sigma^g_\nu\,, \tag{3.32}$$

for which, in addition, the difference between λ^g_ν and σ^g_ν can be significant.

For brevity, no notation is introduced for the equations related to the global-displacements ROM, which would be similar to Eqs. (2.4) and (2.5) and which, anyway, would not be used.

3.3 Numerical implementation

As the mass matrix $[\mathbb{M}^r]$ is a full $(m \times m)$ matrix, this matrix is not assembled. In addition, the eigenvalue problem defined by Eq. (3.24) requires the knowledge of matrices $[\mathbb{M}]$ and $[\mathbb{K}]$, which can involve problems for the commercial software. The purpose of this section is to present an efficient method for the construction of the global-displacements ROB.

Let $[\mathbb{M}^\ell]$ be the diagonal matrix that is a lumped approximation of mass matrix $[\mathbb{M}]$. For avoiding the use of $[\mathbb{M}]$, the following approximation of $[\mathbb{M}^r]$ is introduced,

$$[\mathbb{M}^r] \simeq [\mathbb{M}^\ell][B^\ell][B^\ell]^T[\mathbb{M}^\ell]\,, \tag{3.33}$$

in which $[B^\ell]$ is constructed as $[B]$ (see Section 3.1) but is such that $[B^\ell]^T[\mathbb{M}^\ell][B^\ell] = [I_r]$. The projector $[\mathbb{P}]$ defined by Eq. (3.17) is then approximated by

$$[\mathbb{P}] \simeq [B^\ell][B^\ell]^T[\mathbb{M}^\ell]\,. \tag{3.34}$$

As the reduced kinematics is based on the use of polynomial shape functions defined over the whole domain, and as a lumped approximation of $[\mathbb{M}]$ can be obtained by using constant shape functions within each element of the finite element model, the error induced by the approximation defined by Eq. (3.33) can be considered negligible.

A double projection method is presented, which allows the knowledge of matrix $[\mathbb{K}]$ to be avoided. It consists in projecting Eq. (3.24) onto subspace $\mathcal{S}_c$ that is associated with the classical ROB made up of the elastic modes. Latter subspace is supposed to provide, upon the use of a sufficiently large value of the number n of elastic modes, an accurate representation within frequency band $\mathcal{B}$. Then, without loss of fidelity, such a projection can be obtained by writing

$$\mathcal{S}_g \subseteq \mathcal{S}_c \tag{3.35}$$

that is satisfied if $\boldsymbol{\psi}_\alpha^g$ is written as

$$\boldsymbol{\psi}_\alpha^g = [\Phi]\mathbf{s}_\alpha\,, \tag{3.36}$$

in which $\mathbf{s}_\alpha$ is a n-dimensional real vector that has to be calculated as follows. By using Eq. (3.36), the projection of Eq. (3.24) yields the following reduced-

dimension generalized eigenvalue problem,

$$([\Phi]^T[\mathbb{K}][\Phi])\,\mathbf{s}_\alpha = \sigma_\alpha^g([\Phi]^T[\mathbb{M}^r][\Phi])\,\mathbf{s}_\alpha\,. \tag{3.37}$$

The matrix $[\Phi]^T[\mathbb{K}][\Phi]$ is the diagonal matrix $[\Lambda]$ defined in Eq. (2.6), which is available. By using Eq. (3.33), the full matrix $[\Phi]^T[\mathbb{M}^r][\Phi]$ can be computed as

$$[\Phi]^T[\mathbb{M}^r][\Phi] \simeq [N][N]^T, \tag{3.38}$$

in which the $(n \times r)$ real matrix $[N]$ that is defined by

$$[N] = [\Phi]^T[\mathbb{M}^\ell][B^\ell] \tag{3.39}$$

is also available. Introducing $[S] = [\mathbf{s}_1 \dots \mathbf{s}_\nu]$ and using Eq. (3.36), matrix $[\Psi^g]$ can be written as

$$[\Psi^g] = [\Phi][S]\,. \tag{3.40}$$

Denoting as $[\Sigma^g]$ the diagonal matrix of the first ν eigenvalues σ_α^g and recalling our choice of a unit generalized mass normalization, it can then be deduced that the reduced matrices involved in Eq. (3.27) are such that

$$[\Psi^g]^T[\mathbb{K}][\Psi^g] = [\Sigma^g]\,, \qquad [\Psi^g]^T[\mathbb{M}][\Psi^g] = [S]^T[S]\,. \tag{3.41}$$

Remark 1. Physical interpretation of the filtering strategy Introducing the $(m \times n)$ real matrix $[\Phi^r] = [\mathbb{P}][\Phi]$, we obtain

$$[\Phi]^T[\mathbb{M}^r][\Phi] = [\Phi^r]^T[\mathbb{M}][\Phi^r]\,. \tag{3.42}$$

The following interpretation for Eq. (3.37) can be given. While reduced stiffness matrix $[\Phi]^T[\mathbb{K}][\Phi]$ is the projection of stiffness matrix $[\mathbb{K}]$ onto the basis $[\Phi]$ of the elastic modes (including both global and local displacements), the reduced mass matrix $[\Phi^r]^T[\mathbb{M}][\Phi^r]$ is the projection of mass matrix $[\mathbb{M}]$ onto displacements represented by matrix $[\Phi^r]$, which belong to subspace $\mathcal{S}_\mathcal{R}$, and in which some local displacements are filtered.

Remark 2. Computational efficiency It should be noted that the numerical rank, R, of $[N][N]^T$ is such that $R \leq r$ and $R \leq n$, and that, similarly to Eq. (3.25), truncation order ν must satisfy the inequality $\nu \leq R$. For computing the generalized eigenvalue problem given by Eq. (3.37), three cases are considered.

- For $r < n$, a thin SVD (see [137]) of the $(n \times r)$ real matrix $[\Lambda]^{-1/2}[N]$ is

performed for a lower cost.

- For $r \gg n$, $R = n$ is verified and matrix $[N][N]^T$ is positive definite. For this case, the usual algorithms are used.

- For the intermediate case for which R is close to n, in order to obtain a good accuracy, the SVD approach is more efficient.

3.4 Local-displacements reduced-order basis

In the rest of the document, it is assumed that the above numerical implementation of the global-displacements ROB explicited in Section 3.3 is used. In this section, we present the construction of a local-displacements ROB. The vector subspace associated with the local-displacements ROB, denoted by $\mathcal{S}_\ell$, is the orthogonal complement of subspace $\mathcal{S}_g$ of $\mathcal{S}_c$, with respect to the inner-product defined by matrix $[\mathbb{M}]$. In particular, $\mathcal{S}_c$ is the orthogonal direct sum of $\mathcal{S}_g$ with $\mathcal{S}_\ell$, and we write

$$\mathcal{S}_c = \mathcal{S}_g \oplus \mathcal{S}_\ell \,. \tag{3.43}$$

Thanks to this definition of $\mathcal{S}_\ell$, its ROB, denoted by $[\Phi^\ell]$, satisfies the orthogonality condition,

$$[\Phi^g]^T [\mathbb{M}][\Phi^\ell] = [0], \tag{3.44}$$

as well as the equality

$$[\Phi^\ell] = [\Phi][Q^\ell], \tag{3.45}$$

in which $[Q^\ell]$ is the $(n \times n_\ell)$ real matrix of the coordinates in the basis defined by $[\Phi]$, and where the dimension n_ℓ is such that

$$n_\ell = n - n_g \,. \tag{3.46}$$

Let $[Q^g]$ be the $(n \times n_g)$ real matrix such that

$$[Q^g] = [S][R] \,. \tag{3.47}$$

Using Eqs. (3.28), (3.40), and (3.47) yields

$$[\Phi^g] = [\Phi][Q^g] \,. \tag{3.48}$$

From Eqs. (2.3), (3.44), (3.45), and (3.48), the following orthogonality property can be deduced,

$$[Q^g]^T[Q^\ell] = [0]\,. \tag{3.49}$$

Let $[Z]$ be the $(n \times n_\ell)$ real matrix whose columns are the right-singular vectors associated with the n_ℓ zero singular values of the SVD of $[Q^g]^T$ (and which, consequently, constitute an algebraic basis of the null space of $[Q^g]^T$). By construction, matrix $[Z]$ verifies

$$[Z]^T[Z] = [I_{n_\ell}]\,. \tag{3.50}$$

Equation (3.49) is satisfied for $[Q^\ell]$ expressed as

$$[Q^\ell] = [Z][U]\,, \tag{3.51}$$

in which $[U]$ is a $(n_\ell \times n_\ell)$ real matrix of coordinates in the basis defined by $[Z]$. The local-displacements ROB represented by matrix $[\Phi^\ell]$ is then defined by the first eigenvectors of the dynamical system, which are constrained to belong to the vector space spanned by the n_ℓ columns of the $(m \times n_\ell)$ real matrix $[\Phi][Z]$. The columns $\boldsymbol{\varphi}^\ell_\alpha$ of $[\Phi^\ell]$ are thus written as

$$\boldsymbol{\varphi}^\ell_\alpha = [\Phi][Z]\mathbf{u}_\alpha\,, \tag{3.52}$$

in which, thanks to Eqs.(2.6) and (3.50), it can be deduced that the columns $\mathbf{u}_\alpha$ of $[U]$ are the eigenvectors of the following standard eigenvalue problem of reduced dimension,

$$([Z]^T[\Lambda][Z])\mathbf{u}_\alpha = \lambda^\ell_\alpha\,\mathbf{u}_\alpha\,, \tag{3.53}$$

in which the associated eigenvalues λ^ℓ_α verify $0 < \lambda^\ell_1 \leq \lambda^\ell_2 \leq \ldots \leq \lambda^\ell_{n_\ell} < +\infty$. In this Chapter 3, a general method has been presented for obtaining a global-displacements ROM, for which the construction of the associated ROB depends on the choice of parameters d (maximum degree of the polynomial approximation), ν (truncation order), and f^c (cutoff frequency). The dimension n_g of the ROM results from the values of these parameters. Suitable values of d and ν must be tuned in order to obtain a smaller dimension $n_g \leq n$ while preserving the fidelity of the computational model. As higher frequencies are characterized by vibrations of shorter wavelength, the choice of the values for d and ν strongly depend on the value of frequency f^c. The construction of a ROB made up of local displacements, which is complementary to the global-displacements ROB, has also been proposed,

and will be useful for the construction of a multilevel ROM.

Chapter 4

Multilevel reduced-order model

4.1 Formulation of the multilevel reduced-order model

In this section, the previous developments are used in the construction of a multilevel ROM, for which three ROBs associated with the low-, medium-, and high-frequency bands (LF, MF, HF) are introduced. In contrast to the HF band, the LF band is associated with long-wavelength global displacements, while the MF band is a combination of global and local displacements with more or less short wavelength. For the complex structures considered, there is an overlap of the three vibration regimes. For instance, numerous local elastic modes can be found in low frequencies. The previously introduced filtering strategy is therefore used in order to separate the LF-, MF-, and HF-type displacements. The filtering methodology presented in Sections 3.3 and 3.4 can be condensed into the following mapping,

$$\mathcal{F}_1 : (\mathcal{S}_c \, ; d, \nu, f^c) \longmapsto (\mathcal{S}_g \, , \mathcal{S}_\ell) \, , \tag{4.1}$$

which will be used for defining the multilevel ROM. Like the classical ROM, the multilevel ROM is devoted to the vibration analysis over whole band $\mathcal{B}$, which can be decomposed into three bands, such that

$$\mathcal{B} = \mathcal{B}_\mathcal{L} \cup \mathcal{B}_\mathcal{M} \cup \mathcal{B}_\mathcal{H} \, . \tag{4.2}$$

We now present the basic ideas concerning the construction of the multilevel ROM, based on the introduction of three successive filterings, which are defined through mapping $\mathcal{F}_1$.

Introducing the cutoff frequency, $f_{\mathcal{H}}^c$, associated with the upper bound of $\mathcal{B}_{\mathcal{H}}$, the (global-displacements) vector subspace, $\mathcal{S}_t$, which includes the totality of the remaining considered displacements and which is associated with the multilevel ROM, is given by

$$(\mathcal{S}_t\,,\mathcal{S}_t^{\perp}) = \mathcal{F}_1(\mathcal{S}_c\,;d_{\mathcal{H}},\nu_{\mathcal{H}},f_{\mathcal{H}}^c)\,, \tag{4.3}$$

in which the values of the parameters $d_{\mathcal{H}}$ and $\nu_{\mathcal{H}}$ are tuned in order to obtain a decreased dimension while preserving the fidelity of the ROM up to frequency $f_{\mathcal{H}}^c$. It should be recalled that subspace $\mathcal{S}_c$ is assumed to be associated with an accurate classical ROM over band $\mathcal{B}$. The (local-displacements) vector subspace $\mathcal{S}_t^{\perp}$, verifying $\mathcal{S}_c = \mathcal{S}_t \oplus \mathcal{S}_t^{\perp}$, is not used (the local displacements spanning this subspace are discarded in order to decrease the dimension of the proposed ROM). For carrying out the next filterings, similarly to the double projection method associated with Eq. (3.35), the computational model is now projected onto subspace $\mathcal{S}_t$, which is supposed to be associated with a sufficiently accurate representation.

Similarly, introducing the cutoff frequency, $f_{\mathcal{M}}^c$, associated with the upper bound of $\mathcal{B}_{\mathcal{M}}$, the (local-displacements) vector subspace, $\mathcal{S}_{\mathcal{H}}$, associated with the HF vibration regime, is given by

$$(\mathcal{S}_{\mathcal{LM}}\,,\mathcal{S}_{\mathcal{H}}) = \mathcal{F}_1(\mathcal{S}_t\,;d_{\mathcal{M}},\nu_{\mathcal{M}},f_{\mathcal{M}}^c)\,, \tag{4.4}$$

where $\mathcal{S}_{\mathcal{LM}}$ is the complementary (global-displacements) subspace belonging to $\mathcal{S}_t$. The values of the parameters $d_{\mathcal{M}}$ and $\nu_{\mathcal{M}}$ are tuned such that the ROB associated with $\mathcal{S}_{\mathcal{LM}}$ yields an adequate representation up to frequency $f_{\mathcal{M}}^c$. We have the decomposition,

$$\mathcal{S}_t = \mathcal{S}_{\mathcal{LM}} \oplus \mathcal{S}_{\mathcal{H}}\,. \tag{4.5}$$

Finally, introducing the cutoff frequency, $f_{\mathcal{L}}^c$, associated with the upper bound of $\mathcal{B}_{\mathcal{L}}$, the (global-displacements) vector subspace, $\mathcal{S}_{\mathcal{L}}$, associated with the LF vibration regime, is given by

$$(\mathcal{S}_{\mathcal{L}}\,,\mathcal{S}_{\mathcal{M}}) = \mathcal{F}_1(\mathcal{S}_{\mathcal{LM}}\,;d_{\mathcal{L}},\nu_{\mathcal{L}},f_{\mathcal{L}}^c)\,, \tag{4.6}$$

where $\mathcal{S}_{\mathcal{M}}$ is the complementary (local-displacements) subspace belonging to $\mathcal{S}_{\mathcal{LM}}$. The values of the parameters $d_{\mathcal{L}}$ and $\nu_{\mathcal{L}}$ are tuned such that the ROB associated with $\mathcal{S}_{\mathcal{L}}$, expected to mainly consist of global displacements, yields an adequate representation up to frequency $f_{\mathcal{L}}^c$. It should be noted that, similarly to before, the proposed construction makes the assumption that subspace $\mathcal{S}_{\mathcal{LM}}$, which is as-

sociated with a higher polynomial degree having been tuned for covering a wider frequency band (LF ∪ MF), is associated with a sufficiently accurate representation (for the LF band). Finally, we have the decomposition,

$$\mathcal{S}_{\mathcal{LM}} = \mathcal{S}_{\mathcal{L}} \oplus \mathcal{S}_{\mathcal{M}} \,, \tag{4.7}$$

and consequently, using Eqs. (4.5) and (4.7), we obtain

$$\mathcal{S}_t = \mathcal{S}_{\mathcal{L}} \oplus \mathcal{S}_{\mathcal{M}} \oplus \mathcal{S}_{\mathcal{H}} \,. \tag{4.8}$$

4.2 Implementation of the multilevel nominal reduced-order model

4.2.1 Numerical procedure

In this section, no new concept is introduced, but only details useful for the numerical implementation. The steps seen in Sections 3.3 and 3.4, devoted to the construction of the global-displacements ROB and of the local-displacements ROB, are summarized. Similarly to Eq. (4.1), the procedure is then compacted in a mapping, $\mathcal{F}_2$, which allows for defining the algebraic quantities associated with the multilevel ROM formulated in Section 4.1. In the following, the steps for calculating the outputs of mapping $\mathcal{F}_2$ are given.

For this, it is assumed that maximum degree d of the polynomial approximation, truncation order ν, and cutoff frequency f^c are given and in addition, some new notations are now introduced in order to generalize the numerical procedure. Let $[\Lambda^0]$ be a diagonal matrix of dimension n_0 whose diagonal elements are strictly positive. Let $[Q^0]$ be a $(n_1 \times n_0)$ real matrix for which $n_1 \geq n_0$ and such that $[Q^0]^T[Q^0] = [I_{n_0}]$. Let $[N^0]$ be a $(n_1 \times r_{\max})$ real matrix for which $r_{\max} \geq r$, with

$$r = (d+1)(d+2)(d+3)/2 \,. \tag{4.9}$$

These three matrices are the input parameters of mapping $\mathcal{F}_2$ in addition to the filtering parameters, d, ν, and f^c. The outputs of mapping $\mathcal{F}_2$ will allow us to define the construction of all the matrices involved in the multilevel ROM. It should be noted that, aside from the multilevel ROM, mapping $\mathcal{F}_2$ allows for constructing the global- and the local-displacements ROBs defined in Section 3 by using, as inputs: $[\Lambda^0] = [\Lambda]$, $[Q^0] = [I_n]$ with $n_1 = n_0 = n$, and $[N^0] = [N]$.

The matrix $[N^0]$ is associated with a reduced kinematics for which the maximum

degree of the polynomials is greater or equal to d, and which may already have been used during a previous filtering. Let $[N_r^0]$ be the $(n_1 \times r)$ matrix constituted of the first r columns of $[N^0]$. In addition, the latter possible previous filtering is associated with a change of basis defined by matrix $[Q^0]$. Let $[N_r]$ be the $(n_0 \times r)$ real matrix defined by

$$[N_r] = [Q^0]^T [N_r^0] \,. \tag{4.10}$$

The eigenvectors $\mathbf{s}_\alpha$ and associated eigenvalues σ_α^g are calculated, similarly to Eq. (3.37), as

$$[\Lambda^0]\, \mathbf{s}_\alpha = \sigma_\alpha^g ([N_r][N_r]^T)\, \mathbf{s}_\alpha \,. \tag{4.11}$$

Using $[S] = [\mathbf{s}_1 \dots \mathbf{s}_\nu]$ and $[\Sigma^g]$ the matrix of the eigenvalues σ_α^g, eigenvectors $\mathbf{r}_\alpha$ and associated eigenvalues λ_α^g are calculated, similarly to Eq. (3.27), as

$$[\Sigma^g]\, \mathbf{r}_\alpha = \lambda_\alpha^g ([S]^T [S]) \mathbf{r}_\alpha \,. \tag{4.12}$$

Dimension n_g of the global-displacements ROB is the maximum integer α verifying $f_\alpha^g \leq f^c$, with $f_\alpha^g = \sqrt{\lambda_\alpha^g}/2\pi$. Then, matrix $[\Lambda^g]$ is made up of the first n_g eigenvalues λ_α^g. In addition, matrix $[R] = [\mathbf{r}_1 \dots \mathbf{r}_{n_g}]$ is obtained, from which matrix $[Q^g] = [S][R]$ is constructed. Introducing $[C] = [Q^g]^T$, the following SVD is performed,

$$[C] = [U_C][\Sigma_C][V_C]^T, \tag{4.13}$$

from which the columns of $[V_C]$ associated with the n_ℓ zero singular values in $[\Sigma_C]$ allow for obtaining the $(n_0 \times n_\ell)$ real matrix $[Z]$ with $n_\ell = n_0 - n_g$. Finally, the eigenvectors $\mathbf{u}_\alpha$ and the associated eigenvalues λ_α^ℓ are calculated, similarly to Eq. (3.53), as

$$([Z]^T [\Lambda^0][Z]) \mathbf{u}_\alpha = \lambda_\alpha^\ell \, \mathbf{u}_\alpha \,, \tag{4.14}$$

which allows for obtaining the matrix $[U] = [\mathbf{u}_1 \dots \mathbf{u}_{n_\ell}]$ and the diagonal matrix $[\Lambda^\ell]$ of the n_ℓ eigenvalues λ_α^ℓ, followed by the construction of matrix $[Q^\ell] = [Z][U]$.

The procedure just summarized allows the following mapping to be constructed,

$$([\Lambda^g], [Q^g], [N_r], [\Lambda^\ell], [Q^\ell]) = \mathcal{F}_2([\Lambda^0], [Q^0], [N^0]; d, \nu, f^c) \,, \tag{4.15}$$

whose outputs $[Q^g]$ and $[Q^\ell]$ can be shown, using Eqs. (3.27), (3.41), (3.45), (3.49), (3.50), (3.51), and (3.53), and recalling our choice of a unit generalized mass

normalization, to verify the following orthonormality properties,

$$[Q^g]^T[Q^g] = [I_{n_g}], \qquad [Q^\ell]^T[Q^\ell] = [I_{n_\ell}], \qquad [Q^g]^T[Q^\ell] = [0]\,. \tag{4.16}$$

4.2.2 Construction of the reduced-order bases

4.2.2.1 First filtering

In Eq. (4.3), vector subspace $\mathcal{S}_t$ is obtained by the projection onto $\mathcal{S}_c$ in which $d_{\mathcal{H}}$, $\nu_{\mathcal{H}}$, and $f^c_{\mathcal{H}}$ are the filtering parameters. Denoting by n_t the dimension of the multilevel ROM and setting $r_{\mathcal{H}} = (d_{\mathcal{H}} + 1)(d_{\mathcal{H}} + 2)(d_{\mathcal{H}} + 3)/2$, we define the real matrices $[\Lambda^t]$, $[Q^t]$, and $[N^t]$, respectively of dimensions $(n_t \times n_t)$, $(n \times n_t)$, and $(n \times r_{\mathcal{H}})$, as the first three outputs of mapping $\mathcal{F}_2$, such that

$$([\Lambda^t], [Q^t], [N^t], \sim, \sim) = \mathcal{F}_2([\Lambda], [I_n], [N]; d_{\mathcal{H}}, \nu_{\mathcal{H}}, f^c_{\mathcal{H}})\,, \tag{4.17}$$

in which $[N] = [\Phi]^T[\mathbb{M}^\ell][B^\ell]$. The symbol $\sim$ indicates that the corresponding output variables are not calculated. The ROB $[\Phi^t]$ associated with $\mathcal{S}_t$ is given by

$$[\Phi^t] = [\Phi][Q^t]\,, \tag{4.18}$$

in which, thanks to Eq. (4.16), $[Q^t]$ verifies

$$[Q^t]^T[Q^t] = [I_{n_t}]\,. \tag{4.19}$$

4.2.2.2 Second filtering

In Eq. (4.4), vector subspaces $\mathcal{S}_{\mathcal{LM}}$ and $\mathcal{S}_{\mathcal{H}}$ have their ROB defined through the following outputs of mapping $\mathcal{F}_2$,

$$([\Lambda^{\mathcal{LM}}], [Q^{\mathcal{LM}}], [N^{\mathcal{LM}}], [\Lambda^{\mathcal{H}}], [Q^{\mathcal{H}}]) = \mathcal{F}_2([\Lambda^t], [Q^t], [N^t]; d_{\mathcal{M}}, \nu_{\mathcal{M}}, f^c_{\mathcal{M}})\,, \tag{4.20}$$

in which $\nu_{\mathcal{M}} \leq n_t$ and where, similarly to Eq. (4.16), the following properties are verified,

$$[Q^{\mathcal{LM}}]^T[Q^{\mathcal{LM}}] = [I_{n_{\mathcal{LM}}}], \qquad [Q^{\mathcal{H}}]^T[Q^{\mathcal{H}}] = [I_{n_{\mathcal{H}}}], \qquad [Q^{\mathcal{LM}}]^T[Q^{\mathcal{H}}] = [0]\,, \tag{4.21}$$

in which $n_{\mathcal{LM}} = \dim(\mathcal{S}_{\mathcal{LM}})$ and $n_{\mathcal{H}} = \dim(\mathcal{S}_{\mathcal{H}})$. The ROBs $[\Phi^{\mathcal{LM}}]$ and $[\Phi^{\mathcal{H}}]$ of subspaces $\mathcal{S}_{\mathcal{LM}}$ and $\mathcal{S}_{\mathcal{H}}$ are given by

$$[\Phi^{\mathcal{LM}}] = [\Phi^t][Q^{\mathcal{LM}}]\,, \qquad [\Phi^{\mathcal{H}}] = [\Phi^t][Q^{\mathcal{H}}]\,. \tag{4.22}$$

4.2.2.3 Third filtering

In Eq. (4.6), vector subspaces $\mathcal{S}_{\mathcal{L}}$ and $\mathcal{S}_{\mathcal{M}}$ have their ROB defined through the following outputs of mapping $\mathcal{F}_2$,

$$([\Lambda^{\mathcal{L}}],[Q^{\mathcal{L}}],\sim,[\Lambda^{\mathcal{M}}],[Q^{\mathcal{M}}]) = \mathcal{F}_2([\Lambda^{\mathcal{L}\mathcal{M}}],[Q^{\mathcal{L}\mathcal{M}}],[N^{\mathcal{L}\mathcal{M}}];d_{\mathcal{L}},\nu_{\mathcal{L}},f^c_{\mathcal{L}})\,, \tag{4.23}$$

in which $\nu_{\mathcal{L}} \leq n_{\mathcal{L}\mathcal{M}}$ and where, similarly to Eq. (4.16), the following properties are verified,

$$[Q^{\mathcal{L}}]^T[Q^{\mathcal{L}}] = [I_{n_{\mathcal{L}}}], \qquad [Q^{\mathcal{M}}]^T[Q^{\mathcal{M}}] = [I_{n_{\mathcal{M}}}], \qquad [Q^{\mathcal{L}}]^T[Q^{\mathcal{M}}] = [0]\,, \tag{4.24}$$

in which $n_{\mathcal{L}} = \dim(\mathcal{S}_{\mathcal{L}})$ and $n_{\mathcal{M}} = \dim(\mathcal{S}_{\mathcal{M}})$. The ROBs $[\Phi^{\mathcal{L}}]$ and $[\Phi^{\mathcal{M}}]$ of respectively subspaces $\mathcal{S}_{\mathcal{L}}$ and $\mathcal{S}_{\mathcal{M}}$ are given by $[\Phi^{\mathcal{L}}] = [\Phi^{\mathcal{L}\mathcal{M}}][Q^{\mathcal{L}}]$ and $[\Phi^{\mathcal{M}}] = [\Phi^{\mathcal{L}\mathcal{M}}][Q^{\mathcal{M}}]$, which yields

$$[\Phi^{\mathcal{L}}] = [\Phi^t][Q^{\mathcal{L}\mathcal{M}}][Q^{\mathcal{L}}]\,, \qquad [\Phi^{\mathcal{M}}] = [\Phi^t][Q^{\mathcal{L}\mathcal{M}}][Q^{\mathcal{M}}]\,. \tag{4.25}$$

4.2.3 Construction of the reduced-order models

4.2.3.1 Scale-$\mathcal{S}$ reduced-order model

For $\mathcal{S} = t$, $\mathcal{S} = \mathcal{L}\mathcal{M}$, $\mathcal{S} = \mathcal{H}$, $\mathcal{S} = \mathcal{L}$, or $\mathcal{S} = \mathcal{M}$, when using the scale-$\mathcal{S}$ ROM, displacements $\mathbb{U}(\omega)$ belong to the subspace $\mathcal{S}_{\mathcal{S}}$ that is defined as the space spanned by the columns of matrix $[\Phi^{\mathcal{S}}]$. That is, they are approximated as

$$\mathbb{U}(\omega) \simeq [\Phi^{\mathcal{S}}]\mathbf{q}^{\mathcal{S}}(\omega)\,, \tag{4.26}$$

where the $n_{\mathcal{S}}$-dimensional complex vector of generalized coordinates $\mathbf{q}^{\mathcal{S}}(\omega)$ is the solution of the reduced-matrix equation,

$$(\,-\omega^2[\mathcal{M}^{\mathcal{S}}] + i\omega[\mathcal{D}^{\mathcal{S}}] + [\mathcal{K}^{\mathcal{S}}]\,)\,\mathbf{q}^{\mathcal{S}}(\omega) = \mathbf{f}^{\mathcal{S}}(\omega)\,. \tag{4.27}$$

In latter equation, thanks to the choice of a unit generalized mass normalization and to Eqs. (2.3), (3.29), (4.18), (4.21), (4.22), (4.24), and (4.25), we have

$$\mathbf{f}^{\mathcal{S}}(\omega) = [\Phi^{\mathcal{S}}]^T\mathbb{F}(\omega)\,, \quad [\mathcal{M}^{\mathcal{S}}] = [\Phi^{\mathcal{S}}]^T[\mathbb{M}][\Phi^{\mathcal{S}}] = [I_{n_{\mathcal{S}}}]\,,$$
$$[\mathcal{D}^{\mathcal{S}}] = [\Phi^{\mathcal{S}}]^T[\mathbb{D}][\Phi^{\mathcal{S}}]\,, \quad [\mathcal{K}^{\mathcal{S}}] = [\Phi^{\mathcal{S}}]^T[\mathbb{K}][\Phi^{\mathcal{S}}] = [\Lambda^{\mathcal{S}}]\,. \tag{4.28}$$

4.2.3.2 Multilevel nominal reduced-order model

Introducing the $(m \times n_t)$ ROB, $[\Psi]$, of the multilevel nominal ROM (ML-NROM), which is given by

$$[\Psi] = [\,[\Phi^{\mathcal{L}}][\Phi^{\mathcal{M}}][\Phi^{\mathcal{H}}]\,]\,, \tag{4.29}$$

displacements $\mathbb{U}(\omega)$ are approximated, using the ML-NROM, as

$$\mathbb{U}(\omega) \simeq [\Psi]\mathbf{q}(\omega) = [\Phi^{\mathcal{L}}]\mathbf{q}^{\mathcal{L}}(\omega) + [\Phi^{\mathcal{M}}]\mathbf{q}^{\mathcal{M}}(\omega) + [\Phi^{\mathcal{H}}]\mathbf{q}^{\mathcal{H}}(\omega)\,, \tag{4.30}$$

in which $\mathbf{q}(\omega) = (\mathbf{q}^{\mathcal{L}}(\omega), \mathbf{q}^{\mathcal{M}}(\omega), \mathbf{q}^{\mathcal{H}}(\omega))$ with $\mathbf{q}^{\mathcal{L}}(\omega)$ in $\mathbb{C}^{n_{\mathcal{L}}}$, $\mathbf{q}^{\mathcal{M}}(\omega)$ in $\mathbb{C}^{n_{\mathcal{M}}}$, and $\mathbf{q}^{\mathcal{H}}(\omega)$ in $\mathbb{C}^{n_{\mathcal{H}}}$. Complex vector $\mathbf{q}(\omega)$ is the solution of the reduced-matrix equation,

$$(\,-\omega^2[M] + i\omega[D] + [K]\,)\,\mathbf{q}(\omega) = \mathbf{f}(\omega)\,, \tag{4.31}$$

in which

$$\mathbf{f}(\omega) = [\Psi]^T\mathbb{F}(\omega)\,, \qquad [M] = [\Psi]^T[\mathbb{M}][\Psi]\,, \qquad [D] = [\Psi]^T[\mathbb{D}][\Psi]\,, \qquad [K] = [\Psi]^T[\mathbb{K}][\Psi]\,. \tag{4.32}$$

Introducing $[W^{\mathcal{L}}] = [Q^{\mathcal{L}\mathcal{M}}][Q^{\mathcal{L}}]$, $[W^{\mathcal{M}}] = [Q^{\mathcal{L}\mathcal{M}}][Q^{\mathcal{M}}]$, and $[W^{\mathcal{H}}] = [Q^{\mathcal{H}}]$, from Eqs. (4.22), (4.25), and (4.29), it can be deduced that a block-writing of reduced matrix $[A] = [\Psi]^T[\mathbb{A}][\Psi]$ — for $([A],[\mathbb{A}]) \in \{([M],[\mathbb{M}]),([D],[\mathbb{D}]),([K],[\mathbb{K}])\}$ — can be written as

$$[A] = \begin{bmatrix} [\,A^{\mathcal{L}\mathcal{L}}\,] & [\,A^{\mathcal{L}\mathcal{M}}\,] & [\,A^{\mathcal{L}\mathcal{H}}\,] \\ [A^{\mathcal{M}\mathcal{L}}] & [A^{\mathcal{M}\mathcal{M}}] & [A^{\mathcal{M}\mathcal{H}}] \\ [\,A^{\mathcal{H}\mathcal{L}}\,] & [\,A^{\mathcal{H}\mathcal{M}}\,] & [\,A^{\mathcal{H}\mathcal{H}}\,] \end{bmatrix}\,, \tag{4.33}$$

for which the matrix blocks are defined as follows. For $\mathcal{I}$ and $\mathcal{J}$ in $\{\mathcal{L},\mathcal{M},\mathcal{H}\}$, the $(n_{\mathcal{I}} \times n_{\mathcal{J}})$ real matrix $[A^{\mathcal{I}\mathcal{J}}]$ is given by

$$[A^{\mathcal{I}\mathcal{J}}] = [W^{\mathcal{I}}]^T[\mathcal{A}^t][W^{\mathcal{J}}]\,, \tag{4.34}$$

where, using Eq. (4.18), we have $[\mathcal{A}^t] = [Q^t]^T[\mathcal{A}][Q^t]$ with $[\mathcal{A}] = [\Phi]^T[\mathbb{A}][\Phi]$. Moreover, Eqs. (4.19), (4.21), and (4.24) yield

$$[W^{\mathcal{I}}]^T[W^{\mathcal{I}}] = [I_{n_{\mathcal{I}}}]\,, \qquad [W^{\mathcal{I}}]^T[W^{\mathcal{J}}] = [0] \text{ if } \mathcal{I} \neq \mathcal{J}\,, \tag{4.35}$$

from which it can be deduced that $[M] = [I_{n_t}]$.

4.3 Multilevel stochastic reduced-order model

Similarly to the C-SROM, the multilevel stochastic ROM (ML-SROM) is based on the nonparametric probabilistic approach of uncertainties. This approach allows for taking into account both the model-parameter uncertainties and the model uncertainties induced by the modeling errors. The ML-NROM previously presented is based on the use of three orthogonal ROBs represented by the matrices $[\Phi^{\mathcal{L}}]$, $[\Phi^{\mathcal{M}}]$, and $[\Phi^{\mathcal{H}}]$, which are constituted of LF-, MF-, and HF-type displacements, respectively. For instance, as explained in Section 4.1, the LF-type displacements consist of long-wavelength global displacements, in contrast to the short-wavelength local displacements associated with the HF regime. When a small design change is performed in the structure, the local displacements that exist in the modified part of the structure are likely to vary a lot, whereas the shape of the global displacements is not really modified. Subsequently and as it is well known, the local displacements are more sensitive to uncertainties than the global displacements.

For a given random matrix $[\mathbf{A}]$ representing $[\mathbf{M}]$, $[\mathbf{D}]$ or $[\mathbf{K}]$ of the ML-SROM, which is associated with the corresponding deterministic matrix $[A]$ representing $[M]$, $[D]$ or $[K]$ of the ML-NROM, three dispersion hyperparameters, $\delta_A^{\mathcal{L}}$, $\delta_A^{\mathcal{M}}$, and $\delta_A^{\mathcal{H}}$ are introduced. These parameters are intended to allow each type of displacements to be affected by a particular level of uncertainties. For $\mathcal{S}$ equal to $\mathcal{L}$, $\mathcal{M}$ or $\mathcal{H}$, the dispersion hyperparameter $\delta_A^{\mathcal{S}}$ is such (see Eq. (2.8)) that

$$(\delta_A^{\mathcal{S}})^2 = \frac{1}{n_{\mathcal{S}}}\, E\{|||[\mathbf{G}_{n_{\mathcal{S}}}(\delta_A^{\mathcal{S}})] - [I_{n_{\mathcal{S}}}]|||_F^2\}\,. \tag{4.36}$$

The random matrix $[\mathbf{G}_A]$ with values in the set of all the positive-definite symmetric $(n_t \times n_t)$ real matrices, is written as

$$[\mathbf{G}_A] = \begin{bmatrix} [\,\mathbf{G}_{n_{\mathcal{L}}}(\delta_A^{\mathcal{L}})\,] & [\quad 0 \quad] & [\quad 0 \quad] \\ [\quad 0 \quad] & [\mathbf{G}_{n_{\mathcal{M}}}(\delta_A^{\mathcal{M}})] & [\quad 0 \quad] \\ [\quad 0 \quad] & [\quad 0 \quad] & [\,\mathbf{G}_{n_{\mathcal{H}}}(\delta_A^{\mathcal{H}})\,] \end{bmatrix}, \tag{4.37}$$

in which the random matrices $[\mathbf{G}_{n_{\mathcal{L}}}(\delta_A^{\mathcal{L}})]$, $[\mathbf{G}_{n_{\mathcal{M}}}(\delta_A^{\mathcal{M}})]$, and $[\mathbf{G}_{n_{\mathcal{H}}}(\delta_A^{\mathcal{H}})]$, with dimensions $(n_{\mathcal{L}} \times n_{\mathcal{L}})$, $(n_{\mathcal{M}} \times n_{\mathcal{M}})$, and $(n_{\mathcal{H}} \times n_{\mathcal{H}})$, are statistically independent and are constructed similarly to the $(n \times n)$ random matrix $[\mathbf{G}_n(\delta_{\mathcal{A}})]$ involved in Eq. (2.7). Performing the Cholesky factorization $[A] = [L_A]^T[L_A]$, in which $[L_A]$ is an upper-triangular matrix, the random matrix $[\mathbf{A}]$ is constructed as

$$[\mathbf{A}] = [L_A]^T[\mathbf{G}_A][L_A]\,. \tag{4.38}$$

The ML-SROM allows the random displacements $\mathbf{U}(\omega)$ associated with $\mathbb{U}(\omega)$ to be obtained as

$$\mathbf{U}(\omega) = [\Psi]\mathbf{Q}(\omega), \tag{4.39}$$

in which the $\mathbb{C}^{n_t}$-valued random variable $\mathbf{Q}(\omega)$ is the solution of the random matrix-equation,

$$(\, -\omega^2[\mathbf{M}] + i\omega[\mathbf{D}] + [\mathbf{K}]\,)\,\mathbf{Q}(\omega) = \mathbf{f}(\omega)\,. \tag{4.40}$$

For all ω in $\mathcal{B}$, the random equation defined by Eq. (4.40) is solved with the Monte-Carlo simulation method.

Chapter 5

Statistical inverse identification of the multilevel stochastic reduced-order model: application to an automobile

5.1 Problem definition

5.1.1 Experimental measurements (excitation force and observation points) and frequency band of analysis

Experimental measurements of some FRFs have been carried out for $n_e = 20$ nominally identical cars over a broad frequency band, $\mathcal{B} = 2\pi \times [10\,,900]$ Hz. For each car, the same excitation force is applied at one of the engine fasteners and the acceleration (following a given direction) is measured at two locations referenced as the observation 1 that is far away from the excitation force and as the observation 2 that is close to the excitation force.

5.1.2 Computational model

The finite element model is very dense and complex, including several kinds of elements (springs, bars, beams, plates, shells, volume elements), rigid bodies and constraint equations, with a total of $m = 7{,}872{,}583$ DOFs. A view of the finite element model is displayed in Fig. 5.1.

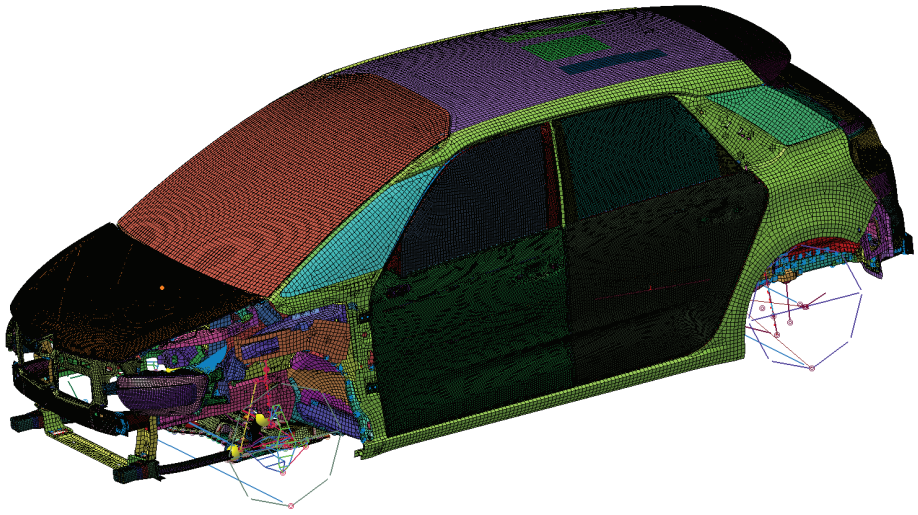

Figure 5.1: View of the finite element model of the automobile.

5.1.3 Modal density characterizing the dynamics and definition of the LF, MF, and HF bands

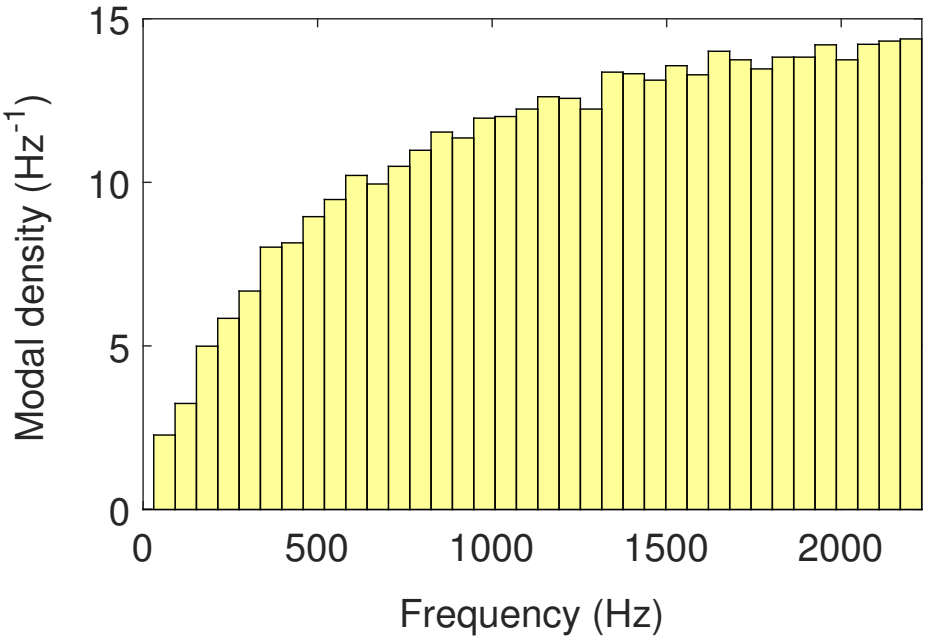

Figure 5.2: Modal density calculated with the computational model.

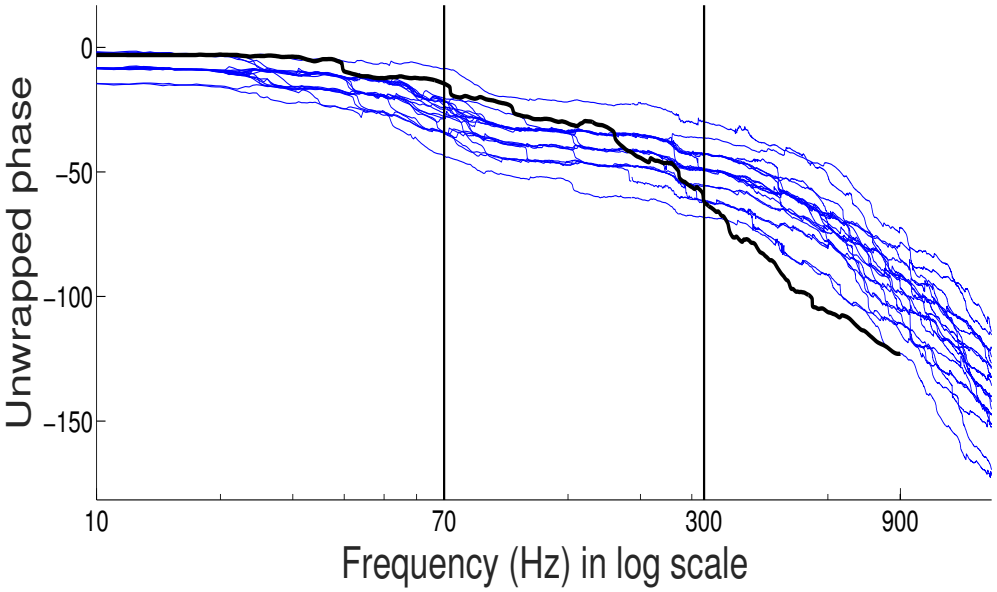

Figure 5.3: Graph of the unwrapped phase as a function of the frequency in logarithmic scale for the observation 1. Computational model (thick line) and 20 experimental measurements performed on the PSA cars of the same type [119] (thin lines).

An intensive computational effort has been carried out for calculating the 24,578 elastic modes that are in the frequency band $[0\,,2200]$ Hz. The graph of the modal density corresponding to these 24,578 elastic modes is displayed in Fig. 5.2.

From this calculation, it can be seen that there are 7,258 elastic modes in frequency band $\mathcal{B}$. There are several possible definitions of the frequency bands $\mathcal{B}_{\mathcal{L}}$, $\mathcal{B}_{\mathcal{M}}$, and $\mathcal{B}_{\mathcal{H}}$ for a complex dynamical system. The definitions greatly depend on the use that is made of the bands defined. In the present framework devoted to the construction of a multilevel model reduction in structural vibrations, we choose the approach proposed in [43], which is based on the analysis of the graph of the unwrapped phase as a function of the frequency in logarithmic scale for the observation 1 that is far away from the excitation force and consequently, for which the propagation follows a long path. It is recalled that the unwrapped phase corrects the radian phase angles by adding multiples of $\pm 2\pi$ when absolute jumps between two consecutive sampled frequencies are greater than or equal to the jump tolerance of π radians. It is known that in the LF range, the phase rotates of π around an eigenfrequency while, in the HF band, the unwrapped phase decreases quasi-linearly. Figure 5.3 displays the graph of the unwrapped phase obtained with the computational model, which is compared to the 20 graphs that correspond to the experimental measurements. The analysis of this figure allows

for defining the following frequency bands $\mathcal{B}_\mathcal{L} = [10, 70]$ Hz, $\mathcal{B}_\mathcal{M} =]70, 300]$ Hz, and $\mathcal{B}_\mathcal{H} =]300, 900]$ Hz. There are 159 elastic modes in low-frequency band $\mathcal{B}_\mathcal{L}$, 1,202 elastic modes in medium-frequency band $\mathcal{B}_\mathcal{M}$, and 5,897 elastic modes in high-frequency band $\mathcal{B}_\mathcal{H}$, or, in average, about 2.5 modes per Hz in $\mathcal{B}_\mathcal{L}$, 5 modes per Hz in $\mathcal{B}_\mathcal{M}$, and 10 modes per Hz in $\mathcal{B}_\mathcal{H}$. A modal density of 2.5 modes per Hz is quite high for the LF band of such a structure. This unusual feature is due to the presence of numerous local displacements in addition to the usual global displacements. For higher frequencies, the density of local elastic modes keeps increasing, which yields a large number of elastic modes for the modal analysis.

5.1.4 Damping model for the automobile

The provided finite element model does not include a damping matrix, $[\mathbb{D}]$, and consequently, the damping model is introduced at the ROM level. For each ROM constructed in this application, the physical damping is introduced through the use of a modal damping model. In the LF band and in the MF band, a multi-parameter modal damping model is fitted by using the experimental FRFs. In the HF band, a one-parameter modal damping model is identified by using the experimental FRFs, for which the parameter is denoted by $c_\mathcal{H}$. For the deterministic ROMs, three cases have to be considered in order to properly define the damping model, depending on which ROM is used.

- The damping matrix of the C-NROM involved in Eq. (2.5) is defined by $[\mathcal{D}] = 2[\Xi(c_\mathcal{H})][\Lambda]^{1/2}$, in which the diagonal matrix $[\Lambda]$ is defined by Eq. (2.6) and where $[\Xi(c_\mathcal{H})]$ is a $(n \times n)$ diagonal matrix of modal damping rates, which depend on parameter $c_\mathcal{H}$ that has to be identified with respect to the experimental measurements, in a deterministic framework. In such a case, Eq. (2.5) consists of a diagonal matrix-equation.

- The damping matrix of the scale-$\mathcal{S}$ ROM involved in Eq. (4.27) is defined by $[\mathcal{D}^\mathcal{S}] = 2[\Xi^\mathcal{S}(c_\mathcal{H})][\Lambda^\mathcal{S}]^{1/2}$, with $[\Lambda^\mathcal{S}]$ the diagonal matrix involved in Eq. (4.28) and where $[\Xi^\mathcal{S}(c_\mathcal{H})]$ is a $(n_\mathcal{S} \times n_\mathcal{S})$ diagonal matrix of damping rates, which depend on parameter $c_\mathcal{H}$ that has to be identified with respect to the experimental measurements, in a deterministic framework. In such a case, Eq. (4.27) consists of a diagonal matrix-equation.

- Concerning the ML-NROM, reduced stiffness matrix $[K]$ involved in Eq. (4.31) is a full matrix. In order to solve latter matrix equation, one possibility is to perform a change of basis in order to diagonalize reduced matrices $[K]$ and $[M]$. Doing so leads us back to scale-t ROM, for which the definition of the damping matrix $[\mathcal{D}^t]$ is given in the item before.

The modal damping rate number α of the classical ROM is given by

$$[\Xi(c_{\mathcal{H}})]_{\alpha\alpha} = \xi(\omega_\alpha; c_{\mathcal{H}})\,, \tag{5.1}$$

in which $\omega_\alpha = [\Lambda]_{\alpha\alpha}^{1/2}$ and where the modal damping function $(\omega; c) \mapsto \xi(\omega; c_{\mathcal{H}})$ is defined as follows. In the LF and MF bands, modal damping function ξ is independent of damping parameter $c_{\mathcal{H}}$. Concerning the rest of the band, the value of function ξ reaches the value of $c_{\mathcal{H}}$ for the maximum angular frequency ω_n. Figure 5.4 displays the graphs of this function for three distinct values of damping parameter $c_{\mathcal{H}}$.
Similarly, the damping rate number α of scale-$\mathcal{S}$ ROM is given by

$$[\Xi^{\mathcal{S}}(c_{\mathcal{H}})]_{\alpha\alpha} = \xi^{\mathcal{S}}(\omega_\alpha^{\mathcal{S}}; c_{\mathcal{H}})\,, \tag{5.2}$$

in which $\omega_\alpha^{\mathcal{S}} = [\Lambda^{\mathcal{S}}]_{\alpha\alpha}^{1/2}$ and where damping function $(\omega; c) \mapsto \xi^{\mathcal{S}}(\omega; c_{\mathcal{H}})$ is defined as follows. In the LF and MF bands, the damping function $\xi^{\mathcal{S}}$ is the same as ξ. Concerning the rest of the band, it is similar to ξ: the value of function $\xi^{\mathcal{S}}$ reaches the value of $c_{\mathcal{H}}$ for the maximum angular frequency $\omega_{n_{\mathcal{S}}}^{\mathcal{S}}$.

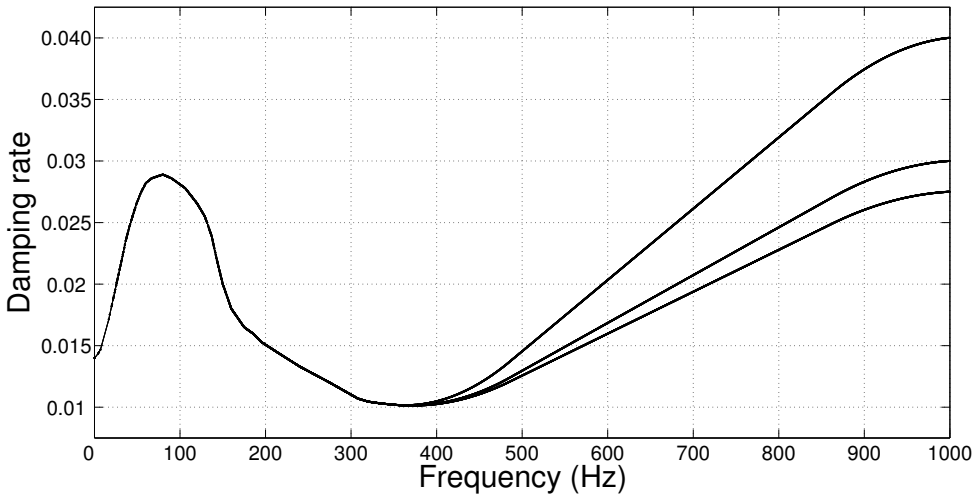

Figure 5.4: Modal damping function $(\omega; c_{\mathcal{H}}) \mapsto \xi(\omega; c)$ plotted, with respect to the frequency in Hz, for: $c_{\mathcal{H}} = 0.0275$ (bottom line), $c_{\mathcal{H}} = 0.03$ (middle line), and $c_{\mathcal{H}} = 0.04$ (top line).

For the stochastic ROMs, two cases have to be considered in order to properly define the random matrix of the damping model, depending on which stochastic ROM is used.

- The definition given in Eq. (2.7) to random damping matrix $[\boldsymbol{\mathcal{D}}]$ of the C-SROM involved in Eq. (2.15) is not used. In order to solve Eq. (2.15), the random generalized eigenvalue problem associated with random reduced matrices $[\boldsymbol{\mathcal{K}}]$ and $[\boldsymbol{\mathcal{M}}]$ is solved, which yields the diagonal matrix, $[\boldsymbol{\Lambda}]$, of the random eigenvalues and the matrix, $[\boldsymbol{\Phi}]$, of the associated random eigenvectors. Equation (2.15) is then projected onto the stochastic ROB $[\boldsymbol{\Phi}]$. In order to obtain a diagonal matrix-equation, random damping matrix $[\boldsymbol{\mathcal{D}}]$ of the C-SROM is then constructed similarly to deterministic damping matrix $[\mathcal{D}]$ of the C-NROM given hereinbefore, except that diagonal matrix $[\Lambda]$ is replaced by the diagonal random matrix $[\boldsymbol{\Lambda}]$ constituted of the random eigenvalues. The parameter $c_{\mathcal{H}}$ has to be identified with respect to the experimental measurements, in a stochastic framework.

- The definition given in Eq. (4.38) to random damping matrix $[\mathbf{D}]$ of the ML-SROM involved in Eq. (4.40) is not used. In order to solve Eq. (4.40), the random generalized eigenvalue problem associated with random reduced matrices $[\mathbf{K}]$ and $[\mathbf{M}]$ is solved, which yields the diagonal matrix, $[\boldsymbol{\Sigma}]$, of the random eigenvalues and the matrix, $[\boldsymbol{\Psi}]$, of the associated random eigenvectors. Equation (4.40) is then projected onto the stochastic ROB $[\boldsymbol{\Psi}]$. In order to obtain a diagonal matrix-equation, random damping matrix $[\mathbf{D}]$ of the ML-SROM is then constructed similarly to deterministic damping matrix $[D]$ of the ML-NROM given hereinbefore, except that diagonal matrix $[\Lambda^t]$ is replaced by the diagonal random matrix $[\boldsymbol{\Sigma}]$ constituted of the random eigenvalues. The parameter $c_{\mathcal{H}}$ has to be identified with respect to the experimental measurements, in a stochastic framework.

5.1.5 Definition of the observations

Let $\mathbb{U}_{(1)}(\omega), \ldots, \mathbb{U}_{(n_j)}(\omega)$ be the n_j scalar observations that are made up of DOFs or of combinations of DOFs of the displacement vector $\mathbb{U}(\omega)$ involved in Eq. (2.1). In this application, we have $n_j = 2$ (corresponding to the two experimental observations). For each j, the computed observation is defined as the modulus $\omega \mapsto u_j^c(\omega)$ in dB scale,

$$u_j^c(\omega) = 20 \log_{10} |\mathbb{U}_{(j)}(\omega)| \,, \tag{5.3}$$

in which $|.|$ is the modulus of a complex number. The counterpart for the experimental measurements of the $k = 1, \ldots, n_e$ cars (with $n_e = 20$) is denoted by $\omega \mapsto u_{j,k}^e(\omega)$ whose definition is the same as the definition of $u_j^c(\omega)$.

5.1.6 Defining the objective function used for the convergence analyses of the deterministic computational ROMs

In order to define a distance between the computed deterministic FRFs and the experimental FRFs, an objective function, J_d, is defined by

$$J_d^2 = \frac{1}{n_j} \sum_{j=1}^{n_j} \frac{1}{n_e} \sum_{k=1}^{n_e} \frac{1}{|\mathcal{B}|} \int_{\mathcal{B}} (u_j^c(\omega) - u_{j,k}^e(\omega))^2 d\omega \,, \tag{5.4}$$

in which $|\mathcal{B}| = \omega_{\max} - \omega_{\min}$. It should be noted that the construction of J_d would remain unchanged if, in Eq. (5.4), the displacements were replaced by their corresponding accelerations.

5.1.7 Defining the objective function used for the identification of the stochastic computational ROMs

The parameters of the stochastic computational ROMs have to be identified with respect to the experimental measurements (solving a statistical inverse problem). Let $U_j^e(\omega)$ be the real-valued random variable for which $u_{j,1}^e(\omega), \ldots, u_{j,n_e}^e(\omega)$ are n_e independent realizations. Let $U_j^c(\omega)$ be the real-valued random variable corresponding to the deterministic quantity $u_j^c(\omega)$. The following objective function, J_s , is introduced

$$J_s = \frac{1}{n_j} \sum_{j=1}^{n_j} J_{s,j} \,, \tag{5.5}$$

in which the objective function $J_{s,j}$ associated with observation $j = 1, \ldots, n_j$ is written as

$$J_{s,j} = \frac{1}{|\mathcal{B}|} \int_{\mathcal{B}} \mathrm{OVL}\left(U_j^c(\omega), U_j^e(\omega)\right) d\omega \,. \tag{5.6}$$

In Eq. (5.6), the function $(X, Y) \mapsto \mathrm{OVL}\,(X, Y)$ is defined by

$$\mathrm{OVL}\,(X, Y) = 1 - \frac{1}{2} \int_{\mathbb{R}} |p_X(x) - p_Y(x)| \, dx \,, \tag{5.7}$$

in which X and Y are real-valued random variables, for which p_X and p_Y are the probability density functions. Function OVL is known as the overlapping coefficient [138]. For all $j = 1, \ldots, n_j$ and all ω in $\mathcal{B}$, n_{sim} realizations of random

variable $U_j^c(\omega)$ are computed by using the Monte-Carlo simulation method. The probability density functions are estimated by using the kernel density estimation method. It can easily be proved that the values of J_s, of $J_{s,j}$ for $j = 1, \ldots, n_j$, and of the OVL function, are between 0 and 1 (with 1 meaning a perfect match).

5.2 Classical nominal ROM and classical stochastic ROM

In a first step, the dimension n of the C-NROM (deterministic) is calculated by performing a convergence analysis of J_d as a function of n. For this value of n, the C-NROM is used for computing the deterministic FRFs that are compared to their experimental counterparts. In a second step, for the value of n determined in the first step, the hyperparameters of the C-SROM (stochastic) are identified by maximizing the objective function J_s. Using the identified values of the hyperparameters, the C-SROM is used for estimating the confidence regions of the random FRFs, which are compared to the experimental measurements.

5.2.1 First step: C-NROM

5.2.1.1 Convergence analysis of J_d as a function of n

The C-NROM is obtained by using Eqs. (2.4) and (2.5). A convergence analysis of the C-NROM is performed with respect to its dimension n and to parameter $c_{\mathcal{H}}$ that controls the damping model. For each value of n, the optimal value, $c_{\mathcal{H}}(n)$, of $c_{\mathcal{H}}$ is identified, in minimizing J_d. For each pair $(n\,, c_{\mathcal{H}}(n))$, Fig. 5.5 displays the graph of J_d as a function of n and shows that convergence is reached starting from n = 7,000. Nevertheless, we choose n = 8,450 (for which f_n = 1,000 Hz), in order (1) to have subspace $\mathcal{S}_c$ sufficiently rich for the construction of subspace $\mathcal{S}_t \subseteq \mathcal{S}_c$ of the multilevel ROM and (2) to have a classical ROM associated with eigenfrequencies covering more than whole band $\mathcal{B}$ for obtaining a satisfactory stochastic ROM.

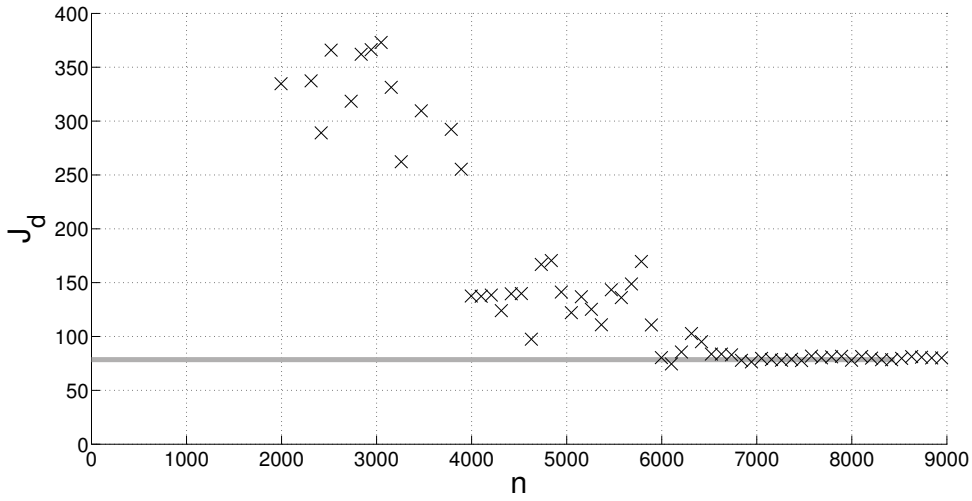

Figure 5.5: Convergence of the C-NROM with respect to its dimension: value of J_d for several values of n (black crosses). Horizontal light-gray line: value of J_d for $n = 8{,}450$.

5.2.1.2 Deterministic FRFs and experimental comparisons

The FRFs provided by the C-NROM, associated with observation 1 (acceleration related to the displacement $\omega \mapsto u_1^c(\omega)$) and with observation 2 (acceleration related to the displacement $\omega \mapsto u_2^c(\omega)$), are plotted in Figs. 5.6 and 5.7 and are compared to the $n_e = 20$ experimental FRFs (accelerations related to displacements $\omega \mapsto u_{j,k}^e(\omega)$ with $k = 1, \ldots, n_e$). These figures clearly show that

- the experimental variabilities strongly increase with the frequency (it should be noted that the relative important experimental variabilities in the LF band for observation 1 that can be seen in Fig. 5.6 is due to measurement noise).

- significant differences between the prediction of the computational model and the experimental measurements can be observed, in particular in the MF band.

- the big experimental variabilities cannot be represented by a simple deterministic prediction, which would require the prediction of confidence regions with a stochastic model.

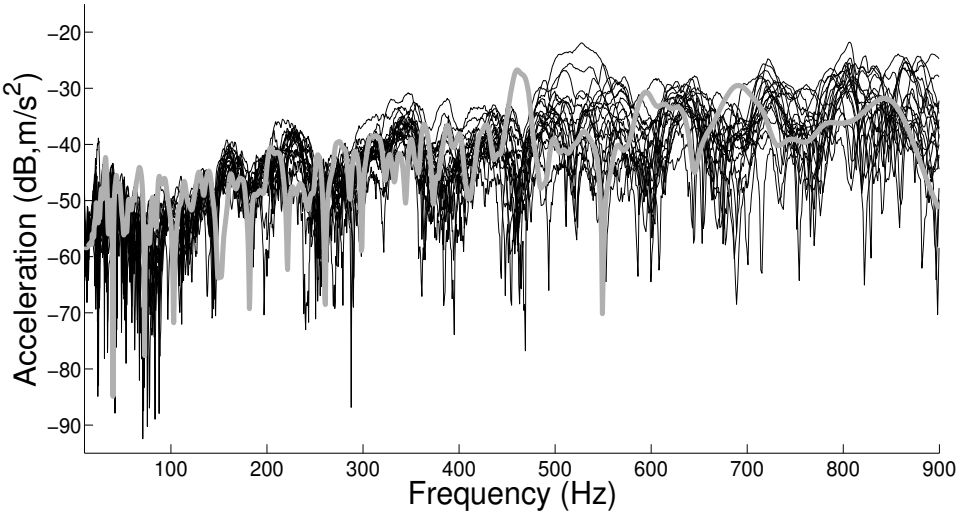

Figure 5.6: Observation 1: experimental FRF measurements performed on the PSA cars of the same type [119] (black lines), deterministic FRF using the C-NROM (gray line).

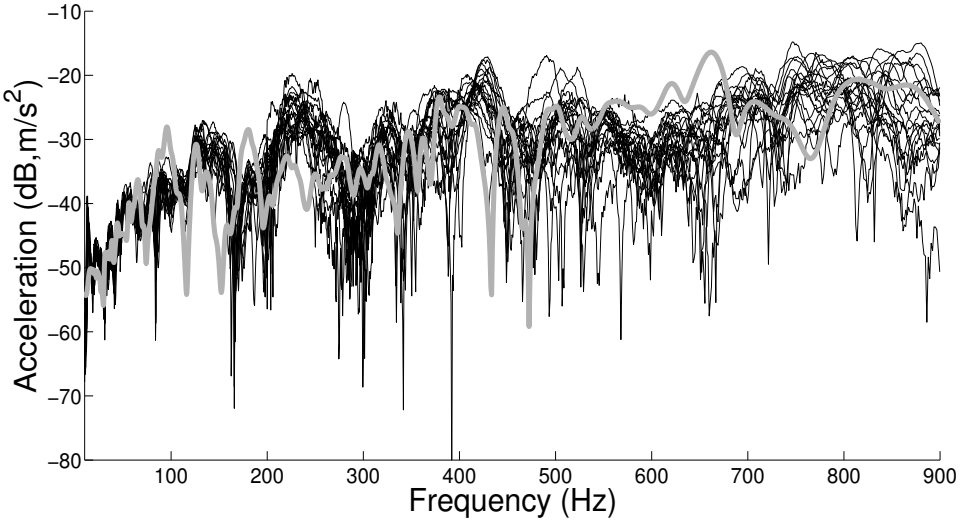

Figure 5.7: Observation 2: experimental FRF measurements performed on the PSA cars of the same type [119] (black lines), deterministic FRF using the C-NROM (gray line).

5.2.2 Second step: C-SROM

5.2.2.1 Experimental identification of the C-SROM

The C-SROM is obtained by using Eqs. (2.14) and (2.15) for which the dispersion hyperparameters and damping parameter $c_{\mathcal{H}}$ must be identified with respect to the experimental measurements, by solving a statistical inverse problem. The random damping matrix $[\boldsymbol{\mathcal{D}}]$ of the C-SROM is the one defined in Section 5.1.4 and consequently, there is no dispersion hyperparameter $\delta_{\mathcal{D}}$. The statistical inverse problem consists in computing the optimal values $\delta_{\mathcal{M}}^{\text{opt}}$, $\delta_{\mathcal{K}}^{\text{opt}}$, and $c_{\mathcal{H}}^{\text{opt}}$ of the optimization problem defined as the maximization of the objective function J_s with respect to the three parameters $\delta_{\mathcal{M}}$, $\delta_{\mathcal{K}}$, and $c_{\mathcal{H}}$ in the set of their admissible values. The optimization problem is not convex and a trial method is used by introducing a fine grid of the admissible set with an non-homogeneous distribution of the sampling points (that can be viewed in Fig. 5.8). For each point $(\delta_{\mathcal{M}}, \delta_{\mathcal{K}})$ in the grid, $c_{\mathcal{H}} \mapsto J_s(\delta_{\mathcal{M}}, \delta_{\mathcal{K}}, c_{\mathcal{H}})$ is maximized yielding the optimal value $c_{\mathcal{H}}^{\star}(\delta_{\mathcal{M}}, \delta_{\mathcal{K}})$. Figure 5.8 displays the graph of function $(\delta_{\mathcal{M}}, \delta_{\mathcal{K}}) \mapsto J_s(\delta_{\mathcal{M}}, \delta_{\mathcal{K}}, c_{\mathcal{H}}^{\star}(\delta_{\mathcal{M}}, \delta_{\mathcal{K}}))$ calculated at the sampling points of the grid. It can be seen there is a quasi-symmetry with respect to $\delta_{\mathcal{M}} = \delta_{\mathcal{K}}$ axis. It can then be deduced the optimal solution, for which $\delta_{\mathcal{M}}^{\text{opt}} = 0.13$ and $\delta_{\mathcal{K}}^{\text{opt}} = 0.11$.

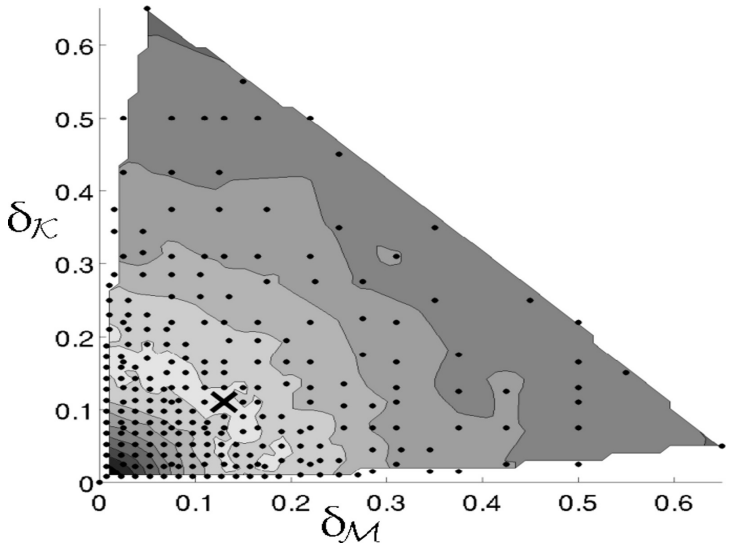

Figure 5.8: Plot of function $(\delta_{\mathcal{M}}, \delta_{\mathcal{K}}) \mapsto J_s(\delta_{\mathcal{M}}, \delta_{\mathcal{K}})$ for the identification of hyperparameters $\delta_{\mathcal{M}}$ and $\delta_{\mathcal{K}}$ of the C-SROM. Black dots: sampling points, black cross: optimal point.

Concerning the calculation of the objective function, for each sampling point of the grid, the value of the objective function J_s is estimated using n_{sim} Monte-Carlo simulations. Figure 5.9 presents the convergence of the objective function J_s as a function of n_{sim} evaluated at the optimal point $(\delta_{\mathcal{M}}^{\text{opt}}, \delta_{\mathcal{K}}^{\text{opt}}, c_{\mathcal{H}}^{\text{opt}})$. It can be seen that, for a reasonable precision of J_s (of about 0.01), convergence is reached quite fast for $n_{\text{sim}} = 40$, which can be considered as a good compromise between the numerical cost and the accuracy (it would make little sense to carry out a very fine statistical estimation if not exploring the parameter space with a sufficiently fine grid – and vice versa).

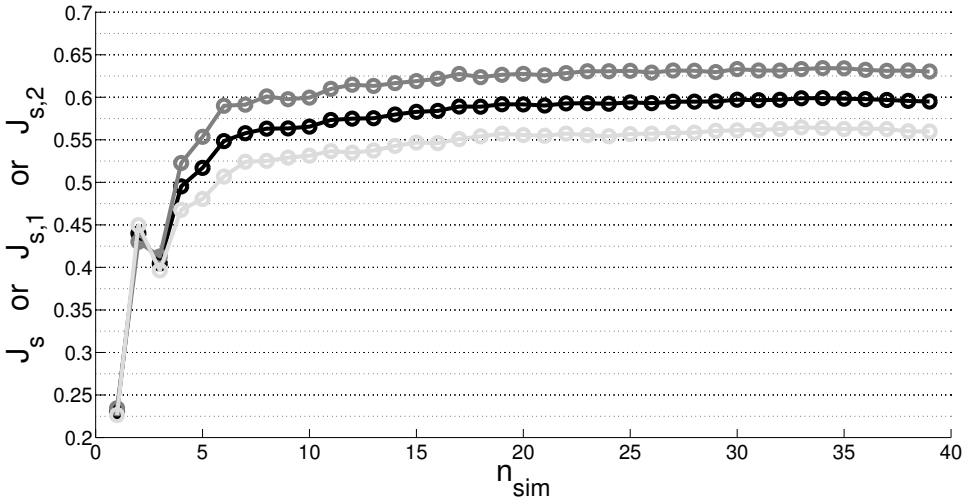

Figure 5.9: Convergence of objective function J_s (black line), of $J_{s,1}$ (dark-gray line), and of $J_{s,2}$ (light-gray line) with respect to number of simulations n_{sim}.

Concerning the computational cost, for each independent realization of random matrices $[\boldsymbol{\mathcal{M}}]$ and $[\boldsymbol{\mathcal{K}}]$ in Eq. (2.15), the matrix equation is diagonalized (solving the generalized eigenvalue problem of reduced dimension associated with the conservative dynamical system) for obtaining an efficient resolution over (1) the frequency sampling and (2) the sampling of parameter $c_{\mathcal{H}}$.

5.2.2.2 Confidence regions of the random FRFs and experimental comparison

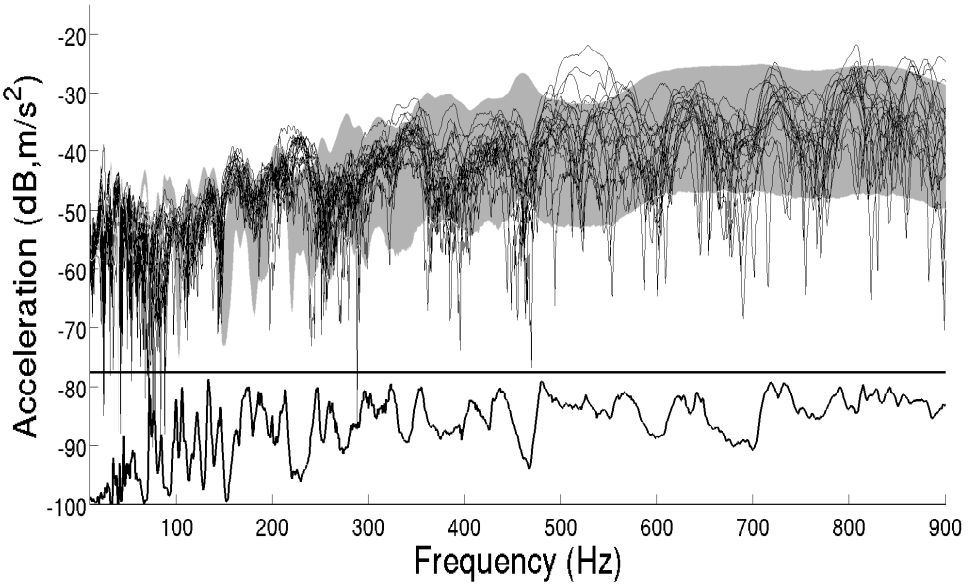

Figure 5.10: Observation 1: experimental FRF measurements performed on the PSA cars of the same type [119] (black lines), random FRF using the identified C-SROM (gray region), and overlap function OVL (black line underneath).

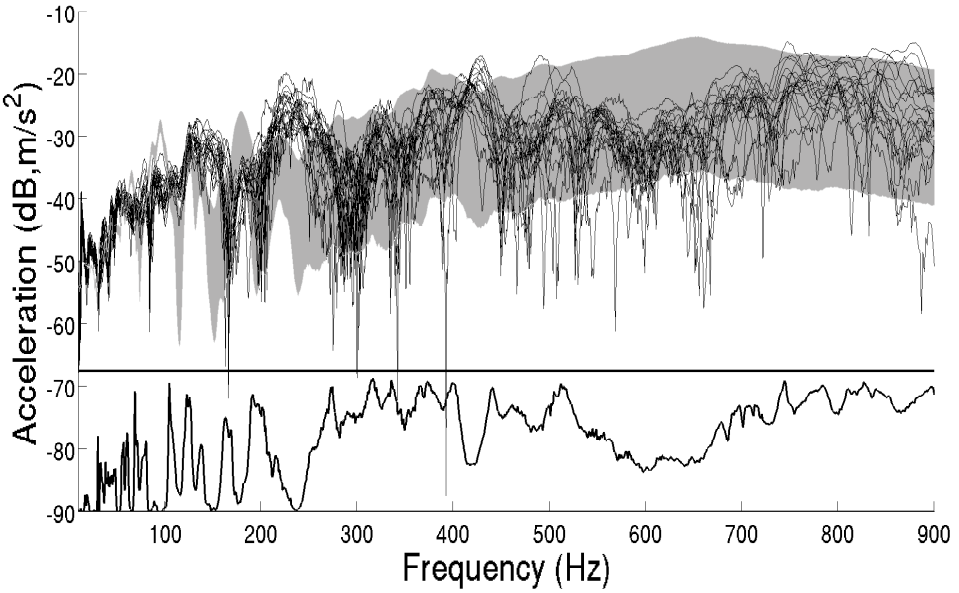

Figure 5.11: Observation 2: experimental FRF measurements performed on the PSA cars of the same type [119] (black lines), random FRF using the identified C-SROM (gray region), and overlap function OVL (black line underneath).

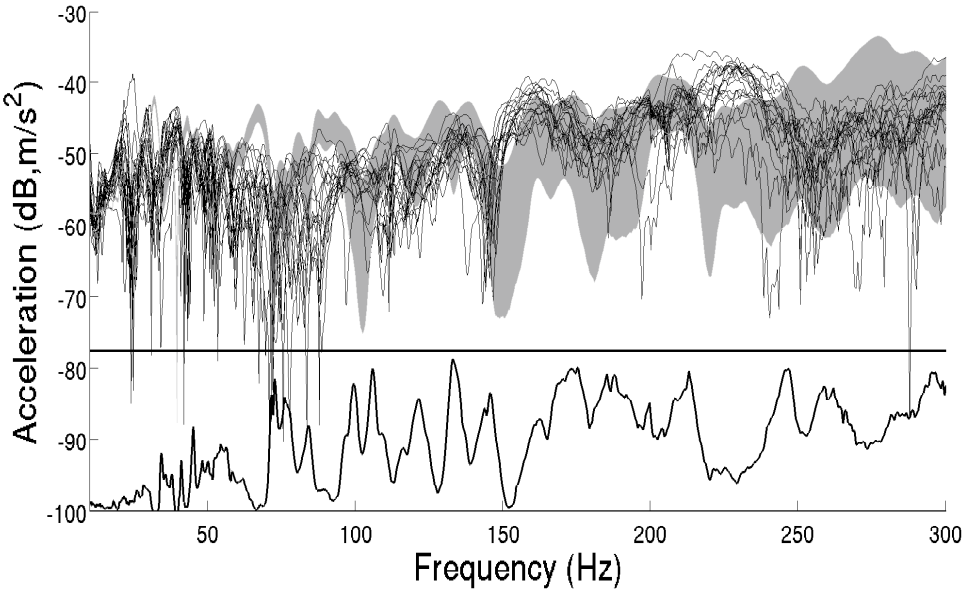

Figure 5.12: Observation 1, zoom into band $\mathcal{B}_{\mathcal{L}} \cup \mathcal{B}_{\mathcal{M}}$: experimental FRF measurements performed on the PSA cars of the same type [119] (black lines), random FRF using the identified C-SROM (gray region), and overlap function OVL (black line underneath).

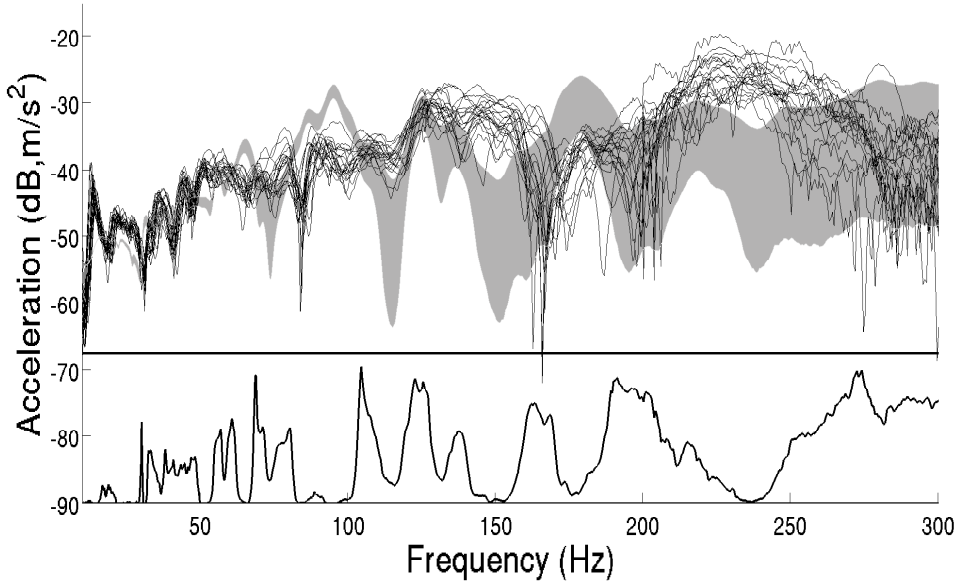

Figure 5.13: Observation 2, zoom into band $\mathcal{B}_{\mathcal{L}} \cup \mathcal{B}_{\mathcal{M}}$: experimental FRF measurements performed on the PSA cars of the same type [119] (black lines), random FRF using the identified C-SROM (gray region), and overlap function OVL (black line underneath).

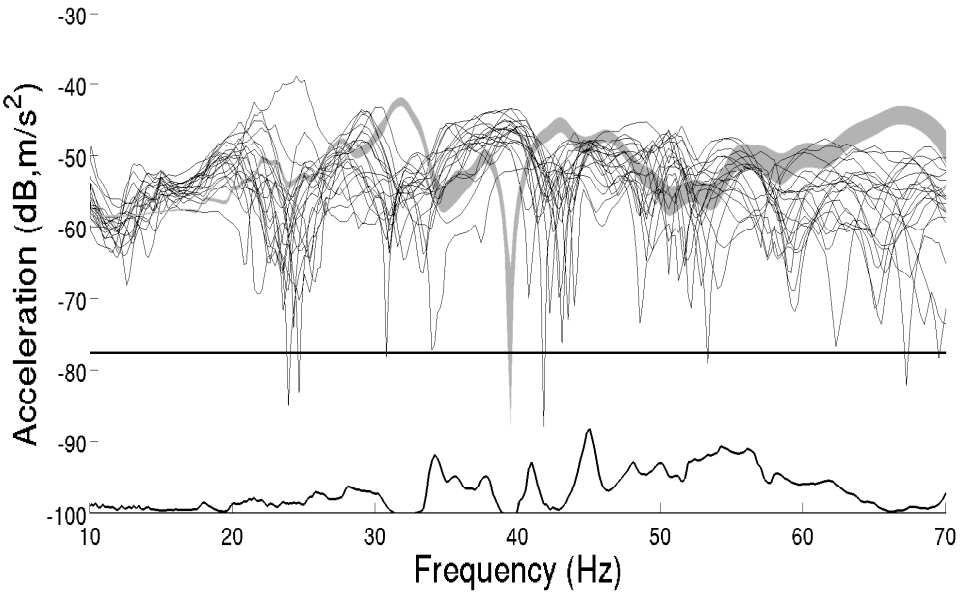

Figure 5.14: Observation 1, zoom into band $\mathcal{B}_{\mathcal{L}}$: experimental FRF measurements performed on the PSA cars of the same type [119] (black lines), random FRF using the identified C-SROM (gray region), and overlap function OVL (black line underneath).

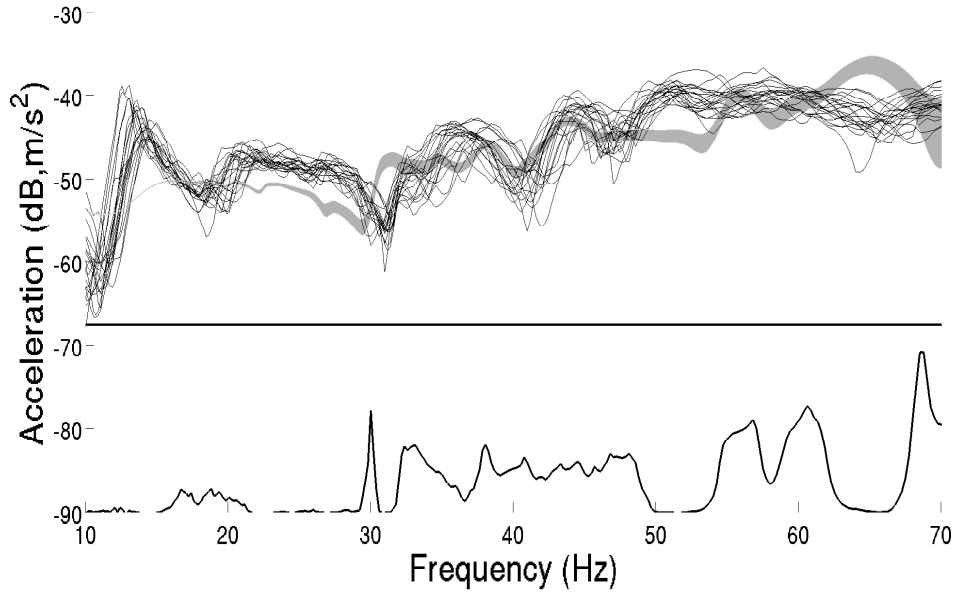

Figure 5.15: Observation 2, zoom into band $\mathcal{B}_{\mathcal{L}}$: experimental FRF measurements performed on the PSA cars of the same type [119] (black lines), random FRF using the identified C-SROM (gray region), and overlap function OVL (black line underneath).

The confidence region (corresponding to a probability level of 95%) of each FRF is computed by using the identified C-SROM. A convergence analysis of the confidence region with respect to the number n_{sim} of realizations in the Monte-Carlo simulation method has been performed. A good convergence of the confidence region is reached for $n_{\text{sim}} = 10{,}000$. The corresponding values of objective functions $J_{s,1}$ and $J_{s,2}$ for the identified C-SROM are $J_{s,1} = 0.62$ and $J_{s,2} = 0.56$, which yields $J_s = 0.59$ (the statistical estimation is done with $n_{\text{sim}} = 10{,}000$). The results for observation 1 and observation 2 are displayed in Figs. 5.10 and 5.11. On each figure it can be seen the confidence region, the 20 experimental measurements, and the OVL function, $\omega \mapsto \text{OVL}(U_j^c(\omega), U_j^e(\omega))$, defined by Eq. (5.7) and plotted between two horizontal lines: the lower horizontal line corresponds to the value 0 and the upper one to the value 1. In Figs. 5.10 and 5.11, it can be seen that, due (1) to the discrepancies of the C-NROM with respect to the experiments and (2) to too narrow confidence regions provided by the C-SROM in the LF band (and to a lesser extent in the MF band), the C-SROM does not perfectly represent most of the experimental FRFs in the LF and MF bands, as it can be seen in Figs. 5.12 and 5.13 that present a zoom of Figs. 5.10 and 5.11 into band $\mathcal{B}_{\mathcal{L}} \cup \mathcal{B}_{\mathcal{M}}$, and in Figs. 5.14 and 5.15 that present a zoom of Figs. 5.10 and 5.11 into band $\mathcal{B}_{\mathcal{L}}$. It can be seen that OVL function confirms the not perfectly correct prediction of the C-SROM in the LF and MF bands. The reason why such a one-level stochastic model of uncertainties is not sufficient for predicting the confidence regions in all the frequency band is that the effects of uncertainties on the FRFs are not homogeneous in the frequency band. It should be noted that, with this one-level stochastic ROM, if one would want to obtain broader confidence regions in the LF band, one could use greater values for the dispersion hyperparameters but in such a case, one would consequently obtain too broad confidence regions in the HF band. The introduction of a multilevel stochastic ROM allows for improving the prediction as demonstrated in the next section.

5.3 Multilevel nominal ROM and multilevel stochastic ROM

In a first step, a deterministic analysis is carried out in order to find suitable filtering parameters, which affect the reduction of the dimension of the model. In fact, this deterministic analysis is not sufficient in itself, as the final objective is the experimental identification of the ML-SROM. Consequently, in a second step, all the filtering parameters defining the multilevel ROB and all the dispersion hyperparameters are simultaneously identified. To this end, first, a temporary choice of filtering parameters defining the ML-NROM is done, based on the de-

terministic analysis. Then, a sensitivity analysis with respect to the dispersion hyperparameters allows for decreasing the number of dispersion hyperparameters to be identified. Based on this assumption, a $3D$ coarse grid allows for finding initial values for the dispersion hyperparameters. All the other parameters being fixed, the filtering parameters of the HF band and the dispersion hyperparameter of the HF band are simultaneously identified in a precise way. Finally, defining the values of the other filtering parameters independently of the global optimization problem, the remaining dispersion hyperparameters are identified at a low cost. Using the identified ML-SROM, the confidence regions of the random FRFs are statistically estimated and are then compared to the experimental measurements.

5.3.1 First step: ML-NROM

5.3.1.1 Convergence analysis of J_d as a function of dimension n_t deduced from a first filtering

For constructing the multilevel ROM, the first step consists in defining the filtering of local displacements that is devoted to the reduction of the final dimension n_t of the proposed ROM. This step corresponds to either Eq. (4.3) or Eq. (4.17). It depends on the maximum degree $d_{\mathcal{H}}$ of the polynomials of the reduced kinematics of mass matrix $[\mathbb{M}^r]$, on truncation order $\nu_{\mathcal{H}}$ that is indirectly related to the upper bound of the frequency band (through the value $\sqrt{\sigma^t_{\nu_{\mathcal{H}}}}/2\pi$ in which σ^t_α is the eigenvalue of rank α in Eq. (4.11), involved in the mapping $\mathcal{F}_2$ in Eq. (4.17)) and to the cutoff frequency $f^c_{\mathcal{H}}$. It should be noted that since by construction one has $\mathcal{S}_t \subseteq \mathcal{S}_c$, the frequency $f^t_{n_t} = \sqrt{\lambda^t_{n_t}}/2\pi$ verifies the inequality $f^t_{n_t} \leq f_n$. Therefore, choosing $f^c_{\mathcal{H}} = f_n = 1{,}000$ Hz would automatically yield $n_t = \nu_{\mathcal{H}}$. We choose to set $f^c_{\mathcal{H}}$ as $f^c_{\mathcal{H}} = 925$ Hz. It should be noted that scale-t ROM given by Eqs. (4.26) and (4.27) yields the same response as the ML-NROM (by construction). By abuse of terminology, we thus say that exploring the possible values of parameters $d_{\mathcal{H}}$ and $\nu_{\mathcal{H}}$ allows the construction of the ML-NROM to be adjusted. It is recalled that $\lambda^t_{\nu_{\mathcal{H}}} \leq \sigma^t_{\nu_{\mathcal{H}}}$. For fixed $d_{\mathcal{H}}$, some sampling points are explored in a segment in which parameter $\nu_{\mathcal{H}}$ verifies

$$f^c_{\mathcal{H}} \leq \sqrt{\sigma^t_{\nu_{\mathcal{H}}}}/2\pi \leq 10 \times f^c_{\mathcal{H}}\,. \tag{5.8}$$

Figure 5.16 presents a plot of function J_d with respect to parameters $d_{\mathcal{H}}$ and $\nu_{\mathcal{H}}$, with $d_{\mathcal{H}}$ ranging from 2 to 40 and with the corresponding values of $\nu_{\mathcal{H}}$ deduced from Eq. (5.8). It can be seen that for $\nu_{\mathcal{H}} \geq 4{,}000$, the value of J_d is only subjected to small fluctuations. It should also be noted that, in general, for a fixed $\nu_{\mathcal{H}}$ between 2,500 and 4,000, the value of J_d is larger (*i.e.* is less good) for a larger value of $d_{\mathcal{H}}$. This is due to the fact that for an increasing value of $d_{\mathcal{H}}$, the

value of $\nu_{\mathcal{H}}$ has to increase in order that the quantity $\sqrt{\sigma^t_{\nu_{\mathcal{H}}}}/2\pi$ reach the upper bound of the frequency band. Indeed, a larger maximum degree $d_{\mathcal{H}}$ means an increasing presence of local displacements, which means more basis vectors kept in the construction of the ROM.

Figure. 5.17 shows the convergence of the ML-NROM with respect to its dimen-

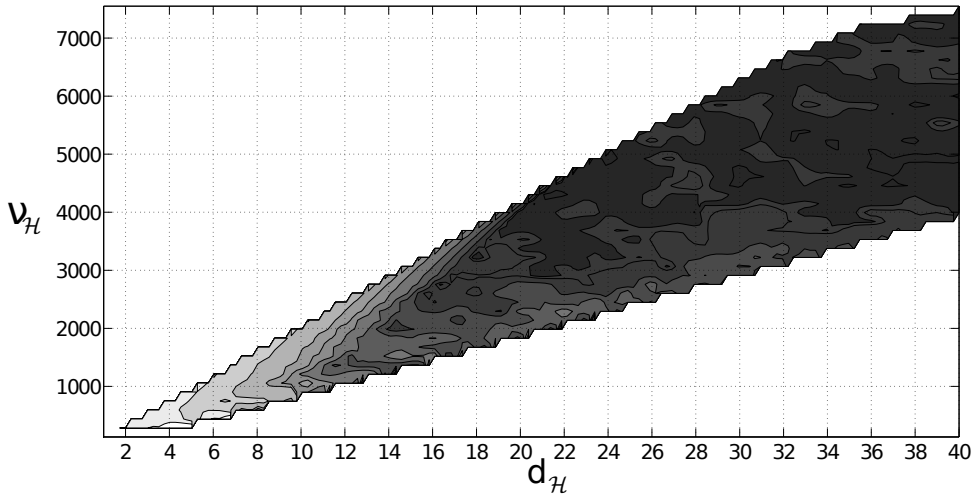

Figure 5.16: Plot of function J_d with respect to parameters $d_{\mathcal{H}}$ and $\nu_{\mathcal{H}}$ (lighter gray level meaning higher J_d)

sion n_t. For this, the value of J_d is plotted as a function of n_t for several ROMs (all the sampling points). Likewise, the convergence of the C-NROM is given on the same figure, in order to put into evidence the faster convergence of the ML-NROM towards a value corresponding to a reasonable accuracy, compared to the C-NROM. This is explained by the fact that the ML-NROM lacks local displacements (and thus has a lower dimension), which are not really important for representing the dynamical responses. For a low maximum degree $d_{\mathcal{H}}$ of the polynomials (and for a low truncation order $\nu_{\mathcal{H}}$), the lower dimension n_t that is obtained for the ROM is associated with more important modeling errors. For constructing the ML-NROM, a good compromise between the value of n_t and the accuracy associated with the value of J_d is sought. In fact, the purpose of the multilevel ROM is to better represent the variabilities of the experimental measurements in the frequency band (i.e. to obtain random FRFs that are able to represent the experimental measurements) and consequently, the identification of parameters $d_{\mathcal{H}}$ and $\nu_{\mathcal{H}}$ depends on the values taken by the dispersion hyperparameters of the ML-SROM (coupled problem). The previous exploration of the possible values of parameters $d_{\mathcal{H}}$ and $\nu_{\mathcal{H}}$ is thus not sufficient. Nevertheless,

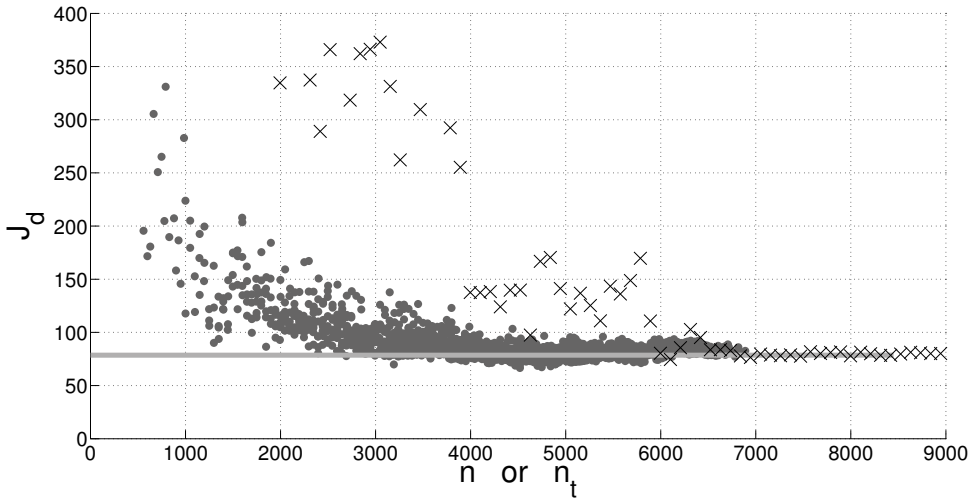

Figure 5.17: For the C-NROM, graph of $n \mapsto J_d(n)$ (black crosses) and graph of $n \mapsto J_d(8{,}450)$ (horizontal light-gray line). For the ML-NROM, graph of $n_t \mapsto J_d(n_t)$ (gray dots).

it allows for defining a sub-region in which the global identification (taking into account the coupling of the dispersion hyperparameters with the filtering parameters) of the ML-SROM will be restrained. Concerning the computational cost, one sampling point involves solving an eigenvalue problem of dimension $\nu_{\mathcal{H}}$ (associated with Eq. (3.27) or Eq. (4.12)). In addition, it implies solving, for each value of the maximum degree $d_{\mathcal{H}}$ of the polynomials, an eigenvalue problem of dimension n (associated with Eq. (3.37) or Eq. (4.11)), which can be solved at a lower cost if $d_{\mathcal{H}}$ (and thus column dimension $r_{\mathcal{H}}$ of matrix $[N^t]$ in Eq. (4.17)) is low, through a SVD (as explained in Remark 2 of Section 3.3). Furthermore, for each value of maximum degree $d_{\mathcal{H}}$ of the polynomials, the matrix $[N^t]$, which is constructed in Eq. (4.10) within the use of mapping $\mathcal{F}_2$ in Eq. (4.17), can be obtained by extracting the first $r_{\mathcal{H}}$ columns of a matrix $[N^t]$ associated with a reduced kinematics of dimension $r_{\mathcal{H},\max}$ that satifies $r_{\mathcal{H},\max} \geq r_{\mathcal{H}}$ for all considered $r_{\mathcal{H}}$. This way, the construction of matrix $[B^\ell]$ and the matrix product with $(m \times n)$ matrix $[\Phi]$ are done once and for all.

5.3.1.2 Deterministic FRFs and experimental comparisons

Figures 5.18 and 5.19 show the deterministic FRFs obtained using the ML-NROM with $d_{\mathcal{H}} = 34$ and $\nu_{\mathcal{H}} = 4{,}250$, which are the optimal values found solving the global stochastic optimization problem presented in the next section. It can be seen that the ML-NROM, with reduced dimension $n_t = 4{,}232$, yields a satisfacory

prediction with respect to that of the C-NROM.

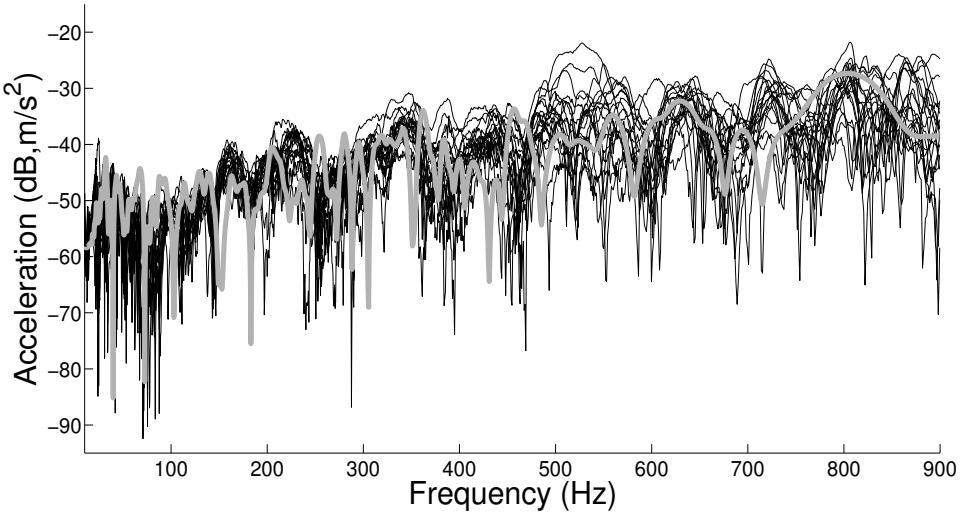

Figure 5.18: Observation 1: experimental FRF measurements performed on the PSA cars of the same type [119] (black lines), deterministic FRF using the identified ML-NROM (gray line)

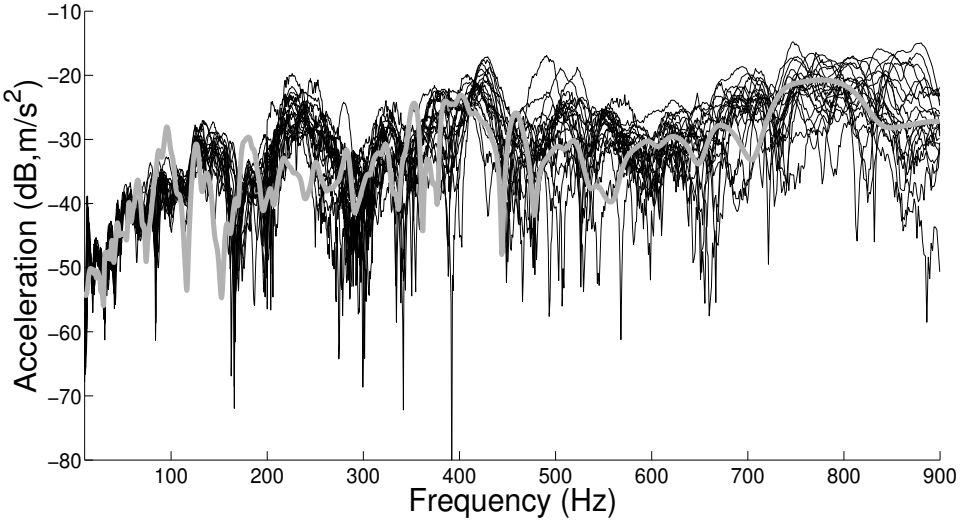

Figure 5.19: Observation 2: experimental FRF measurements performed on the PSA cars of the same type [119] (black lines), deterministic FRF using the identified ML-NROM (gray line)

5.3.2 Second step: ML-SROM

5.3.2.1 Global experimental identification of all the parameters defining the ML-SROM

For the inverse identification of the ML-SROM, the global stochastic optimization problem requires identifying the successive input parameters (filtering parameters) of function $\mathcal{F}_1$ in Eqs. (4.3), (4.4), and (4.6) used for defining the ML-NROM. Based on the ML-NROM, the ML-SROM is constructed upon dispersion hyperparameters $\delta_K^{\mathcal{L}}$, $\delta_M^{\mathcal{L}}$, $\delta_K^{\mathcal{M}}$, $\delta_M^{\mathcal{M}}$, $\delta_K^{\mathcal{H}}$, and $\delta_M^{\mathcal{H}}$ that also have to be identified. The random damping matrix $[\mathbf{D}]$ of the ML-SROM is defined in Section 5.1.4 and consequently, there is no dispersion hyperparameters $\delta_D^{\mathcal{L}}$, $\delta_D^{\mathcal{M}}$, and $\delta_D^{\mathcal{H}}$. The cutoff frequencies $f_{\mathcal{L}}^c$ and $f_{\mathcal{M}}^c$ are chosen as the upper bounds of bands $\mathcal{B}_{\mathcal{L}}$ and $\mathcal{B}_{\mathcal{M}}$, that is to say $f_{\mathcal{L}}^c = 70$ Hz and $f_{\mathcal{M}}^c = 300$ Hz. It is recalled that $f_{\mathcal{H}}^c = 925$ Hz. In addition to damping parameter $c_{\mathcal{H}}$ and to the 6 dispersion hyperparameters, the ML-SROM is defined by the 6 filtering parameters, $(d_{\mathcal{H}}\,, \nu_{\mathcal{H}})$, $(d_{\mathcal{M}}\,, \nu_{\mathcal{M}})$, and $(d_{\mathcal{L}}\,, \nu_{\mathcal{L}})$.

5.3.2.2 Construction of a first version of the ML-NROM

First, from the numerical exploration of parameters $(d_{\mathcal{H}}\,, \nu_{\mathcal{H}})$ in a deterministic framework as described in latter section 5.3.1.1 (see also Fig. 5.16), a first version of the scale-t ROM, given by $d_{\mathcal{H}} = 20$ and $\nu_{\mathcal{H}} = 3{,}900$, is chosen. Then, successive numerical explorations of the parameters $(d_{\mathcal{M}}\,, \nu_{\mathcal{M}})$ and $(d_{\mathcal{L}}\,, \nu_{\mathcal{L}})$ are carried out in a similar manner by using scale-$\mathcal{LM}$ and scale-$\mathcal{L}$ ROMs (these ROMs were introduced in Section 4.2.3). These explorations yield $(d_{\mathcal{M}} = 12, \nu_{\mathcal{M}} = 800)$ and $(d_{\mathcal{L}} = 6, \nu_{\mathcal{L}} = 275)$. It should be noted that the coupling with the dispersion hyperparameters to be identified is, at this step, not taken into account.

5.3.2.3 Sensitivity analysis of the ML-SROM with respect to the dispersion hyperparameters

A sensitivity analysis of the ML-SROM associated with latter definition of the ML-NROM is carried out. It shows that for a given scale $\mathcal{S}$ equal to $\mathcal{L}$, $\mathcal{M}$ or $\mathcal{H}$, the influence of parameters $\delta_M^{\mathcal{S}}$ and $\delta_K^{\mathcal{S}}$ (associated with the statistical dispersion of the reduced mass and stiffness matrices) is roughly identical. Therefore, only 3 dispersion hyperparameters $\delta^{\mathcal{L}}$, $\delta^{\mathcal{M}}$, and $\delta^{\mathcal{H}}$ have to be identified: $\delta^{\mathcal{L}} = \delta_K^{\mathcal{L}} = \delta_M^{\mathcal{L}}$, $\delta^{\mathcal{M}} = \delta_K^{\mathcal{M}} = \delta_M^{\mathcal{M}}$, and $\delta^{\mathcal{H}} = \delta_K^{\mathcal{H}} = \delta_M^{\mathcal{H}}$.

5.3.2.4 First identification of the hyperparameters of the ML-SROM using a coarse $3D$ grid

A first identification is carried out using a coarse $\delta^{\mathcal{L}} \times \delta^{\mathcal{M}} \times \delta^{\mathcal{H}}$ grid, for which the boundaries are deduced from the previous sensitivity analysis. The $3D$ grid is constituted of 540 sampling points, defined by the cartesian product of the following sets $\boldsymbol{\delta}^{\mathcal{L}} \times \boldsymbol{\delta}^{\mathcal{M}} \times \boldsymbol{\delta}^{\mathcal{H}}$:

$$\begin{aligned} \boldsymbol{\delta}^{\mathcal{L}} &= (\,0.15\,,\,0.20\,,\,0.25\,,\,0.30\,,\,0.35\,,\,0.40\,,\,0.45\,,\,0.50\,,\,0.55\,,\,0.60\,)\,, \\ \boldsymbol{\delta}^{\mathcal{M}} &= (\,0.10\,,\,0.15\,,\,0.20\,,\,0.25\,,\,0.30\,,\,0.35\,,\,0.40\,,\,0.45\,,\,0.50\,)\,, \\ \boldsymbol{\delta}^{\mathcal{H}} &= (\,0.05\,,\,0.07\,,\,0.09\,,\,0.11\,,\,0.13\,,\,0.15\,)\,. \end{aligned} \tag{5.9}$$

As for the C-SROM, only $n_{\text{sim}} = 40$ Monte-Carlo simulations are used for estimating the objective function J_s associated with each sampling point. The optimal point found is $\delta^{\mathcal{L}} = 0.25\,,\ \delta^{\mathcal{M}} = 0.25\,,\ \delta^{\mathcal{H}} = 0.11\,,$ which is sufficiently far from the grid boundaries. Concerning the computational cost, similarly to the C-SROM, for each independent realization of random matrices $[\mathbf{M}]$ and $[\mathbf{K}]$ of Eq. (4.40), the matrix equation is diagonalized, by solving an eigenvalue problem of dimension $n_t\,.$ In addition, damping parameter $c_{\mathcal{H}}$ is identified for each sampling point. It should be noted that, compared to dimension $n = 8{,}450$ of the classical ROM, the final dimension $n_t = 4{,}232$ of the identified multilevel ROM allows for obtaining a non-negligible computational time gain of about a factor of ten (the complexity of the algorithms for computing all the eigenvalues and eigenvectors of a full matrix being approximately cubic).

5.3.2.5 Precise and simultaneous identification of the filtering parameters of the HF band and of the dispersion hyperparameter of the HF band

We are now interested in adjusting the choice for parameters $(d_{\mathcal{H}}\,,\nu_{\mathcal{H}})$ that induce the construction of subspace $\mathcal{S}_t$ of the ML-NROM of dimension n_t. Supposing these filtering parameters are sufficiently big, the choice of their values does not influence the random FRFs in the LF and MF bands (which have already converged with respect to them). The influence of parameter $\delta^{\mathcal{M}}$ (and especially of parameter $\delta^{\mathcal{L}}$) is not preponderant for the random response in the HF band. Consequently, fixing the values of $\delta^{\mathcal{L}}$ and $\delta^{\mathcal{M}}$ that have been identified in the coarse $3D$ grid, the ML-SROM is identified with respect to filtering parameters $(d_{\mathcal{H}}\,,\nu_{\mathcal{H}})$ and to dispersion hyperparameter $\delta^{\mathcal{H}}$, simultaneously. It should be noted that the identification does not consist, at this step, in picking the parameters that maximize the objective function $J_s\,.$ Rather, it consists in finding a set of parameters

for which J_s is close to its maximum but under the constraint of a reasonably small dimension n_t for the ROM. It should be recalled that J_s is only estimated using $n_{\text{sim}} = 40$ realizations and, in addition, the identification is subjected to approximations. In such a context, between ML-SROMs with similar values for J_s, one should pick the ML-SROM for which the dimension n_t is the smallest, since, anyway, the value of J_s suffers from approximations. This step completed, the parameters that are chosen are the following: $d_{\mathcal{H}} = 34$, $\nu_{\mathcal{H}} = 4{,}250$, and $\delta^{\mathcal{H}} = 0.078$.

5.3.2.6 Final stage for the global identification of the ML-SROM

Parameters $(d_{\mathcal{L}}\,, \nu_{\mathcal{L}})\,, (d_{\mathcal{M}}\,, \nu_{\mathcal{M}})\,, \delta^{\mathcal{L}}\,,$ and $\delta^{\mathcal{M}}$ remain to be identified. In order to avoid a 6-dimensional costly optimization problem, the 4 filtering parameters are left unchanged. It should be noted that these parameters control the overlap of subspaces $\mathcal{S}_{\mathcal{L}}\,, \mathcal{S}_{\mathcal{M}}\,,$ and $\mathcal{S}_{\mathcal{H}}$ of the multilevel ROM, associated with LF-, MF-, and HF-type displacements. Also, if parameters $(d_{\mathcal{L}}\,, \nu_{\mathcal{L}})$ and $(d_{\mathcal{M}}\,, \nu_{\mathcal{M}})$ were to tend towards infinity, there would be no overlap of subspaces $\mathcal{S}_{\mathcal{L}}\,, \mathcal{S}_{\mathcal{M}}\,,$ and $\mathcal{S}_{\mathcal{H}}\,.$ Qualitatively, subspace $\mathcal{S}_{\mathcal{L}}$ is supposed to be composed of long-wavelength global displacements, without the numerous local displacements. Therefore, based on these physical considerations, it is more suitable to force the values of filtering parameters $(d_{\mathcal{L}}\,, \nu_{\mathcal{L}})$ and $(d_{\mathcal{M}}\,, \nu_{\mathcal{M}})$ outside the global stochastic identification problem of the ML-SROM. Then, parameters $\delta^{\mathcal{L}}$ and $\delta^{\mathcal{M}}$ of the ML-SROM are identified by estimating objective function J_s over the sampling points of a given $2D$ grid, the other parameters being fixed. After this final stage, the identified values are $\delta^{\mathcal{L}} = 0.4$ and $\delta^{\mathcal{M}} = 0.22$. For the identified ML-SROM, the values of objective functions $J_{s,1}$ and $J_{s,2}$ evaluated by using, again, $n_{\text{sim}} = 10{,}000$ realizations, are $J_{s,1} = 0.65$ and $J_{s,2} = 0.64$, hence $J_s = 0.65$, which constitutes a non-negligible improvement with respect to the C-SROM.

5.3.2.7 Confidence regions of the random FRFs and experimental comparisons

The confidence regions obtained using the identified ML-SROM are estimated using $n_{\text{sim}} = 10{,}000$ realizations and are plotted in Figs. 5.20 and 5.21. It can be seen that, despite the discrepancies of the ML-NROM (which are similar to those of the C-NROM), the ML-SROM is able to represent most of the experimental FRFs (unlike the C-SROM). This improvement is due to the increased flexibility of the ML-SROM with respect to the C-SROM, particularly concerning the capability to adapt the level of uncertainties to each frequency band. It should be

noted that, in general, on one hand the variability of the real system is low in the LF band and that, on the other hand, the robustness of the computational models is better in this band. In the present case, in the LF and MF bands, the modeling errors are more important than the level of variabilities of the real system, hence the large confidence intervals provided by the ML-SROM in these bands.

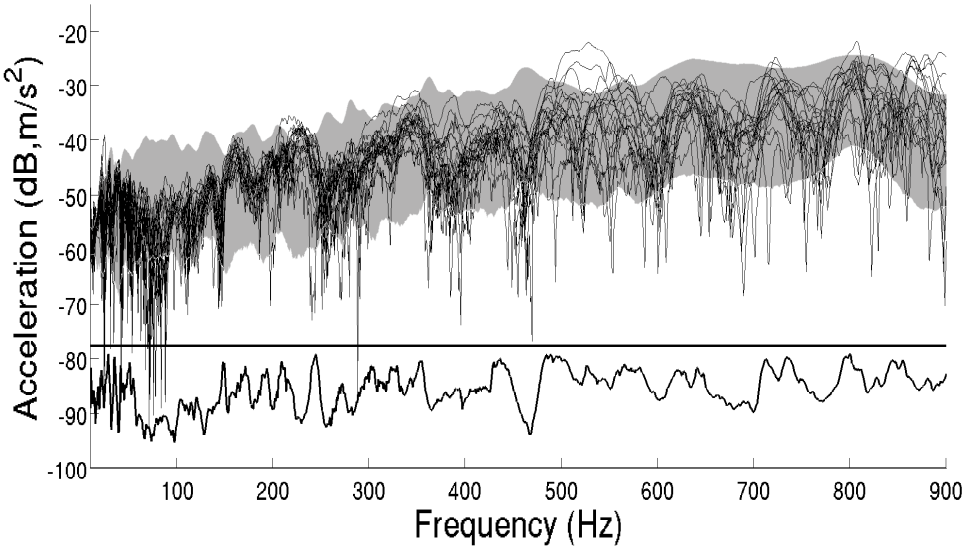

Figure 5.20: Observation 1: experimental FRF measurements performed on the PSA cars of the same type [119] (black lines), random FRF using the identified ML-SROM (gray region), and OVL function (black line underneath).

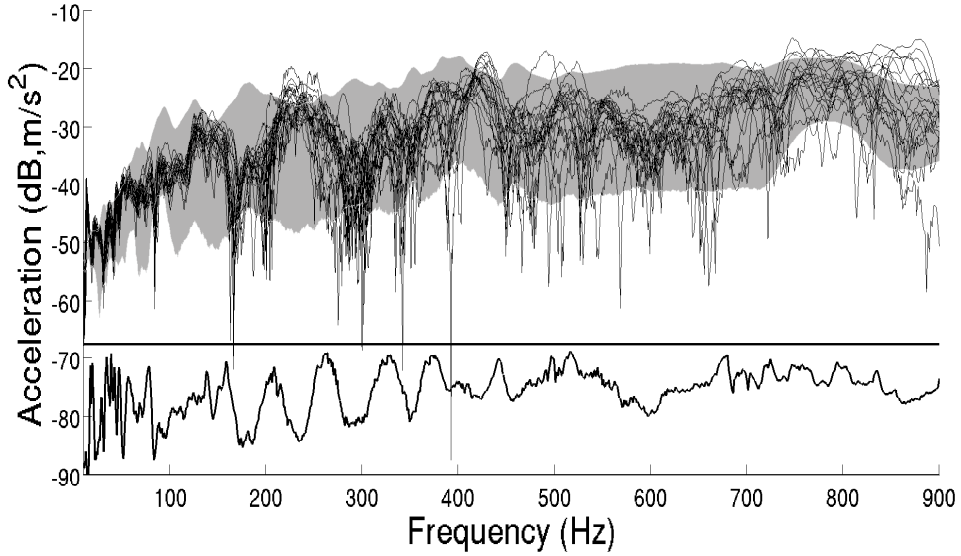

Figure 5.21: Observation 2: experimental FRF measurements performed on the PSA cars of the same type [119] (black lines), random FRF using the identified ML-SROM (gray region), and OVL function (black line underneath).

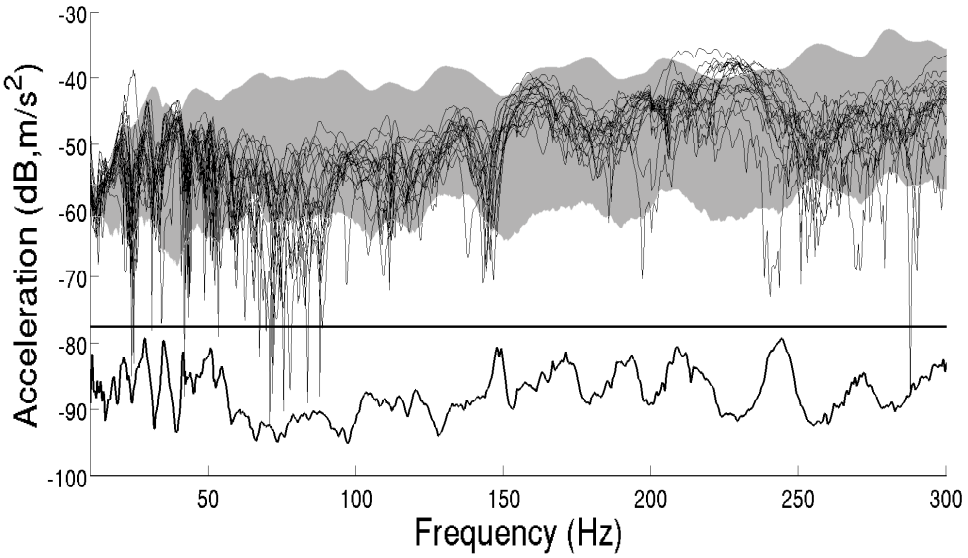

Figure 5.22: Observation 1, zoom into band $\mathcal{B}_{\mathcal{L}} \cup \mathcal{B}_{\mathcal{M}}$: experimental FRF measurements performed on the PSA cars of the same type [119] (black lines), random FRF using the identified ML-SROM (gray region), and OVL function (black line underneath).

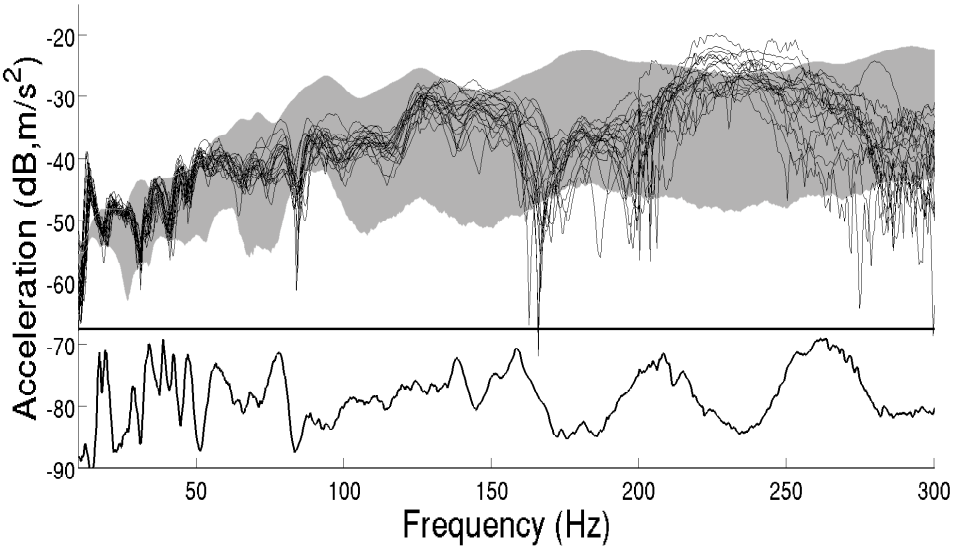

Figure 5.23: Observation 2, zoom into band $\mathcal{B}_{\mathcal{L}} \cup \mathcal{B}_{\mathcal{M}}$: experimental FRF measurements performed on the PSA cars of the same type [119] (black lines), random FRF using the identified ML-SROM (gray region), and OVL function (black line underneath).

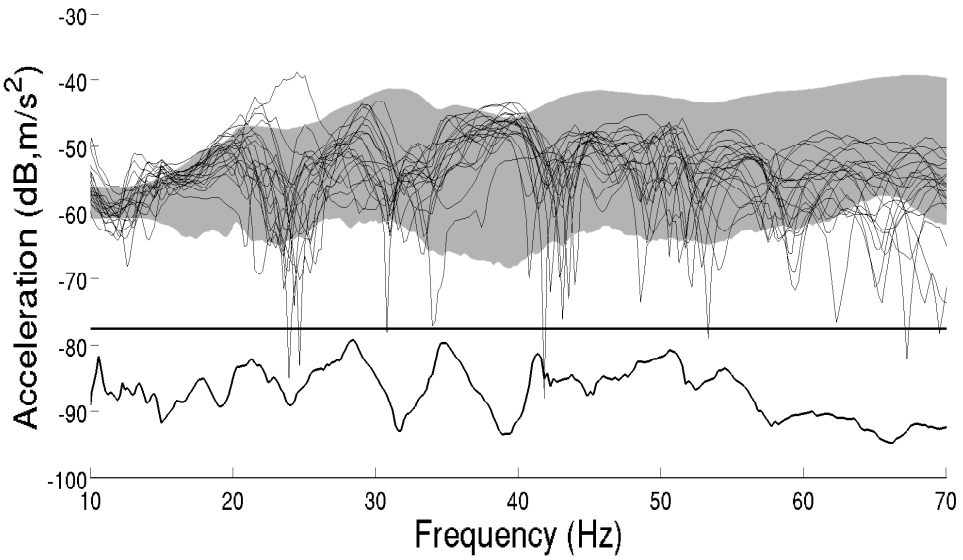

Figure 5.24: Observation 1, zoom into band $\mathcal{B}_{\mathcal{L}}$: experimental FRF measurements performed on the PSA cars of the same type [119] (black lines), random FRF using the identified ML-SROM (gray region), and OVL function (black line underneath).

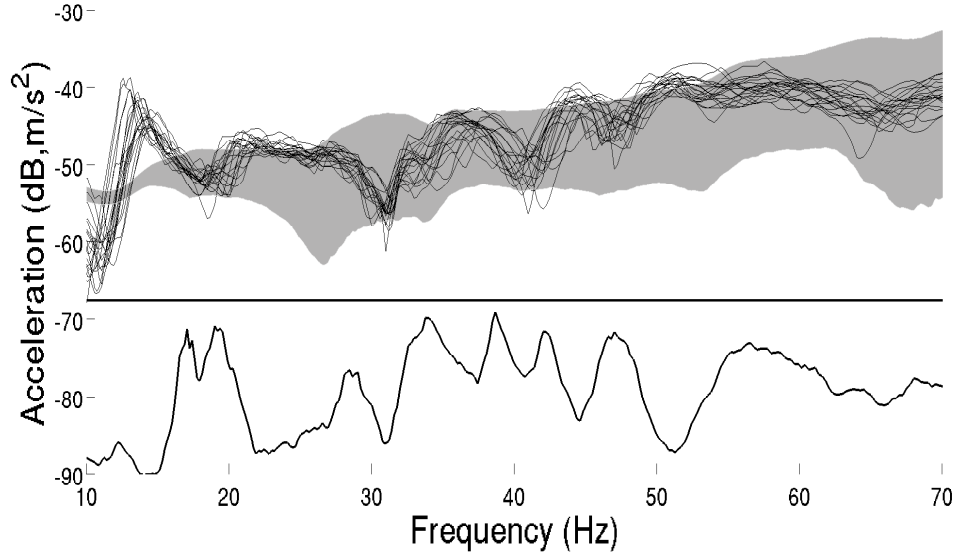

Figure 5.25: Observation 2, zoom into band $\mathcal{B}_{\mathcal{L}}$: experimental FRF measurements performed on the PSA cars of the same type [119] (black lines), random FRF using the identified ML-SROM (gray region), and OVL function (black line underneath).

Figures 5.22 and 5.23 display a zoom of Figs. 5.20 and 5.21 into band $\mathcal{B}_{\mathcal{L}} \cup \mathcal{B}_{\mathcal{M}}$ and Figs. 5.24 and 5.25 display a zoom of Figs. 5.20 and 5.21 into band $\mathcal{B}_{\mathcal{L}}$. It can be seen that the OVL function confirms the improved prediction of the ML-SROM in the LF and MF bands.

5.4 Complementary results

5.4.1 Deterministic analysis of the contribution of each of the ROBs

In order to put into evidence the individual contribution of each ROB, $[\Phi^{\mathcal{L}}]$, $[\Phi^{\mathcal{M}}]$ or $[\Phi^{\mathcal{H}}]$, the deterministic FRFs are calculated by using either scale-$\mathcal{L}$, scale-$\mathcal{M}$, or scale-$\mathcal{H}$ ROM (of dimensions $n_{\mathcal{L}} = 81$, $n_{\mathcal{M}} = 414$, and $n_{\mathcal{H}} = 3{,}737$, respectively). Figures 5.26 and 5.27 present the FRFs (modulus in log scale of the accelerations of observations 1 and 2) given by these three ROMs, in addition to the experimental measurements. For comparison, three ROMs are introduced, for which the associated ROBs are (i) the first 159 elastic modes, (ii) the next 1,202 elastic modes, and (iii) the following 7,089 elastic modes. The same FRFs are computed by using these ROMs and are depicted in Figs. 5.28 and 5.29. It can be seen that, in contrast to the FRFs given by the different ROBs of elastic modes, the ROBs constituted of the constructed LF-, MF-, and HF-type displacements yield FRFs for which the dynamical contents overlap in frequency. It should be noted that the scale-$\mathcal{L}$ ROM does not contribute beyond $f^c_{\mathcal{L}} = 70$ Hz, neither does the scale-$\mathcal{M}$ ROM beyond $f^c_{\mathcal{M}} = 300$ Hz. This is explained by latter cutoff frequencies, which have been used for constructing these ROMs.

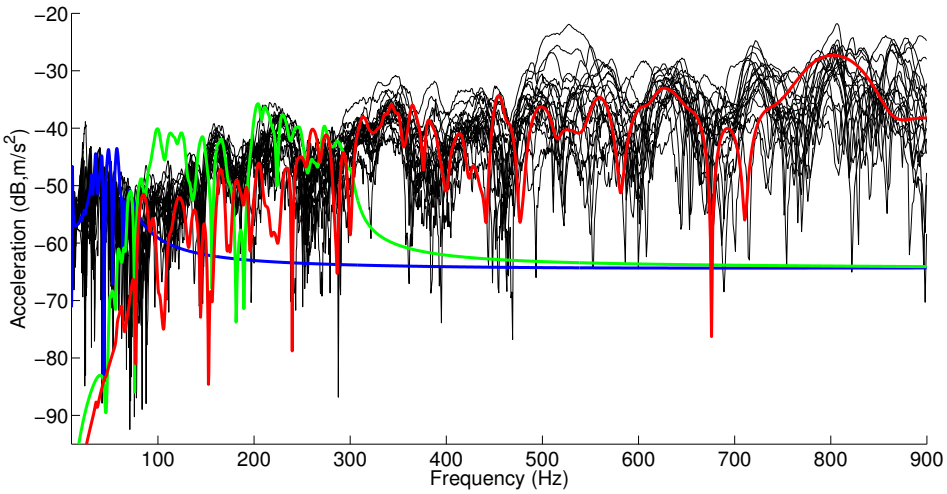

Figure 5.26: Observation 1: experimental FRF measurements performed on the PSA cars of the same type [119] (black lines), deterministic FRF using the scale-$\mathcal{L}$ ROM (blue line), deterministic FRF using the scale-$\mathcal{M}$ ROM (green line), and deterministic FRF using the scale-$\mathcal{H}$ ROM (red line).

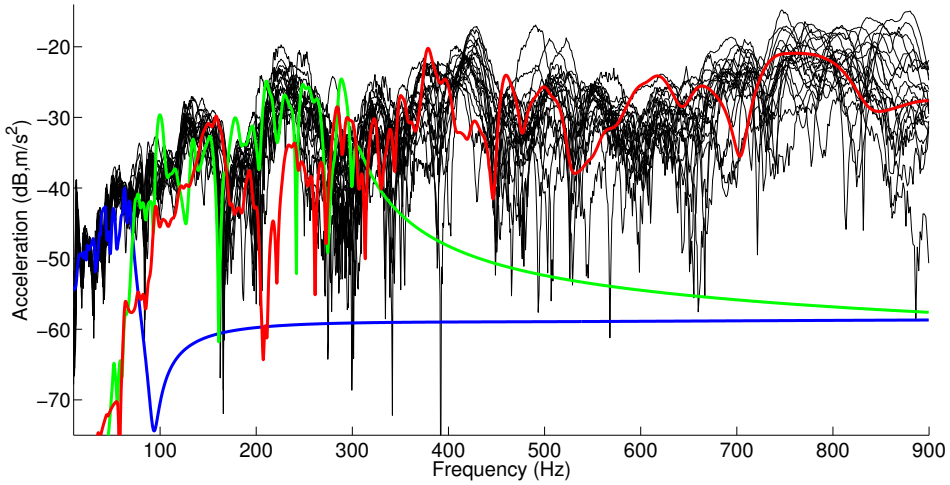

Figure 5.27: Observation 2: experimental FRF measurements performed on the PSA cars of the same type [119] (black lines), deterministic FRF using the scale-$\mathcal{L}$ ROM (blue line), deterministic FRF using the scale-$\mathcal{M}$ ROM (green line), and deterministic FRF using the scale-$\mathcal{H}$ ROM (red line).

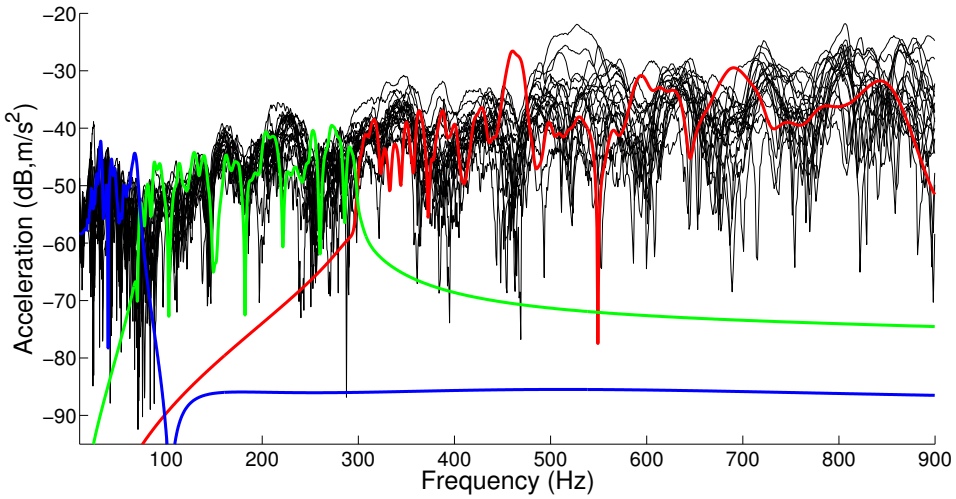

Figure 5.28: Observation 1: experimental FRF measurements performed on the PSA cars of the same type [119] (black lines), deterministic FRF using the 159 LF elastic modes (blue line), deterministic FRF using the 1,202 MF elastic modes (green line), and deterministic FRF using the 7,089 HF elastic modes (red line).

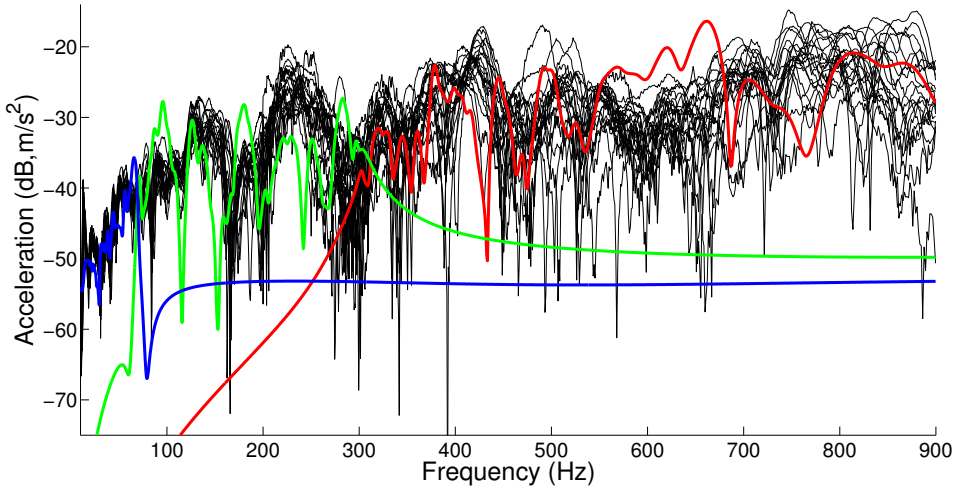

Figure 5.29: Observation 2: experimental FRF measurements performed on the PSA cars of the same type [119] (black lines), deterministic FRF using the 159 LF elastic modes (blue line), deterministic FRF using the 1,202 MF elastic modes (green line), and deterministic FRF using the 7,089 HF elastic modes (red line).

5.4.2 Stochastic sensitivity analysis

5.4.2.1 Proposed ML-SROM

A sensitivity analysis of the ML-SROM with respect to the dispersion hyperparameters is presented. Using the identified parameters of the ML-SROM and successively setting to zero 2 dispersion hyperparameters out of the 3 hyperparameters $\delta^{\mathcal{L}}$, $\delta^{\mathcal{M}}$, $\delta^{\mathcal{H}}$ allow for quantifying the individual contribution of each scale $\mathcal{L}$, $\mathcal{M}$, $\mathcal{H}$ of displacements in the random responses. The confidence regions obtained using the proposed ML-SROM are estimated using $n_{\text{sim}} = 10{,}000$ Monte-Carlo realizations. The confidence regions are obtained by using the identified ML-SROM and by setting, successively, $\delta^{\mathcal{M}} = \delta^{\mathcal{H}} = 0$ (see Fig. 5.30 for observation 1 and Fig. 5.33 for observation 2), $\delta^{\mathcal{L}} = \delta^{\mathcal{H}} = 0$ (see Fig. 5.31 for observation 1 and Fig. 5.34 for observation 2), and $\delta^{\mathcal{L}} = \delta^{\mathcal{M}} = 0$ (see Fig. 5.32 for observation 1 and Fig. 5.35 for observation 2). In each figure, the vertical lines indicate the boundaries between the LF, MF, and HF bands. Figures 5.32 and 5.35 show, for instance, that adding uncertainties to the HF-type displacements yields the presence of uncertainties in the LF and MF bands. It is explained by the fact that, since $d_{\mathcal{H}}$ is greater than $d_{\mathcal{M}}$, some HF-type displacements are likely to be present in the LF and MF bands. However, despite the absence of MF-type displacements in the HF band (it is recalled that $f^c_{\mathcal{M}} = 300$ for the construction

given in either Eq. (4.4) or (4.20)), Figs. 5.31 and 5.34 show, for instance, that adding uncertainties to the MF-type displacements yields the presence of uncertainties in the HF band. This is due to the fact that the LF-, MF-, and HF-type displacements are not orthogonal with respect to the stiffness matrix.

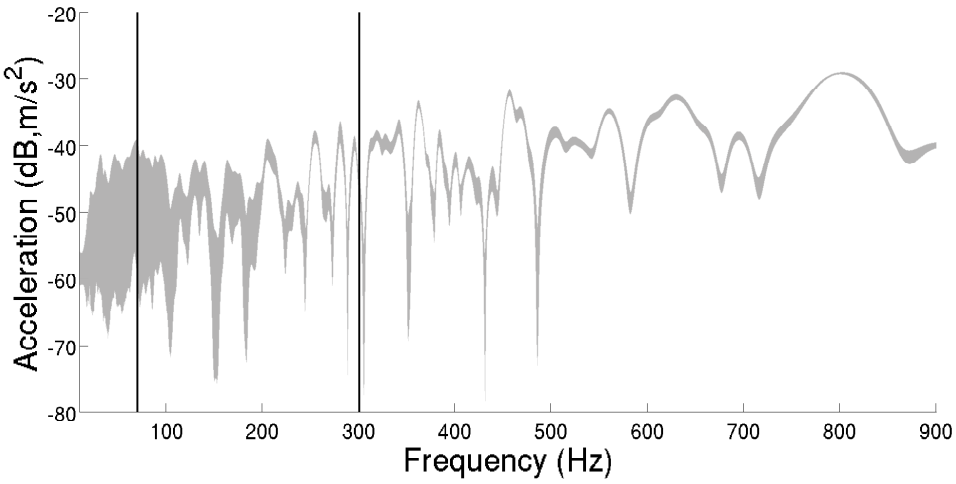

Figure 5.30: Observation 1: random FRF using the identified ML-SROM but for which $\delta^{\mathcal{M}} = \delta^{\mathcal{H}} = 0$ is imposed.

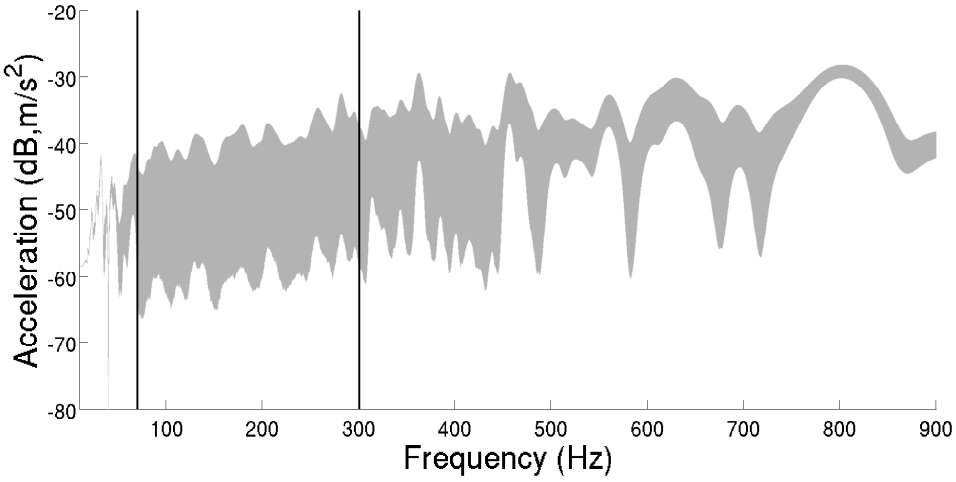

Figure 5.31: Observation 1: random FRF using the identified ML-SROM but for which $\delta^{\mathcal{L}} = \delta^{\mathcal{H}} = 0$ is imposed.

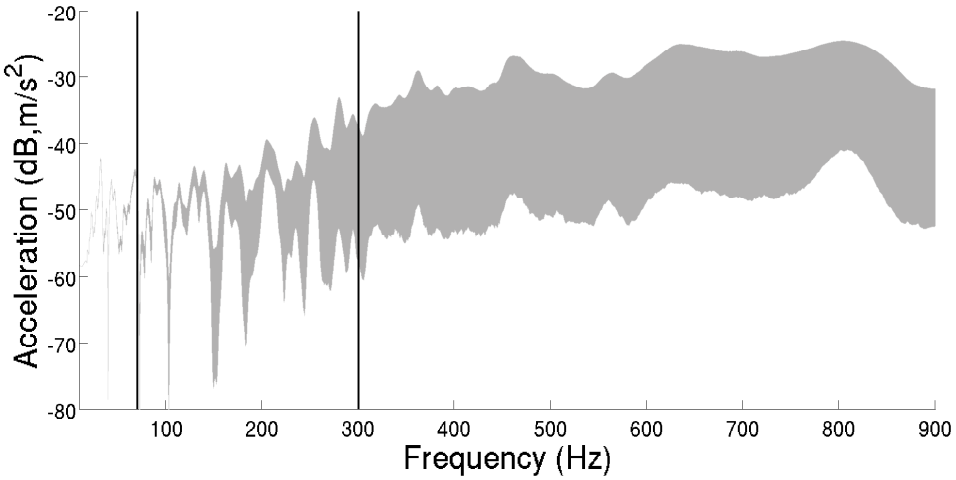

Figure 5.32: Observation 1: random FRF using the identified ML-SROM but for which $\delta^{\mathcal{L}} = \delta^{\mathcal{M}} = 0$ is imposed.

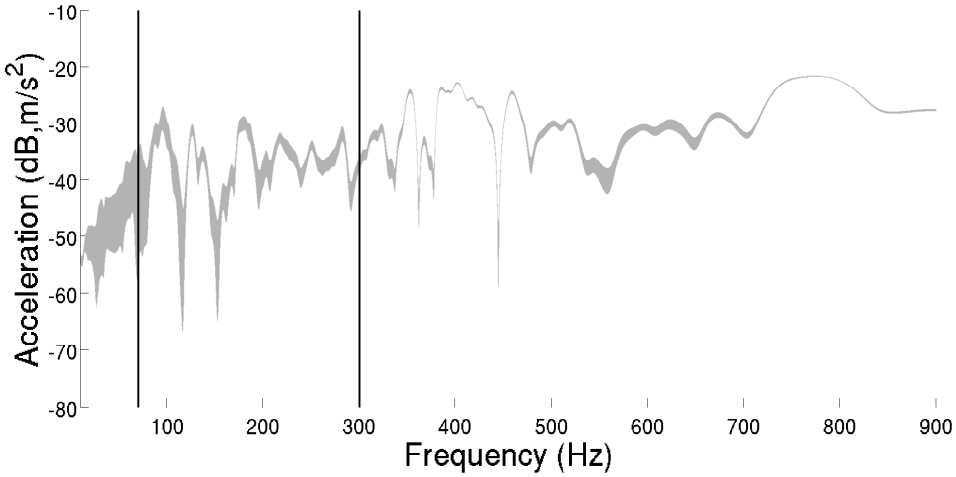

Figure 5.33: Observation 2: random FRF using the identified ML-SROM but for which $\delta^{\mathcal{M}} = \delta^{\mathcal{H}} = 0$ is imposed.

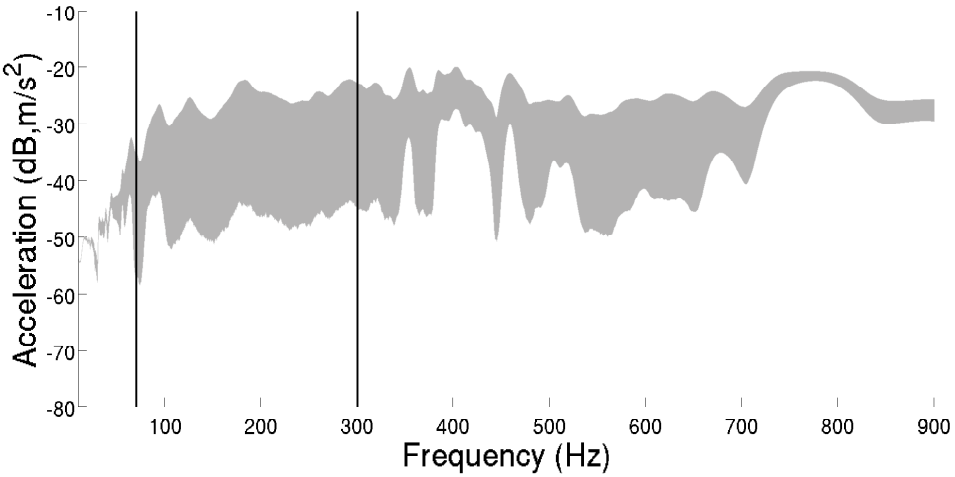

Figure 5.34: Observation 2: random FRF using the identified ML-SROM but for which $\delta^{\mathcal{L}} = \delta^{\mathcal{H}} = 0$ is imposed.

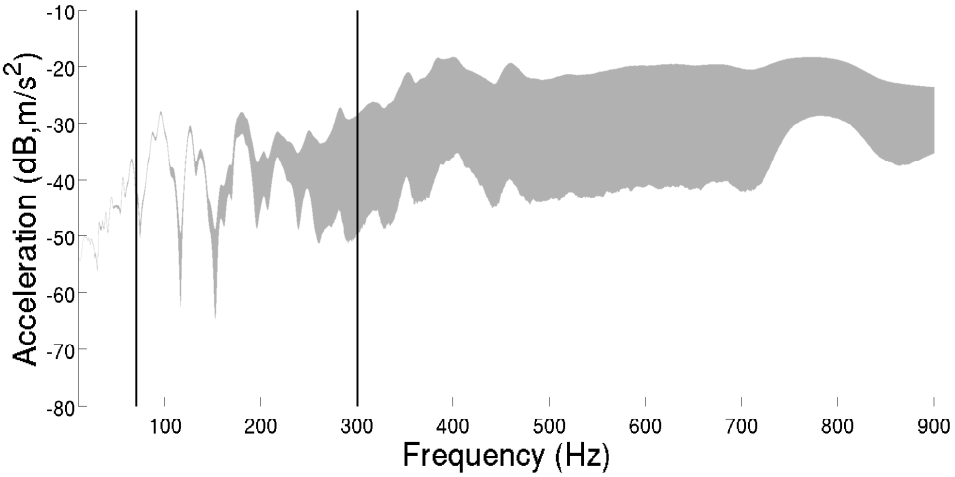

Figure 5.35: Observation 2: random FRF using the identified ML-SROM but for which $\delta^{\mathcal{L}} = \delta^{\mathcal{M}} = 0$ is imposed.

5.4.2.2 Naive ML-SROM

A sensitivity analysis is carried out by using a naive ML-SROM that is defined as follows. The vector basis associated with subspace $\mathcal{S}_{\mathcal{L}}$ is given by the 159 elastic modes present in frequency band $\mathcal{B}_{\mathcal{L}}$, the vector basis associated with subspace $\mathcal{S}_{\mathcal{M}}$ is given by the 1,202 elastic modes present in frequency band $\mathcal{B}_{\mathcal{M}}$, and the vector basis associated with subspace $\mathcal{S}_{\mathcal{H}}$ is given by the next 7,099 elastic modes. It should be noted that this ML-SROM corresponds to choosing filtering parameters $(d_{\mathcal{L}}\,,\nu_{\mathcal{L}})$, $(d_{\mathcal{M}}\,,\nu_{\mathcal{M}})$, and $(d_{\mathcal{H}}\,,\nu_{\mathcal{H}})$ as going to infinity (no filtering). The sensitivity analysis of this stochastic ROM is carried out using the same set of combinations of the dispersion hyperparameters as in the previous section. The confidence regions are estimated using $n_{\text{sim}} = 10{,}000$ Monte-Carlo realizations. Figures 5.36, 5.37, and 5.38 depict the confidence regions obtained for observation 1 and Figs. 5.39, 5.40, and 5.41 depict the confidence regions obtained for observation 2 . It can be seen that, for this naive ML-SROM, the introduction of uncertainties for one given vector basis induces the presence of uncertainties for the corresponding frequency band, while practically none elsewhere. This stochastic ROM is thus not well adapted for modeling uncertainties of complex dynamical systems for which the LF, MF, and HF vibration regimes overlap.

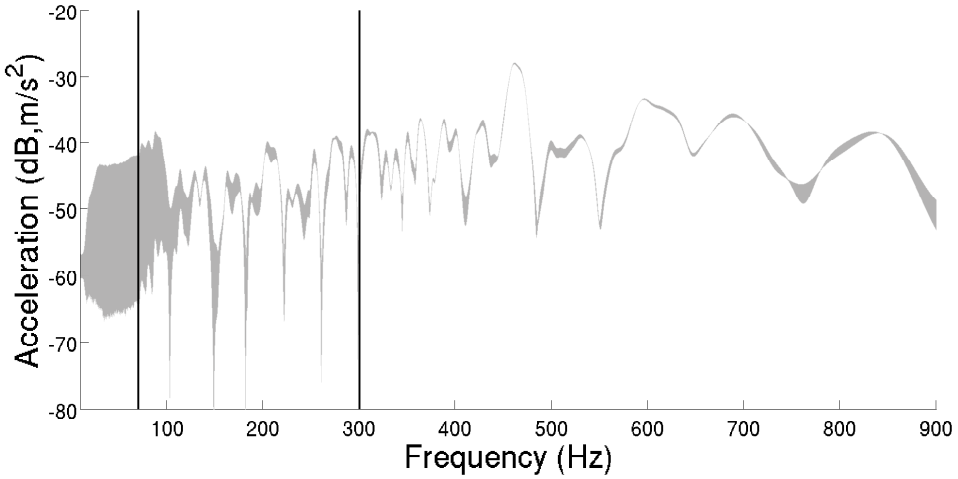

Figure 5.36: Observation 1: random FRF using the naive ML-SROM for which $\delta^{\mathcal{M}} = \delta^{\mathcal{H}} = 0$ is imposed.

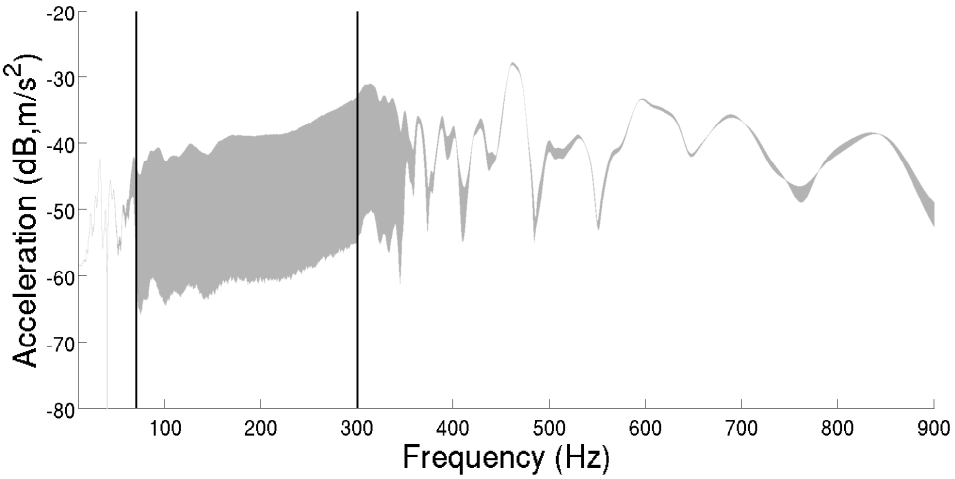

Figure 5.37: Observation 1: random FRF using the naive ML-SROM for which $\delta^{\mathcal{L}} = \delta^{\mathcal{H}} = 0$ is imposed.

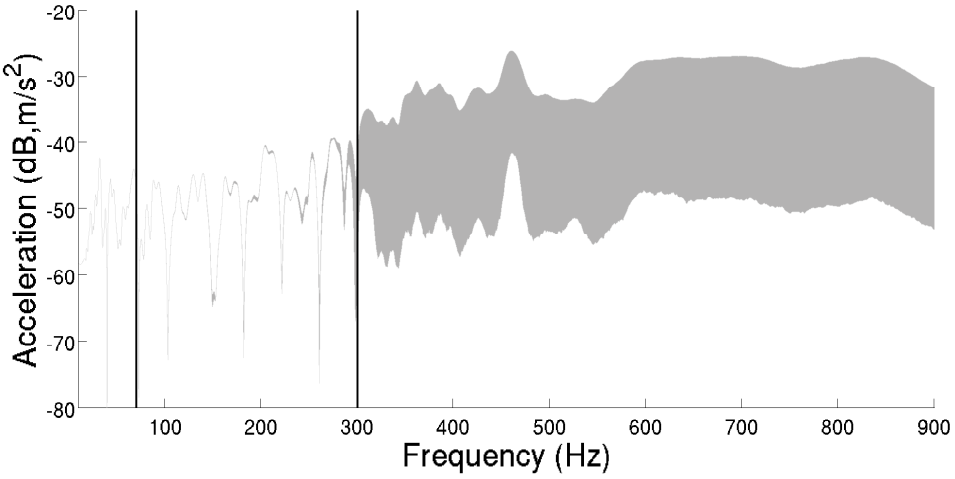

Figure 5.38: Observation 1: random FRF using the naive ML-SROM for which $\delta^{\mathcal{L}} = \delta^{\mathcal{M}} = 0$ is imposed.

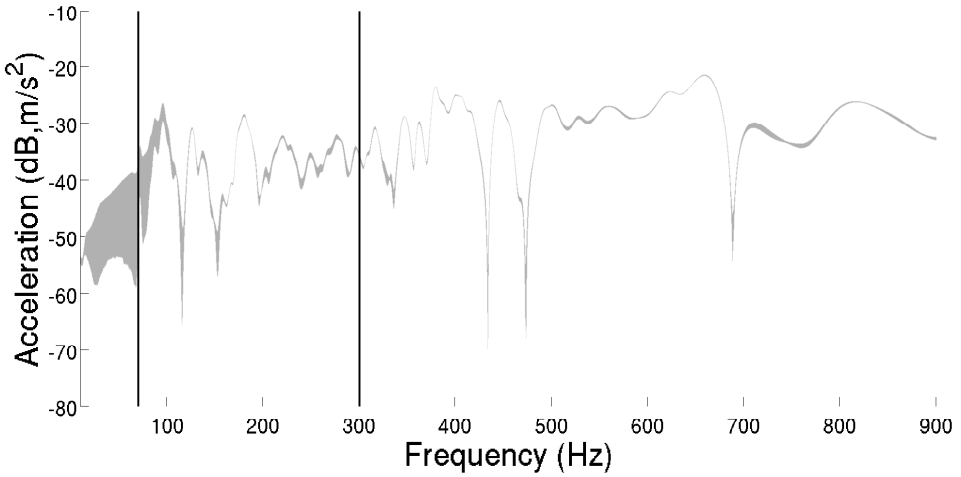

Figure 5.39: Observation 2: random FRF using the naive ML-SROM for which $\delta^{\mathcal{M}} = \delta^{\mathcal{H}} = 0$ is imposed.

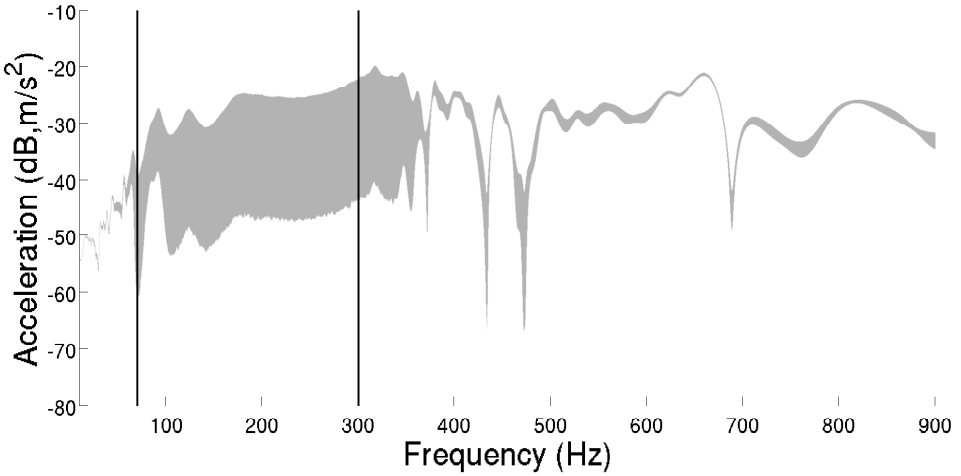

Figure 5.40: Observation 2: random FRF using the naive ML-SROM for which $\delta^{\mathcal{L}} = \delta^{\mathcal{H}} = 0$ is imposed.

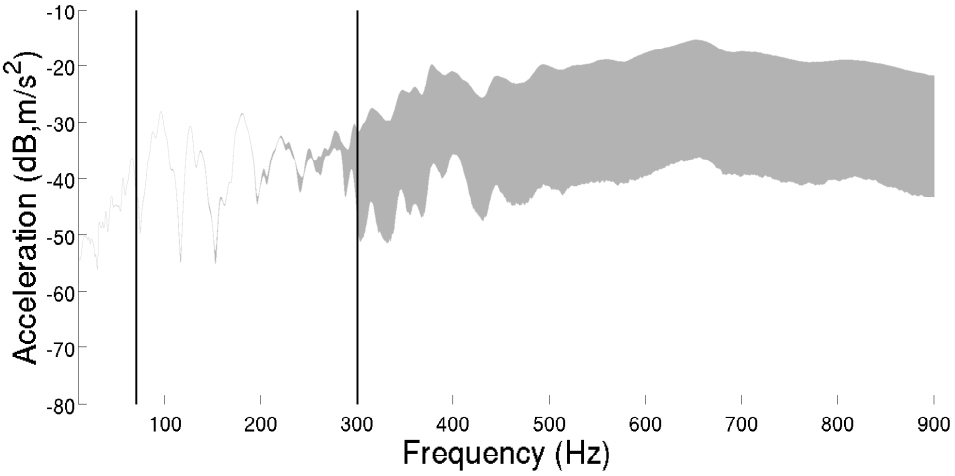

Figure 5.41: Observation 2: random FRF using the naive ML-SROM for which $\delta^{\mathcal{L}} = \delta^{\mathcal{M}} = 0$ is imposed.

Chapter 6

Conclusions and future prospects

Conclusions

A general method has been developed for the construction of a multilevel stochastic ROM devoted to the robust dynamical analysis of complex systems over a broad frequency band. The complex systems considered are constituted of several structural scales which, for instance, induce the presence in the low-frequency range of numerous short-wavelength local displacements in addition to the usual long-wavelength global displacements.

The proposed multilevel ROM is based on the construction of three orthogonal ROBs whose displacements are either LF-, MF-, or HF-type displacements, associated with the overlapping LF, MF, and HF vibration regimes. The construction of these ROBs relies on a filtering strategy that is based on the introduction of global shape functions for the kinetic energy (in contrast to the local shape functions of the finite elements). In parallel to the fact that the local displacements are more sensitive to uncertainties than the global displacements, implementing the nonparametric probabilistic approach of uncertainties within the multilevel nominal ROM, each ROB of the obtained multilevel stochastic ROM can be endowed with a specific level of uncertainties through the values given to the dedicated dispersion hyperparameters.

The numerical analysis and the algorithms have carefully been developed in order to deal with large-scale finite element models. The complete methodology has been implemented in a dedicated software (written in MATLAB language), for which the inputs are the eigenfrequencies, the elastic modes, and a lumped mass matrix of the finite element model, which are exported from any commercial

software. Consequently, the approach proposed is nonintrusive with respect to commercial software.

Several applications have been carried out in order to work out the method, the numerical analysis, and the algorithms. All these applications are published in the papers by the author and referenced in the introduction. These applications are not reproduced in the thesis, in order not to complicate the presentation. These applications concern a heterogeneous plate with two structural levels, a heterogeneous plate with three structural levels, and a car body structure with a large-scale finite element model (different from the one presented in the thesis).

The experimental validation has been given and the capability of the methodology proposed has been demonstrated, for a multilevel stochastic ROM constructed for a complex dynamical system consisting of an automobile, which has been identified with respect to experimental measurements, and which allows for obtaining a decreased dimension as well as an improved prediction with respect to a classical stochastic ROM.

Future prospects

A first development would consist in extending the current framework devoted to the filtering between the global and the local displacements by introducing an adaptive reduced kinematics for the kinetic energy.

A second point would be to test the capability of the methodology for other complex structures and also for vibroacoustic systems.

A third point would consist in substituting the nonparametric probabilistic approach based on the random matrix theory by the nonparametric probabilistic approach recently proposed [118] and based on the use of a stochastic ROB for constructing the stochastic ROM.

Bibliography

[1] Bathe KJ (1996) Finite element procedures. Prentice Hall, Upper Saddle River, New Jersey.

[2] Hughes TJR (2000) The Finite Element Method: Linear Static and Dynamic Finite Element Analysis. Dover Publications, New York.

[3] Zienkiewicz OC, Taylor RL (2000) The Finite Element Method, 5th ed. Butterworth-Heinemann, Oxford.

[4] Soize C (1982) Medium frequency linear vibrations of anisotropic elastic structures. La Recherche Aérospatiale (English edition) 5:65–87.

[5] Bathe KJ, Wilson EL (1976) Numerical methods in the finite element method. Englewood Cliffs, New Jersey: Prentice-Hall.

[6] Meirovitch L (1990) Dynamics and Control of Structures. Wiley, New York.

[7] Argyris J, Mlejnek HP (1991) Dynamics of Structures. North-Holland, Amsterdam.

[8] Geradin M, Rixen D (1997) Mechanical Vibrations, Second edition: Theory and Applications to Structural Dynamics. Wiley, Chichester.

[9] Ohayon R, Soize C (1998) Structural acoustics and vibration. Academic Press, San Diego.

[10] Craig RR, Kurdila AJ (2006) Fundamentals of Structural Dynamics. Wiley, 2nd Edition, John Wiley and Sons, Hoboken.

[11] Bathe KJ (2013) The subspace iteration method - revisited. Comp Struct 126:177–183. doi:http://dx.doi.org/10.1016/j.compstruc.2012.06.002

[12] Casciati S, Faravelli L (2014) Quantity vs. quality in the model order reduction (MOR) of a linear dynamical system. Smart Struct Syste 13(1):99–109. doi:http://dx.doi.org/10.12989/sss.2014.13.1.099

[13] Rumpler R, Legay A, Deü JF (2011) Performance of a restrained-interface substructuring FE model for reduction of structural-acoustic problems with poroelastic damping. Comput Struct 89(23–24):2233–2248. doi:http://dx.doi.org/10.1016/j.compstruc.2011.08.012

[14] Rumpler R, Göransson P, Deü JF (2013) A residue-based mode selection and sorting procedure for efficient poroelastic modeling in acoustic finite element applications. J Acoust Soc Am 134(6):4730–4741. doi:http://dx.doi.org/10.1121/1.4824966

[15] Lyon RH, DeJong RG (1995) Theory and Application of Statistical Energy Analysis. Butterworths-Heimann, Boston.

[16] Langley RS, Bremner P (1999) A hybrid method for the vibration analysis of complex structural-acoustic systems. J Acoust Soc Am 105(3):1657–1671. doi:http://dx.doi.org/10.1121/1.426705

[17] LeBot A (2002) Energy transfer for high frequencies in built-up structures. J Sound Vib 250(2):247–275. doi:http://dx.doi.org/10.1006/jsvi.2001.3933

[18] Maxit L, Guyader JL (2003) Extension of SEA model to subsystems with non-uniform modal energy distribution. J Sound Vib 265(2):337–358. doi:http://dx.doi.org/10.1016/S0022-460X(02)01459-1

[19] Langley RS, Cotoni V (2004) Response variance prediction in the statistical energy analysis of built up systems. J Acoust Soc Am 115(2):706–718. doi:http://dx.doi.org/10.1121/1.1642621

[20] Langley RS (2007) On the diffuse field reciprocity relationship and vibrational energy variance in a random subsystem at high frequencies. J Acoust Soc Am 121(2):913–921. doi:http://dx.doi.org/10.1121/1.2409484

[21] Cotoni V, Langley R, Shorter P (2008) A statistical energy analysis subsystem formulation using finite element and periodic structure theory. J Sound Vib 318(4-5):1077–1108. doi:http://dx.doi.org/10.1016/j.jsv.2008.04.058

[22] Ragnarsson P, Pluymers B, Donders S, W. Desmet W (2010) Subcomponent modelling of input parameters for statistical energy analysis by using a wave-based boundary condition. J Sound Vib 329(1):96–108. doi:http://dx.doi.org/10.1016/j.jsv.2009.08.033

[23] Besset S, Ichchou MN, Jézéquel L (2010) A coupled BEM and energy flow method for mid-high frequency internal acoustic. J Comput Acoust 18(1):69–85. doi:http://dx.doi.org/10.1142/S0218396X10004073

[24] Cotoni V, Le Bot A, Jézéquel L (2002) High-frequency radiation of L-shaped plates by a local energy flow approach. J Sound Vib 250(3):431–444. doi:http://dx.doi.org/10.1006/jsvi.2001.3952

[25] Sui FS, Ichchou MN, Jézéquel L (2002) Prediction of vibroacoustics energy using a discretized transient local energy approach and comparison with TSEA. J Sound Vib 251(1):163–180. doi:http://dx.doi.org/10.1006/jsvi.2001.3786

[26] Morand HJP (1992) A modal hybridization method for vibroacoustic studies at medium frequencies. J Acoust Soc Am 92(4):2365–2366. doi:http://dx.doi.org/10.1121/1.404855

[27] Ladevèze P (1996) A new computational approach for structure vibrations in the medium frequency range. CR Acad Sci II B-Mec 322(12):849–856.

[28] Soize C (1998) Reduced models in the medium frequency range for general dissipative structural-dynamics systems. Eur J Mech A-Solid 17(4):657–685. doi:http://dx.doi.org/10.1016/S0997-7538(99)80027-8

[29] Ladevèze P, Arnaud L, Rouch P, Blanzé C (2001) The variational theory of complex rays for the calculation of medium-frequency vibrations. Eng Computation 18(1-2):193–214. doi:http://dx.doi.org/10.1108/02644400110365879

[30] Farhat C, Harari I, Hetmaniuk U (2003) A discontinuous Galerkin method with Lagrange multipliers for the solution of Helmholtz problems in the mid-frequency regime. Comput Method Appl M 192(11-12):1389–1419. doi:http://dx.doi.org/10.1016/S0045-7825(02)00646-1

[31] De Bel E, Villon P, Bouillard Ph (2005) Forced vibrations in the medium frequency range solved by a partition of unity method with local information. Int J Numer Meth Eng 62(9):1105–1126. doi:http://dx.doi.org/10.1002/nme.1202

[32] Ladevèze P, Chevreuil M (2005) A new computational method for transient dynamics including the low- and the medium-frequency ranges. Int J Numer Meth Eng 64(4):503–527. doi:http://dx.doi.org/10.1002/nme.1379

[33] Shorter PJ, Langley RS (2005) Vibro-acoustic analysis of complex systems. J Sound Vib 288(3):669–699. doi:http://dx.doi.org/10.1016/j.jsv.2005.07.010

[34] Zhang L, Tezaur R, Farhat C (2006) The discontinuous enrichment method for elastic wave propagation in the medium-frequency regime. Int J Numer Meth Eng 66(13):2086–2114. doi:http://dx.doi.org/10.1002/nme.1619

[35] Ji L, Mace BR, Pinnington RJ (2006) A mode-based approach for the mid-frequency vibration analysis of coupled long- and short-wavelength structures. J Sound Vib 289(1-2):148–170. doi:http://dx.doi.org/10.1016/j.jsv.2005.02.003

[36] Soize C (1993) A model and numerical method in the medium frequency range for vibroacoustic predictions using the theory of structural fuzzy. J Acoust Soc Am 94:849–865. doi:http://dx.doi.org/10.1121/1.408186

[37] Sarkar A, Ghanem R (2002) Mid-frequency structural dynamics with parameter uncertainty. Comput Method Appl M 191(47-48):5499–5513. doi:http://dx.doi.org/10.1016/S0045-7825(02)00465-6

[38] Gagliardini L, Houillon L, Borello G, Petrinelli L (2003) Virtual SEA: Mid-Frequency Structure-Borne Noise Modeling Based on Finite Element Analysis. In: Noise & Vibration Conference, Traverse City, MI, USA, May 5-8, Paper 2003-01-1555, 22–28. SAE International, Troy, MI, USA.

[39] Ghanem R, Sarkar A (2003) Reduced models for the medium-frequency dynamics of stochastic systems. J Acoust Soc Am 113(2):834–846. doi:http://dx.doi.org/10.1121/1.1538246

[40] Soize C (2003) Uncertain dynamical systems in the medium-frequency range. J Eng Mech-ASCE 129(9):1017–1027. doi:http://dx.doi.org/10.1061/(ASCE)0733-9399(2003)129:9(1017)

[41] Capiez-Lernout E, Soize C (2008) Robust updating of uncertain damping models in structural dynamics for low- and medium-frequency ranges. Mech Syst Signal Pr 22(8):1774–1792. doi:http://dx.doi.org/10.1016/j.ymssp.2008.02.005

[42] Kassem M, Soize C, Gagliardini L (2011) Structural partitioning of complex structures in the medium-frequency range. An application to an automotive vehicle. J Sound Vib 330(5):937–946. doi:http://dx.doi.org/10.1016/j.jsv.2010.09.008

[43] Ohayon R, Soize C (2014) Advanced Computational Vibroacoustics - Reduced-Order Models and Uncertainty Quantification. Cambridge University Press, New York.

[44] Durand JF, Soize C, Gagliardini L (2008) Structural-acoustic modeling of automotive vehicles in presence of uncertainties and experimental identification and validation. J Acoust Soc Am 124(3):1513–1525. doi:http://dx.doi.org/10.1121/1.2953316

[45] Arnoux A, Batou A, Soize C, Gagliardini L (2013) Stochastic reduced order computational model of structures having numerous local elastic modes in low frequency dynamics. J Sound Vib 332(16):3667–3680. doi:http://dx.doi.org/10.1016/j.jsv.2013.02.019

[46] Arnoux A, Soize C, Batou A, Gagliardini L (2013) Reduced-order computational model for low-frequency dynamics of automobiles. Advances in Mechanical Engineering 310362:1–12. doi:http://dx.doi.org/10.1155/2013/310362

[47] Gagliardini L (2014) Dispersed vibroacoustic responses of industrial products: What are we able to predict? In: Proceedings of the International Conference on Noise and Vibration Engineering ISMA 2014, Leuven, Belgium, September 15–17, 17–37.

[48] Bucher I, Braun SG (1997) Left eigenvectors: Extraction from measurements and physical interpretation. J Appl Mech-T ASME 64(1):97–105. doi:http://dx.doi.org/10.1115/1.2787300

[49] Hansen PC (1987) The truncated SVD as a method for regularization. BIT 27(4):534–553. doi:http://dx.doi.org/10.1007/BF01937276

[50] Guyan RJ (1965) Reduction of stiffness and mass matrices. AIAA J 3(2):380–380. doi:http://dx.doi.org/10.2514/3.2874

[51] Bouhaddi N, Fillod R (1992) A method for selecting master DOF in dynamic substructuring using the Guyan condensation method. Comput Struct 45(5-6):941–946. doi:http://dx.doi.org/10.1016/0045-7949(92)90052-2

[52] Belytschko T, Mindle WL (1980) Flexural wave-propagation behavior of lumped mass approximations. Comput Struct 12(6):805–812. doi:http://dx.doi.org/10.1016/0045-7949(80)90017-6

[53] Chan HC, Cai, CW, Cheung YK (1993) Convergence studies of dynamic analysis by using the finite element method with lumped mass matrix. J Sound Vib 165(2):193–207. doi:http://dx.doi.org/10.1006/jsvi.1993.1253

[54] Jensen MS (1996) High convergence order finite elements with lumped mass matrix. Int J Numer Meth Eng 39(11):1879–1888. doi:http://dx.doi.org/10.1002/(SICI)1097-0207(19960615)39:11¡1879::AID-NME933¿3.0.CO;2-2

[55] Hahn Y, Kikuchi N (2005) Identification of global modeshape from a few nodal eigenvectors using simple free-form deformation. Eng Comput 21(2):115–128. doi:http://dx.doi.org/10.1007/s00366-005-0314-x

[56] Guyader JL (2009) Characterization and reduction of dynamic models of vibrating systems with high modal density. J Sound Vib 328(4-5):488–506. doi:http://dx.doi.org/10.1016/j.jsv.2009.08.012

[57] Guyader JL (1990) Modal sampling method for the vibration study of systems of high modal density. J Acoust Soc Am 88(5):2269–2276. doi:http://dx.doi.org/10.1121/1.400069

[58] Noor A, Anderson M, Greene W (1978) Continuum models for beam- and platelike-lattice structures. AIAA J 16(12):1219–1228. doi:http://dx.doi.org/10.2514/3.61036

[59] Planchard J (1995) Vibrations of nuclear fuel assemblies: A simplified model. Nucl Eng Des 86(3):383–391. doi:http://dx.doi.org/10.1016/0029-5493(85)90303-6

[60] Sigrits J, Broc D (2008) Dynamic analysis of a tube bundle with fluid-structure interaction modelling using a homogenisation method. Comput Method Appl M 197(9-12):1080–1099. doi:http://dx.doi.org/10.1016/j.cma.2007.10.010

[61] Craig RR (1985) A review of time domain and frequency domain component mode synthesis method in combined experimental-analytical modeling of dynamic structural systems. ASME-AMD 67, D.R. Martinez and A.K. Miller, New York.

[62] de Klerk D, Rixen DJ, Voormeeren SN (2008) General framework for dynamic substructuring: History, review, and classification of techniques. AIAA J 46:1169–1181. doi:http://dx.doi.org/10.2514/1.33274

[63] Leung AYT (1993) Dynamic stiffness and substructures. Springer-Verlag, Berlin.

[64] Ohayon R, Soize C, Sampio R (2014) Variational-based reduced-order model in dynamic substructuring of coupled structures through a dissipative physical interface: Recent advances. Arch Comput Method E 21(3):321–329. doi:http://dx.doi.org/10.1007/s11831-014-9107-y

[65] Argyris JH, Kelsey S (1959) The analysis of fuselages of arbitrary cross-section and taper: A DSIR sponsored research program on the development

and application of the matrix force method and the digital computer. Aircr Eng Aerosp Tec 31(3):62–74. doi:http://dx.doi.org/10.1108/eb033088

[66] Przemieniecki JS (1963) Matrix structural analysis of substructures. AIAA J 1(1):138–147. doi:http://dx.doi.org/10.2514/3.1483

[67] Irons B (1965) Structural eigenvalue problems - elimination of unwanted variables. AIAA J 3(5):961–962. doi:http://dx.doi.org/10.2514/3.3027

[68] Hurty WC (1960) Vibrations of structural systems by component mode synthesis. J Eng Mech-ASCE 86(4):51–70.

[69] Hurty WC (1965) Dynamic analysis of structural systems using component modes. AIAA J 3(4):678–685. doi:http://dx.doi.org/10.2514/3.2947

[70] Craig RR, Bampton MCC (1968) Coupling of substructures for dynamic analyses. AIAA J 6(7):1313–1319. doi:http://dx.doi.org/10.2514/3.4741

[71] Bathe KJ, Gracewski S (1981) On nonlinear dynamic analysis using substructuring and mode superposition. Comput Struct 13(5):699–707. doi:http://dx.doi.org/10.1016/0045-7949(81)90032-8

[72] Farhat C, Geradin M (1994) On a component mode synthesis method and its application to incompatible substructures. Comput Struct 51(5):459–473. doi:http://dx.doi.org/10.1016/0045-7949(94)90053-1

[73] Meirovitch L, Hale AL (1981) On the substructure synthesis method. AIAA J 19(7):940–947. doi:http://dx.doi.org/10.2514/3.51023

[74] Meirovitch L, Kwak MK (1991) Rayleigh-Ritz based substructure synthesis for flexible multibody systems. AIAA J 29(10):1709–1719. doi:http://dx.doi.org/10.2514/3.10794

[75] Voormeeren SN, van der Valk PL, Rixen DJ (2011) Generalized methodology for assembly and reduction of component models for dynamic substructuring. AIAA J 49(5):1010–1020. doi:http://dx.doi.org/10.2514/1.J050724

[76] Benfield WA, Hruda RF (1971) Vibration analysis of structures by component mode substitution. AIAA J 9(7):1255–1261. doi:http://dx.doi.org/10.2514/3.49936

[77] Mac Neal R (1971) A hybrid method of component mode synthesis. Comput Struct 1(4):581–601. doi:http://dx.doi.org/10.1016/0045-7949(71)90031-9

[78] Rubin S (1975) Improved component-mode representation for structural dynamic analysis. AIAA J 13(8):995–1006. doi:http://dx.doi.org/10.2514/3.60497

[79] Markovic D, Park KC, Ibrahimbegovic A (2007) Reduction of substructural interface degrees of freedom in flexibility-based component mode synthesis. Int J Numer Meth Eng 70(2):163–180. doi:http://dx.doi.org/10.1002/nme.1878

[80] Ohayon R, Sampaio R, Soize C (1997) Dynamic substructuring of damped structures using singular value decomposition. J Appl Mech-T ASME 64(2):292–298. doi:http://dx.doi.org/10.1115/1.2787306

[81] Park KC, Park YH (2004) Partitioned component mode synthesis via a flexibility approach. AIAA J 42(6):1236–1245. doi:http://dx.doi.org/10.2514/1.10423

[82] Rixen DJ (2004) A dual Craig-Bampton method for dynamic substructuring. J Comput Appl Math 168(1-2):383–391. doi:http://dx.doi.org/10.1016/j.cam.2003.12.014

[83] Beck JL, Katafygiotis LS (1998) Updating models and their uncertainties - I: Bayesian statistical framework. J Eng Mech-ASCE 124(4):455–461. doi:http://dx.doi.org/10.1061/(ASCE)0733-9399(1998)124:4(455)

[84] Ibrahim RA (1985) Parametric Random Vibration. John Wiley and Sons, New York.

[85] Ghanem RG, Spanos PD (1991) Stochastic Finite Elements: A Spectral Approach. Springer-Verlag, New York. Revised edition, Dover Publications, New York, 2003.

[86] Soize C, Ghanem R (2004) Physical systems with random uncertainties: Chaos representation with arbitrary probability measure. SIAM J Sci Comput 26(2):395–410. doi:http://dx.doi.org/10.1137/S1064827503424505

[87] Mace R, Worden W, Manson G (2005) Uncertainty in Structural Dynamics. Special issue of the Journal of Sound and Vibration 288(3):431–790.

[88] Schuëller GI (2005) Computational methods in stochastic mechanics and reliability analysis. Special issue of Computer Methods in Applied Mechanics and Engineering 194(12-16):1251–1795.

[89] Schuëller GI (2005) Uncertainties in Structural Mechanics and Analysis - Computational Methods. Special issue of Computer and Structures 83(14):1031-1150.

[90] Schuëller GI (2006) Developments in stochastic structural mechanics. Arch Appl Mech 75(10-12):755–773. doi:http://dx.doi.org/10.1007/s00419-006-0067-z

[91] Deodatis G, Spanos PD (2008) 5th International Conference on Computational Stochastic Mechanics. Special issue of the Probabilistic Engineering Mechanics 23(2-3):103–346.

[92] Schuëller GI, Pradlwarter HJ (2009) Uncertain linear systems in dynamics: Retrospective and recent developments by stochastic approaches. Eng Struct 31(11):2507–2517. doi:http://dx.doi.org/10.1016/j.engstruct.2009.07.005

[93] Le Maitre OP, Knio OM (2010) Spectral methods for uncerainty quantification with applications to computational fluid dynamics. Springer, Heidelberg.

[94] Soize C (2013) Stochastic modeling of uncertainties in computational structural dynamics - Recent theoretical advances. J Sound Vib 332(10):2379–2395. doi:http://dx.doi.org/10.1016/j.jsv.2011.10.010

[95] Ghanem R, Higdon D, Owhadi H (Eds) (2017) Handbook of Uncertainty Quantification, Springer International Publishing Switzerland. doi:http://dx.doi.org/10.1007/978-3-319-11259-6

[96] Schevenels M, Lombaert G, Degrande G, Degrauwe G, Schoors B (2007) The Green's functions of a vertically inhomogeneous soil with a random dynamic shear modulus. Probabilist Eng Mech 22(1):100–111. doi:http://dx.doi.org/10.1016/j.probengmech.2006.09.001

[97] Bui-Thanh T, Willcox K, Ghattas O (2008) Parametric reduced-order models for probabilistic analysis of unsteady aerodynamic applications. AIAA J 46(10):2520–2529. doi:http://dx.doi.org/10.2514/1.35850

[98] Degroote J, Virendeels J, Willcox K (2010) Interpolation among reduced-order matrices to obtain parameterized models for design, optimization and probabilistic analysis. Int J Numer Meth Fl 63(2):207–230. doi:http://dx.doi.org/10.1002/fld.2089

[99] Marzouk YM, Najm HN, Rahn LA (2007) Stochastic spectral methods for efficient Bayesian solution of inverse problems. J Comput Phys 224(2):560–586. doi:http://dx.doi.org/10.1016/j.jcp.2006.10.010

[100] Galbally D, Fidkowski K, Willcox K, Ghattas O (2010) Non-linear model reduction for uncertainty quantification in large scale inverse problems. Int J Numer Meth Eng 81(12):1581–1608. doi:http://dx.doi.org/10.1002/nme.2746

[101] Lieberman C, Willcox K, Ghattas O (2010) Parameter and state model reduction for large scale statistical inverse problems. SIAM J Sci Comput 32(5):2523–2542. doi:http://dx.doi.org/10.1137/090775622

[102] Nouy A, Soize C (2014) Random fields representations for stochastic elliptic boundary value problems and statistical inverse problems. Eur J Appl Math 25(3):339–373. doi:http://dx.doi.org/10.1017/S0956792514000072

[103] Cui T, Marzouk YM, Willcox KE (2015) Data-driven model reduction for the Bayesian solution of inverse problems. Int J Numer Meth Eng 102(5):966-990. doi:http://dx.doi.org/10.1002/nme.4748

[104] Soize C (2016) Random vectors and random fields in high dimension. Parametric model-based representation, identification from data, and inverse problems. pp:1–65, in Handbook for Uncertainty Quantification edited by Ghanem R, Higdon D, Owhadi H., Springer: Heidelberg. doi:http://dx.doi.org/10.1007/978-3-319-11259-6_30-1

[105] Soize C (2000) A nonparametric model of random uncertainties for reduced matrix models in structural dynamics. Probabilist Eng Mech 15(3):277–294. doi:http://dx.doi.org/10.1016/S0266-8920(99)00028-4

[106] Shannon CE (1948) A Mathematical Theory of Communication. Bell Syst Tech J 27(3), 379–423. doi:http://dx.doi.org/10.1002/j.1538-7305.1948.tb01338.x

[107] Jaynes ET (1957) Information Theory and Statistical Mechanics. Phys. Rev. 106(4):620–630. doi:http://dx.doi.org/10.1103/PhysRev.106.620

[108] Mignolet MP, Soize C (2008) Nonparametric stochastic modeling of linear systems with prescribed variance of several natural frequencies. Probabilist Eng Mech 23(2-3):267–278. doi:http://dx.doi.org/10.1016/j.probengmech.2007.12.027

[109] Soize C (2016) Random matrix models and nonparametric method for uncertainty quantification, pp. 1–69, in *Handbook of Uncertainty Quantification*, edited by R. Ghanem, D. Higdon, and H. Owhadi, doi:http://dx.doi.org/10.1007/978-3-319-11259-6_5-1, Springer International Publishing Switzerland, 2016.

[110] Chen C, Duhamel D, Soize C (2006) Probabilistic approach for model and data uncertainties and its experimental identification in structural dynamics: Case of composite sandwich panels. J Sound Vib 294(1-2):64–81. doi:http://dx.doi.org/10.1016/j.jsv.2005.10.013

[111] Capillon R, Desceliers C, Soize C (2016) Uncertainty quantification in computational linear structural dynamics for viscoelastic composite structures. Comput Method Appl M 305:154–172. doi:http://dx.doi.org/10.1016/j.cma.2016.03.012

[112] Soize C, Chebli H (2003) Random uncertainties model in dynamic substructuring using a nonparametric probabilistic model. J Eng Mech-ASCE 129(4):449–457. doi:http://dx.doi.org/10.1061/(ASCE)0733-9399(2003)129:4(449)

[113] Mignolet MP, Soize C, Avalos J (2013) Nonparametric stochastic modeling of structures with uncertain boundary conditions / coupling between substructures. AIAA J 51(6):1296–1308. doi:http://dx.doi.org/10.2514/1.J051555

[114] Arnst M, Clouteau D, Chebli H, Othman R, Degrande G (2006) A non-parametric probabilistic model for ground-borne vibrations in buildings. Probabilist Eng Mech 21(1):18–34. doi:http://dx.doi.org/10.1016/j.probengmech.2005.06.004

[115] Capiez-Lernout E, Soize C (2008) Robust design optimization in computational mechanics. J Appl Mech-T ASME 75(2):1-11. doi:http://dx.doi.org/10.1115/1.2775493

[116] Mignolet MP, Soize C (2008) Stochastic reduced order models for uncertain geometrically nonlinear dynamical systems. Comput Method Appl M 197(45-48):3951–3963. doi:http://dx.doi.org/10.1016/j.cma.2008.03.032

[117] Capiez-Lernout E, Soize C, Mignolet MP (2014) Post-buckling nonlinear static and dynamical analyses of uncertain cylindrical shells and experimental validation. Comput Method Appl M 271(1):210–230. doi:http://dx.doi.org/10.1016/j.cma.2013.12.011

[118] Soize C, Farhat C (2016) Uncertainty quantification of modeling errors for nonlinear reduced-order computational models using a nonparametric probabilistic approach. Int J Numer Meth Eng, accepted for publication May 30, 2016.

[119] Bouvet P, Siwiak H, Schuh J (2013) Mesures de dispersion acoustique sur 208 en sortie d'usine. Rapport VIBRATEC réf. 353.245.RA.01.B pour le compte de PSA.

[120] Soize C, Batou A (2011) Stochastic reduced-order model in low-frequency dynamics in presence of numerous local elastic modes. J Appl Mech-T ASME 78(6):061003-1–9. doi:http://dx.doi.org/10.1115/1.4002593

[121] Sethian JA (1995) A fast marching level set method for monotonically advancing fronts. P Natl Acad Sci USA 93(4):1591–1595.

[122] Sethian JA, Kimmel R. Computing Geodesic Paths on Manifolds, P Natl Acad Sci USA 95: 8431–8435.

[123] Batou A, Soize C (2013) Uncertainty quantification in low-frequency dynamics of complex beam-like structures having a high-modal density. International Journal for Uncertainty Quantification 1(1):475–485. doi:http://dx.doi.org/10.1615/Int.J.UncertaintyQuantification.2012005286

[124] Batou A, Soize C, Brie N (2013) Reduced-order computational model in nonlinear structural dynamics for structures having numerous local elastic modes in the low-frequency range. Application to fuel assemblies. Nucl Eng Des 262:276–284. doi:http://dx.doi.org/10.1016/j.nucengdes.2013.04.039

[125] Arnoux A (2012) Réduction des modèles numériques en dynamique linéaire basse fréquence des automobiles. PhD thesis. Université Paris-Est, 2012.

[126] Ezvan O, Batou A, Soize C (2015) Multilevel reduced-order computational model in structural dynamics for the low- and medium-frequency ranges. Comput Struct 160:111–125. doi:http://dx.doi.org/10.1016/j.compstruc.2015.08.007

[127] Ezvan O, Batou A, Soize C, Gagliardini L (2016) Multilevel model reduction for uncertainty quantification in computational structural dynamics. Submitted to Computational Mechanics on July 1st, 2016.

[128] Ezvan O, Batou A, Soize C (2014) Reduced-order model for the dynamical analysis of complex structures with a high modal density. The 21st International Congress on Sound and Vibration (ICSV21) 2:1396–1403.

[129] Ezvan O, Batou A, Soize C (2014) Stochastic reduced-order model for the dynamical analysis of complex structures with a high modal density. In: Proceedings of the International Conference on Uncertainty in Structural Dynamics USD 2014, Leuven, Belgium, September 15–17, 4653–4664.

[130] Ezvan O, Batou A, Soize C (2015) Global reduced-order model adapted to the low- and medium-frequency analysis of complex dynamical structures. In: Proceedings of the 1st Pan-American Congress on Computational Mechanics PANACM 2015, Buenos Aires, Argentina, April 27–29, 1022–1028.

[131] Ezvan O, Batou A, Soize C (2015) Réduction de modèle adaptée à la dynamique basse et moyenne fréquence des structures complexes. In: CSMA 2015, 12e Colloque National en Calcul des Structures, Presqu'île de Giens (Var), France, May 18–22.

[132] Ezvan O, Batou A, Soize C (2016) Multilevel stochastic reduced-order model in linear structural dynamics for complex structures. In: VII European Congress on Computational Methods in Applied Sciences and Engineering, ECCOMAS Congress 2016, Crete Island, Greece, June 5–10, paper ID 6736.

[133] Karypis G, Vipin K (1998) A fast and high quality multilevel scheme for partitioning irregular graphs. SIAM J Sci Comput 20(1):359–392. doi:http://dx.doi.org/10.1137/S1064827595287997

[134] Bennighof JK, Lehoucq RB (2004) An automated multilevel substructuring method for eigenspace computation in linear elastodynamics. SIAM J Sci Comput 25(6):2084–2016. doi:http://dx.doi.org/10.1137/S1064827502400650

[135] Gao W, Li XS, Yang C, Bai Z (2008) An implementation and evaluation of the AMLS method for sparse eigenvalue problems. ACM T Math Software 34(4):20:1–20:28. doi:http://dx.doi.org/10.1145/1377596.1377600

[136] Rubinstein R (1981) Simulation and the Monte Carlo Method. John Wiley and Sons, New York.

[137] Golub GH, Van Loan CF (1983) Matrix Computations. John Hopkins Univ Press, Baltimore.

[138] Inman HF, Bradley EL (1989) The overlapping coefficient as a measure of agreement between probability distributions and point estimation of the overlap of two normal densities. Commun Stat Theory 18(10): 3851–3874. doi:http://dx.doi.org/10.1080/03610928908830127